Draft version December 13, 2017
Typeset using LaTeX **twocolumn** style in AASTeX61

CHEMICALLY-DISSECTED ROTATION CURVES OF THE GALACTIC BULGE FROM MAIN SEQUENCE PROPER MOTIONS*

William I. Clarkson,[1] Annalisa Calamida,[2] Kailash C. Sahu,[2] Thomas M. Brown,[2] Mario Gennaro,[2] Roberto Avila,[2] Jeff Valenti,[2] Victor P. Debattista,[3] R. Michael Rich,[4] Dante Minniti,[5,6,7] and Manuela Zoccali[7,8]

[1] *Department of Natural Sciences, University of Michigan-Dearborn, 4901 Evergreen Rd. Dearborn, MI, 48128, USA*
[2] *Space Telescope Science Institute, 3700 San Martin Drive, Baltimore, MD 21218, USA*
[3] *Jeremiah Horrocks Institute, University of Central Lancashire, Preston PR1 2HE, UK*
[4] *Division of Astronomy & Astrophysics, University of California, Los Angeles, 430 Portola Plaza, Box 951547, Los Angeles, CA 90095-1547, USA*
[5] *Departamento de Ciencias Fìsicas, Facultad de Ciencias Exactas, Universidad Andrés Bello, Av. Fernández Concha 700, Las Condes, Santiago, Chile*
[6] *Vatican Observatory, V00120 Vatican City State, Italy*
[7] *Millennium Institute of Astrophysics, Av. Vicuña Mackenna 4860, 782-0436 Macul, Santiago, Chile*
[8] *Instituto de Astrofisica, Pontificia Universidad Catòlica de Chile, Av. Vicuña Mackenna 4860, Santiago, Chile*

ABSTRACT

We report results from an exploratory study implementing a new probe of Galactic evolution using archival Hubble Space Telescope imaging observations. Precise proper motions are combined with photometric relative metallicity and temperature indices, to produce the proper motion rotation curves of the Galactic bulge separately for metal-poor and metal-rich Main Sequence samples. This provides a "pencil-beam" complement to large-scale wide-field surveys, which to-date have focused on the more traditional bright Giant Branch tracers and which, taken together, remain somewhat agnostic on the existence of any difference in mean rotation between metal-poor and metal-rich components within the Galactic bulge, particularly within a few degrees of the Galactic mid-plane.

We find strong evidence that the Galactic bulge rotation curves drawn from "metal-rich" and "metal-poor" samples are indeed discrepant. The "metal-rich" sample shows greater rotation amplitude and a steeper gradient against line of sight distance, as possibly a stronger central concentration along the line of sight. We also investigate selection effects this would imply for the longitudinal proper motion cut often used to isolate a "pure-bulge" sample. Extensive investigation of synthetic stellar populations suggest that instrumental and observational artefacts are unlikely to account for the observed rotation curve differences.

Thus, proper motion-based rotation curves can be used to probe chemo-dynamical correlations for *Main Sequence* tracer stars, which are orders of magnitude more numerous in the Galactic Bulge than the bright Giant Branch tracers. We discuss briefly the prospect of using this new tool to constrain detailed models of Galactic formation and evolution.

Keywords: Galaxy: bulge, Galaxy: disk, Galaxy: kinematics and dynamics, instrumentation: high angular resolution, methods: data analysis, techniques: photometric

Corresponding author: Will Clarkson
wiclarks@umich.edu

* Based on observations made with the NASA/ESA Hubble Space Telescope and obtained from the data archive at the Space Telescope Science Institute. STScI is operated by the Association of Universities for Research in Astronomy, Inc. under NASA contract NAS 5-26555.

1. INTRODUCTION

The diversity of observed properties of the Galactic bulge has challenged attempts to provide a coherent explanation for its formation and subsequent development. For example, while color-magnitude diagrams suggest the majority of bulge stars are likely older than ~ 8 Gy (e.g. Zoccali et al. 2003, Kuijken & Rich 2002, Clarkson et al. 2008, Calamida et al. 2014, although see, e.g. Nataf & Gould 2012, Haywood et al. 2016 and Bensby et al. 2017 for alternative interpretation), minority populations of younger objects have been detected (e.g. Sevenster et al. 1997, van Loon et al. 2003). That measurements of even bulk parameters like bar orientation and axis ratio have not converged with time (e.g. Vanhollebeke et al. 2009) is consistent with a dependence of these properties on the ages of the tracers used. For example, Catchpole et al. (2016) find distinct bar/bulge spatial structures coexisting in the same volume, traced by Mira populations of different ages. As shown by Ness et al. (2013a), the various apparent observational contradictions can be resolved by a scenario in which most bulge stars did indeed form early but later were rearranged into their present-day spatial and kinematic distributions by disk-driven evolution. Recent reviews of Galactic bulge observations and formation scenarios include Rich (2015), Babusiaux (2016), Zoccali & Valenti (2016) and Nataf (2017).

Observations have long suggested a co-dependence between chemical abundance and kinematics in the bulge, particularly as traced by velocity dispersion, providing an observational test of formation and evolution scenarios (e.g. Rich 1990; Minniti 1996). Metal-rich samples show a steeper increase in radial velocity dispersion with Galactic latitude than do the metal-poor objects (whose dispersion-latitude profile is only gently sloped and may be flat); while differences exist in the literature as to the [Fe/H] cuts used to define the two samples, by latitude $|b| \lesssim 3°$ the metal-poor and metal-rich samples have consistent radial velicity dispersions (Figure 4 of Babusiaux 2016 presents a recent compilation for fields along the Bulge minor axis). For the very inner-most fields in the Bulge ($|b| \lesssim 1.0°$ and $|l| \lesssim 2°$), a radial velocity dispersion "inversion" may even be present (an expression of a steeper dispersion gradient with longitude for metal-rich objects), with the metal-rich stars showing *greater* velocity dispersion than the metal-poor objects in bins closest to the Galactic center (e.g. Babusiaux et al. 2014; Zoccali et al. 2017). In a complementary manner, Spaenhauer et al. (1992) traced the proper motion dispersion for a sample of 57 Bulge giants towards Baade's window, allowing the first test of Bulge chemical and kinematic co-dependence using proper motions. No statistically significant discrepancy in proper motion dispersion was found between metal-poor (defined as [Fe/H] < 0.0) and metal-rich ([Fe/H] > 0.0) objects (with Galactic latitudinal proper motion dispersion difference $\Delta\sigma_{\mu,l} \approx 0.5 \pm 0.6$ mas yr^{-1} between the samples), although the sample size was not large.

The implications of observational chemical-dynamical correlations for formation models of the inner Milky Way are the subject of vigorous ongoing observational and theoretical research. For example, Debattista et al. (2017) showed that samples drawn from a continuous metallicity distribution in a pure-disk galaxy model can be "kinematically fractionated" by bar formation into metal-rich and metal-poor populations with quite different morphology and dynamics, depending on their initial (Galactocentric) radial velocity dispersions. This is consistent with the tendency of the stellar population in the "X"-shape to be dominated by metal-rich stars (Vásquez et al. 2013), as has now also been observed in NGC 4710, a nearby disk-dominated galaxy viewed almost edge-on (Gonzalez et al. 2016, 2017).

Indeed, Shen et al. (2010) argue that the radial velocities and morphology of Bulge stellar populations show no need for a substantial spheroidal "Classical" bulge component (at the level of $\lesssim 8\%$ of the disk mass), arguing that the Milky Way can be characterized as a pure-disk galaxy. Nonetheless, a small spheroidal component probably *has* been detected, although its likely contribution to the total Bulge mass is likely well under 10% (Kunder et al. 2016). Interpretation of this component in the context of Galactic formation is not clear; it might, for example, represent part of the Halo population that has also probably been detected in the inner Milky Way (Koch et al. 2016).

1.1. *Does bulge rotation depend on metallicity?*

The trend in bulge mean radial velocity (against Galactic longitude or Galactocentric radius) may also vary with metallicity, but here the magnitude (or even existence) of such a dependence is less clear than for the velocity dispersions.[1]

Harding & Morrison (1993) and Minniti (1996) demonstrated that "metal-rich" stars show a gradient in circular speed with Galactocentric radius, consistent with the "solid body"-type rotation traced by planetary nebulae (Kinman et al. 1988), Miras (Menzies 1990) and SiO masers (Nakada et al. 1993). In con-

[1] The interpretation of any radial velocity-metallicity bifurcation is somewhat complicated by variations both in calibration of the [Fe/H] scale and in the definitions authors use to define "metal-rich" and "metal-poor" samples.

trast, metal-poor objects (then identified with the halo) showed no strong evidence for a rotational trend. (Note that Minniti 1996 defined "metal-rich" as objects with [Fe/H] > -1.00, quite different from the boundary usually used in more recent studies.)

The large ARGOS survey of three-dimensional motions of (mostly clump) giants at $|b| \geq 4°$ showed no [Fe/H] -dependence of the mean radial velocity trend with Galactic longitude, for sub-samples of objects with [Fe/H] > -1.0; the objects in this range show cylindrical rotation, with the sub-component at [Fe/H] $\gtrsim -0.5$ showing separate kinematic identity; Ness et al. 2013b). Among the ARGOS sample, the metal-poor objects at [Fe/H] $\lesssim -1.0$ do show a slightly lower amplitude of rotation curve (with the large-longitude velocity plateau at $\sim \pm 50$ km s^{-1} compared to $\sim \pm 100$ km s^{-1} or more for [Fe/H] > -1.0).

Then Kunder et al. (2016) found that their metal-poor RR Lyrae sample with mostly sub-solar metallicities ($-2.4 <$ [Fe/H] $\lesssim +0.3$, peaking at [Fe/H] ~ -1.0) shows no strong signature of rotation from radial velocities in any Galactic latitude range. This is in contrast to the majority-bulge population, which shows bulk rotation with amplitude $v_{GC}\pm \approx 80$ km s^{-1} progressing from the first to fourth Galactic quadrant (e.g. Howard et al. 2009; Kunder et al. 2016).

Defining their "metal-rich" and "metal-poor" samples as [Fe/H] > 0 and [Fe/H] < 0, respectively, Williams et al. (2016) found no difference in trends of mean line-of-sight velocity with Galactic longitude, from a sample of some 2,000 bright giants among twelve Southern bulge fields ($-10° \lesssim b \lesssim -3.5°$) from the Gaia-ESO Spectroscopic Survey.

Most recently, the 26-field GIRAFFE Inner Bulge Survey (GiBS) spectroscopic sample of Red Clump Giants (RCGs) and Red Giant Branch (RGB) stars may show a small metallicity dependence of the radial-velocity trend, depending on the selection criteria used for metal-poor and metal-rich objects. Using ($-1.0 \lesssim$ [Fe/H] < -0.3) for metal-poor and ($+0.2 <$ [Fe/H] $\lesssim +0.6$) for metal-rich samples, Zoccali et al. (2017) find a slightly steeper gradient of mean radial velocity with Galactic longitude for metal-rich objects than metal-poor, although only at the $\approx 1.5\sigma$ level (their Table 2). In contrast with the samples used by Ness et al. (2013b), Williams et al. (2016) and Kunder et al. (2016), the sample of Zoccali et al. (2017) reaches down to Galactic latitudes $|b| \leq 2.0°$.

Thus, the set of mean-motion determinations from radial velocity studies appears to be somewhat agnostic on the existence of any difference in bulk rotation between metal-rich and metal-poor samples. It is not yet clear to what extent differences in sample selection and even calibration are responsible for the apparent inconsistencies.

The radial velocity studies to-date have also been limited by the small intrinsic population size per field of view (for example, ARGOS typically observed about 600 stars at [Fe/H] > -1.0 per 2°-diameter field of view; Ness et al. 2013b). Thus, mean velocities interpreted for rotation trends represent averages both over quite large angular regions on the sky, and, more importantly, over the entire line of sight depth of the sample in a given sight-line. For example, when rotation trends are fitted to separate populations by metallicity, the uncertainties in trend parameters can be quite large (e.g. Zoccali et al. 2017). It remains to be determined whether the apparently conflicting determinations of Kunder et al. (2016) and Zoccali et al. (2017) are in fact statistically compatible with each other.

To make further progress, an independent measure of bulge rotation is needed, using a tracer sample sufficiently populous that the sample can be dissected by line-of-sight distance to mitigate the statistical limitations of giant-branch tracers. For a single sight-line this suggests main sequence tracers should be used, which are highly challenging for traditional spectroscopic studies.

1.2. *Bulge rotation curves from proper motions*

Proper motions do offer an independent method to kinematically chart the bulge rotation curves, and, if information on chemical composition is available, explore whether multiple abundance-samples really do show distinct *mean* motions as well as the well-established velocity dispersion differences.

To-date, proper motion investigations in the context of multiple populations (or a continuum) have mostly been performed using bright giants. Soto et al. (2007) provided an important early demonstration of vertex deviation using HST proper motions for bright giants (for which spectroscopic abundances and radial velocities completed the set of observational parameters; Babusiaux 2016 shows a more recent compilation of vertex deviation). OGLE proper motions were used to suggest streaming motions between the near- and far-arms of the "X" shape in the Bulge (Poleski et al. 2013). Most recently, proper motions from the VVV survey have already been used to draw proper motion rotation curves for *both* giant-branch and upper main-sequence populations (although the upper main sequence population show substantially different selection effects; Smith et al. 2017, accepted).

Using main sequence (MS) objects as kinematic tracers furnishes several advantages. MS tracers are orders of magnitude more common on the sky, affording the opportunity to dissect a single sight line along the line of sight, thus offering a "pencil-beam" complement to the wide-field surveys that use the bright end of the color magnitude diagram.[2]

It is the charting of the chemically-dissected Bulge rotation curve from MS proper motions that we report here. Because this is a relatively new technique, we briefly review the short literature in MS proper motion determination for the Bulge before proceeding further.

1.3. *Proper motions of bulge populations below the Main Sequence Turn-off*

Proper motion-based rotation curves[3] from *main sequence* Bulge stars are relatively rare in the literature. Kuijken & Rich (2002) were the first to demonstrate the approach for MS populations, for both the Baade and Sagittarius Windows, presenting the HST/WFPC2-derived rotation and dispersion curves against photometric parallax (with photometric parallax determined as a linear combination of color and magnitude in order to remove the color-magnitude slope of the MS tracer population of interest). This demonstrated a clear sense of rotation, with the nearside of the bulge showing positive mean longitudinal proper motion relative to the far-side (a determination made *before* the much brighter RCGs were used to show Bulge rotation from proper motions; Sumi et al. 2004). The proper motion dispersion showed a slight increase in the most populous middle bins of photometric parallax (most strongly pronounced in the latitudinal proper motion dispersion σ_b) for their Sagittarius-Window field. Kuijken (2004) presented an extension of this work to multiple fields across the bulge, including the use of three minor-axis fields to estimate the vertical gravitational acceleration along the Galactic minor axis.

Kozłowski et al. (2006) were able to demonstrate similar behavior to the Kuijken & Rich (2002) rotation curves in their analysis of proper motions in Baade's Window, the only field for which a sufficiently large sample of sufficiently precisely-measured MS stars could be measured from their large 35-field study (using WFPC2 for early-epoch and ACS/HRC for late-epoch observations). While their dispersion curve is consistent with a flat distribution, the rotation trend in galactic longitude was clearly observed. Kozłowski et al. (2006) may also have been the first to detect the weak trend in latitudinal proper motion μ_b due to Solar reflex motion (see Vieira et al. 2007 for discussion of this effect, including its detection using sets of ground-based observations of bulge giants over a 21-year time-baseline). In any case, Kozłowski et al. (2006) were the first to detect the proper motion correlation $C_{l,b}$ at statistical significance from any population (using the RCGs that formed their main target population), using it to constrain the tilt-angle of the Bulge velocity ellipsoid. As they point out, detection of $C_{l,b}$ (or equivalently the orientation angle ϕ_{lb} of the proper motion ellipsoid) allows constraints to be placed on the orbit families for bulge populations, although the conversion from observation to physical constraint is not trivial (e.g. Zhao et al. 1994; Häfner et al. 2000; Rattenbury et al. 2007).

Clarkson et al. (2008, hereafter Cl08) extended the rotation curve approach, using a much deeper dataset with ACS/WFC towards the Sagittarius Window, estimating photometric parallax directly with reference to a fiducial isochrone chosen to pass through the locus describing the average population in the color-magnitude diagram. Consistent with Kuijken & Rich (2002) and Kozłowski et al. (2006), this showed a clear sense of rotation and an increase in proper motion dispersion towards the middle of the population, with a clear detection of the latitudinal proper motion trend from nearside to far-side, and a pronounced peak in the velocity dispersion of both coordinates (σ_l and σ_b) coincident with the most densely-populated middle of the photometric distance-range of the sample. Cl08 converted proper motions to velocities, charting the run of the mean velocity (i.e., the rotation curves), the semiminor and semimajor axis lengths (i.e. the velocity dispersions) and the variation of the orientation ϕ_{lb} of the projected velocty ellipse with line of sight distance, and verified through simulation and comparison with the behavior of Red Clump stars that indeed distance effects *are* observable in MS photometric parallax (though unlike RCG tracers, unresolved binaries blur somewhat the inferred distances for a given main-sequence population).

More recently, in a careful study of three off-axis Bulge fields using WFPC2 for early-epoch observations and ACS/WFC for the late epoch, Soto et al. (2014) were able to extract the rotation curve (and associated proper motion dispersion curves) for a field farther from the

[2] Indeed, giants in the Bulge are so bright that they can be challenging to precisely measure from space due to the requirement to take short exposures.

[3] Throughout, the *rotation curve* is defined as the run of the mean proper motion (or transverse velocity) against relative photometric parallax (or distance). The run of proper motion dispersion (or velocity disperson) is referred to as the *dispersion curve*. The rotation curve is distinct from the *circular speed curve* (the run of circular speed about the Galactic center against distance from the Galactic center), which requires projection to Cylindrical Galactic co-ordinates and an assumption of the orbit shape.

mid-plane, at $(l, b) = (+3.58°, -7.17°)$.[4] Soto et al. (2014) also computed the run of velocity ellipse orientation ϕ_{lb} with photometric distance, finding trends consistent with Cl08. The kinematics of main-sequence objects at some distance from the plane, were thus established to be broadly similar to those at the more central Baade and Sagittarius Window fields.

1.4. *Main-sequence proper motions for multiple populations*

Until recently, no observational dataset existed that would allow the proper motion-based rotation curves to be charted for *multiple* spatially-overlapping main-sequence metallicity samples in the Bulge, as the relevant tracer samples (a few magnitudes beneath the Main Sequence Turn-off, and well clear of the subgiant and giant branches in the CMD) are far too faint and spatially crowded for objects to be chemically distinguished using current spectroscopic technology.

The situation changed with the *WFC3 Bulge Treasury Survey* (hereafter BTS; Brown et al. 2009), which used three-filter flux ratios to construct a temperature index [t], which is a function of F555W, F110W, F160W magnitudes (similar to V, J, H), and a metallicity index [m] that uses F390W, F555W, F814W magnitudes (similar to Washington-C, V,I), with scale factors chosen so that [t] and [m] are relatively insensitive to reddening. This allows stars to be chemically tagged in a relative sense by their location in [m], [t] space, down to much fainter limits and in regions of higher spatial density than currently allowed by spectroscopy. Brown et al. (2010) showed that indeed the wide bulge metallicity range can be traced photometrically, setting [t] and [m] indices for tens of thousands of MS objects in each of the four observed bulge fields, inverting the photometric indices to produce relative [Fe/H] distributions broadly similar to the spectroscopic indications from much brighter objects (e.g. Hill et al. 2011; Johnson et al. 2013). Computing these indices appropriately for objects near the bulge MS turn off, Brown et al. (2010) found that the candidate exoplanet hosts of the SWEEPS field (Sahu et al. 2006) tend to pile up at the metal-rich end of the [m] distribution as expected, suggesting that [m] is indeed tracking metallicity. Exploitation of this unique dataset to directly constrain the star-formation history of the bulge is ongoing (see Gennaro et al. 2015 for an example of the techniques involved).

[4] This was the only field of the three analyzed by Soto et al. (2014) with a sufficient number of well-measured stars to produce the rotation curve from proper motions.

Here we combine the relative metallicity estimates from the WFC3/Treasury survey with ultra-deep proper motions using ACS/WFC, to construct the proper motion-based rotation curves of candidate "metal-poor" and "metal-rich" MS samples, and examine whether and how the kinematics of the two samples differ from each other. Our work represents the first extension of chemo-dynamical studies of the bulge down to the Main Sequence.

This paper is organized as follows. The observational datasets are introduced in Section 2, with the techniques used to classify samples as "metal-poor" or "metal-rich" and to draw rotation curves described in Section 3. The rotation curves themselves are presented in Section 4. Section 5 discusses the implications of our results both for the distribution of populations within the Bulge and proper motion sample selection, and discusses the impact of various systematic effects, with conclusions outlined in Section section 6. Appendices A-G provide supporting information, including the full set of results in tabular form.

2. OBSERVATIONS

By the standards of modern proper motion measurements with HST (e.g. Sahu et al. 2017), the relative streaming motions of the near- and far-side bulge populations are not small (the mean motion of the bulge nearside being typically $\Delta\mu_l \sim 4$ mas yr^{-1} relative to the farside, although the intrinsic proper motion dispersion is of roughly similar magnitude; Calamida et al. 2014). Thus, extraction of proper motion-based rotation curves should in general be reasonably straighforward for many bulge fields for which multiple epochs are available.

For this exploratory study, however, we choose the deepest and most precisely-measured sample of HST proper motions available towards the Bulge, to minimize complications due to completeness effects and varying measurement uncertainty. This is the SWEEPS dataset, which, with many epochs over a 9-year time-baseline, represents the current state-of-the-art in space-based proper motion observation towards the bulge with HST (e.g. Calamida et al. 2015, Kains et al. 2017).

We therefore attach SWEEPS proper motions (subsection 2.1) to the BTS photometry (subsection 2.2), to afford the maximum sensitivity to proper motions for populations that we can label chemically in a relative sense. Table 1 summarizes the observations used in this work.

2.1. *SWEEPS photometry and proper motions*

Table 1. Provenance of the observational datasets used in this work. $N_{\rm all}$ represents the number of objects in each catalog (with measurements in all filters for SWEEPS and BTS). The median Modified Julian Dates are indicated for the 2004 and the 2011-2012-2013 SWEEPS epochs. The SWEEPS field lies at $(\alpha, \delta)_{\rm J2000.0} \approx$ (17:59:00.7, -29:11:59.1), or $(l, b)_{\rm J2000.0} \approx (+1.26^\circ, -2.65^\circ)$.

Dataset	Program (PI)	Observation dates	Instrument	Filters or wavelength range	$N_{\rm all}$	Section
SWEEPS	HST GO-9750 (Sahu)	2004 Feb (MJD 53060)	HST-ACS/WFC	F606W, F814W	339,193	subsection 2.1
	HST GO-12586 (Sahu)	2011 Oct - 2013 Oct				
	HST GO-13057 (Sahu)	(MJD 56333)				
BTS	HST GO-11664 (Brown)	2010 May	HST-WFC3/UVIS	F390W, F555W, F814W	52,596	subsection 2.2
			HST-WFC/IR	F110W, F160W		
VLT	ESO 073.C-0410(A)	2004 June	VLT-UT2/UVES	4812 – 5750Å	123	subsection B.1
	(Minniti)			5887 – 6759Å		

The SWEEPS dataset used here consists of an extremely deep imaging campaign with a 9-year time baseline using ACS/WFC in F606W, F814W (programs GO-9750, GO-12586 and GO-13057, PI K. C. Sahu). The observations, analysis techniques used to produce the proper motions and photometry used herein, are described in some detail in previous papers (Sahu et al. 2006, hereafter Sa06; Cl08; Calamida et al. 2014, hereafter Ca14; Calamida et al. 2015, hereafter Ca15, and Kains et al. 2017). Here we briefly describe the relevant characteristics for the present study.

The observations cover a single ACS/WFC field of view ($\sim 3.4' \times 3.4'$) in the Sagittarius Window, a low-reddening region,[5] close in projection to the Galactic center ($l, b = 1.26^\circ, -2.65^\circ$). Proper motions were estimated using effective-PSF methods developed for HST and implemented for ACS/WFC in the `img2xym.F` routine (by J. Anderson; Anderson & King 2006) and associated utilities to accurately measure stellar positions in individual images (see Anderson et al. 2008a and Anderson et al. 2008b for detailed discussion of the methods).

The 2011-2012-2013 epoch consists of 60 (61) images in F606W (F814W) taken with an approximately two-week cadence, while the 2004 epoch consists of 254 (265) exposures in F606W(F814W) taken over a 1-week interval in 2004 (Sa06, all exposures in both programs being $\approx$ 5.5 minutes each, which well-samples the Bulge MS and minimizes down-time for buffer-dumps).

Because the disk and bulge stars move relative to each other, the 2011-2012-2013 images were reduced separately from those in the 2004 epoch. Proper motions were derived from the best-fit positional differences between the 2004 and 2011-2012-2013 datasets; they thus represent two-epoch proper motions but with positions in each individual epoch measured to very high accuracy. The reference frame for the proper motions is that of the average bulge population in the line of sight, with obvious foreground disk members removed from the sample of tracer stars used to fit reference frames across epochs. Ca15 also conducted extensive artificial star-tests to estimate measurement uncertainty in the proper motions, with artificial objects injected with proper motions into *individual* measurement frames and the uncertainty in proper motion characterized as a function of apparent magnitude.

The result is a set of 339,193 objects with ACS/WFC positions, apparent magnitudes, and proper motion estimates, all with uncertainties characterized as a function of apparent magnitude. Exploitation of these data are presented in Calamida et al. (2014, 2015) and Kains et al. (2017).

2.2. *WFC3 photometry from the WFC3 Bulge Treasury Project (BTS)*

The WFC3 Bulge Treasury Project (BTS; program GO-11664, PI T. M. Brown) visited four fields in the Bulge, with WFC3, including the SWEEPS field. The observations are described in detail in Brown et al. (2010), here we briefly summarize the characteristics relevant for the present paper.

In each field, observations were taken in UVIS/F390W (11,180s), UVIS/F555W (2,283s), UVIS/F814W (2,143s), IR/F110W(1,255s) and IR/F160W (1,638s), using dithered IR images (field of view $123'' \times 136''$) appropriate to fully cover the UVIS observations (field of view $162'' \times 162''$). Good overlap was achieved with the SWEEPS ACS/WFC observations; nearly all the BTS objects in this field also fall within the SWEEPS ACS/WFC field of view (Figure 1).

[5] $E(B-V) \approx$ 0.5-0.7, depending on the reddening prescription; e.g. Ca15

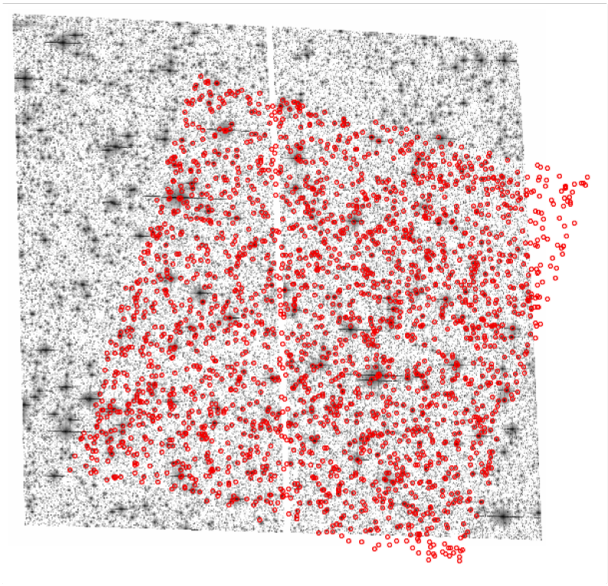

Figure 1. Comparison of the fields of view for the SWEEPS ACS/WFC and BTS datasets towards the Sagittarius Window. A representative sample of bright BTS objects is plotted over a distortion-corrected "drizzled" stack of F814W images from the 2004 epoch. (Unlike most subsequent figures, here the red symbols represent WFC3 observations rather than the "metal-rich" end of the metallicity sample.) North is up, East left, and the ACS/WFC field of view is approximately $3.4' \times 3.4'$. The ACS/WFC field center is located approximately at $(\alpha, \delta)_{\rm J2000.0}$ = (17:59:00.7, -29:11:59.1), or $(l, b)_{\rm J2000.0} = (+1.26°, -2.65°)$. See section 2.

The Version-1 BTS catalog, which we use here, used photometry and positions measured with `daophotII` (Stetson 1987) from the early-epoch observations (GO-11664). The resulting BTS v1 catalog lists 400,424 objects in the Sagittarius window with reported apparent magnitude in any of the BTS filters. Of these, 52,596 have measurements in all five of the BTS filters that are required to construct [t], [m] estimates.

A more recent version of the BTS catalog using improved analysis methods and exploiting the second-epoch BTS observations (HST-GO-12666, PI T. M. Brown), was recently released to the MAST archive when the present work was already entering the writeup stage. Since this second version contains improved measurements compared to v1, application of the techniques we describe here to the entirety of the BTS dataset is straightforward. We defer to a future article the reporting of the applications of our techniques to all four BTS fields.

3. ANALYSIS

We used the BTS photometry to draw "metal-rich" and "metal-poor" samples by use of [t], [m],[6] and used the SWEEPS data to estimate the relative photometric parallaxes and proper motions. The SWEEPS deep (F606W, F814W) color-magnitude diagram was used to estimate relative photometric parallax (π') because this choice of filters is relatively insensitive to metallicity variations when compared to, for example, the C, V, I color-magnitude diagram presented in Brown et al. 2010.

This Section is organized as follows: subsection 3.1 describes the merging of the SWEEPS and BTS catalogs, with the sample selection for proper motion selection discussed in subsection 3.2 and the calculation of the photometric indices [t], [m] shown in subsection 3.3. The indices require a prescription for extinction, discussed in subsection 3.4. The Main-sequence sample of interest was characterized in terms of [t], [m] in subsection 3.5; the use of this characterization to draw relatively "metal-rich" and "metal-poor" samples is communicated in subsection 3.6. The kinematic behavior of the two samples was then measured in two ways; a simple one-dimensional characterization of longitudinal proper motion μ_l is indicated in subsection 3.7, while a more sophisticated dissection of the velocity ellipse with relative photometric parallax π' and conversions from π' to distance D is shown in subsection 3.8.

3.1. *Merging the ACS/WFC and BTS catalogs*

The BTS and SWEEPS catalogs were first cross-matched by equatorial co-ordinates. Although the absolute pointing of HST is accurate only to $\sim 0.1''$ (Gonzaga & et al. 2012), with F814W observations in both datasets,[7] matching of similar objects in both catalogs is straightforward (using F555W and F606W measurements in WFC3 and ACS/WFC respectively to refine the matches). For the first round of matching, a kd-tree approach was used to cross-match on the sphere, with a 5-pixel radius used for initial matching. In the second round, pixel-positions in the two catalogs were cross-matched and fit using a general linear transformation for objects in the $18 \leq F814W \leq 26$ range. While the population of good matches transitions to a background of mismatched objects at a radius of ∼2-

[6] We take this opportunity to remind the reader that [m] is a relative metallicity index; while populations can be inter-compared by metallicity, the absolute scale is uncertain at the level of ~ 0.15 dex; Brown et al. 2009, 2010.

[7] Small differences in effective bandpass of the F814W filter between ACS/WFC and WFC3 do not significantly impact the cross-matching.

Table 2. Vertices of the selection polygon in the SWEEPS CMD that was used to select objects for further proper motion study. See subsection 3.2 for discussion.

(F606W - F814W)	F606W
mag	mag
1.40	24.80
1.54	21.30
1.34	20.50
1.17	23.80

pixels and larger, the vast majority of cross-matches were somewhat better, falling within a 1-pixel matching distance. The cross-matching resulted in a master-list of objects common to both catalogs.

The matching process resulted in a list of 47,537 objects with proper motions and seven-filter apparent magnitudes, with uncertainty estimates for all quantities.

3.2. *Sample selection for proper motion study*

The successive selection steps isolating the sample for further study, are detailed in Table 3. Of an initial sample of 339,193 SWEEPS objects and 400,424 BTS objects, 9,682 ($\sim 2.9\%$) were used for further analysis.

Two aspects of the sample selection are worth highlighting. Firstly, the selection region in the (F606W, F814W) color-magnitude diagram was chosen to be well clear of the Main Sequence Turn-off, subgiant and giant branches, to encompass as many stars as possible with good proper motion measurements, and finally to capture a region over which the MS locus for a given population is reasonably free of curvature in the CMD. The co-ordinates of this selection region are given in Table 2. Secondly, the photometric metallicity and temperature indices include coefficients that amplify measurement uncertainty (particularly F110W and F160W, which appear in the temperature index [t]). For this reason, objects were only selected for further study for which all apparent magnitude uncertainties in the photometric catalog are smaller than 0.1 mag.

3.3. *Production of* [t], [m] *for the proper motion sample*

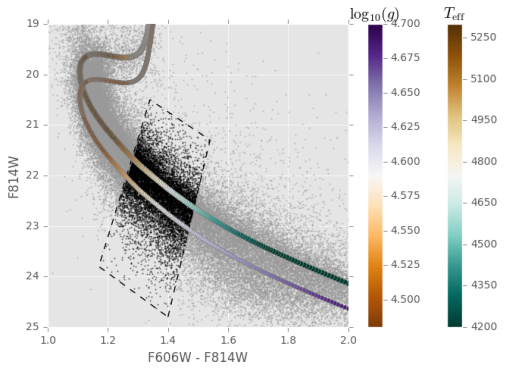

Figure 2. Region-selection in the SWEEPS color-magnitude diagram. The dashed polygon shows the selection region for objects selected for proper motion study (see subsection 3.2 and Table 2). To illustrate typical stellar parameter ranges for this sample, also overplotted is a 10 Gy isochrone at [Fe/H] $= -0.09$ from the "canonical" α-enhanced set within the BaSTI library (Pietrinferni et al. 2004, using the "F05" opacities of Ferguson et al. 2005). The isochrone is plotted twice, color-coded to show $\log(g)$ (left colorbar) and $T_{\rm eff}$ (right colorbar) and offset for clarity, with color minima and maxima set to the range of parameters across the sample of interest. See subsections 3.2 and 3.3.

Table 3. Selection steps used to isolate the proper motion sample for further study. The cuts are cumulative, reading from top to bottom. Objects are eliminated for which *any* of the seven phometry and two proper motion measurements are listed as a "bad" value in either the SWEEPS or BTS catalogs. In practice this limits the sample to ($18.5 \leq F606W \leq 27.5$). The SWEEPS CMD selection region is shown in Figure 2. For the three instrumental configurations listed, objects must show photometric uncertainty < 0.1 mag in all the filters. Objects passing [t], [m] clipping satisfy ($-3.50 \leq$ [t] ≤ -1.00) and ($-0.60 \leq$ [m] ≤ 0.50). See discussion in Sections 3.2-3.6.

Selection	N(remaining)	N(removed)
SWEEPS sample	339,193	-
Cross-matched with BTS	55,666	283,527
BTS measurements in all filters	47,537	8,129
Within SWEEPS CMD selection region	10,225	37,312
σ(ACS/WFC) < 0.1 mag	10,222	3
σ(WFC3/UVIS) < 0.1 mag	10,209	13
σ(WFC3/IR) < 0.1 mag	10,145	64
Clipping far outliers in [t], [m]	9,682	463

The photometric indices [t], [m] take the following form (Brown et al. 2009):

$$[\mathrm{t}] \equiv (V-J) - \alpha(J-H)$$
$$[\mathrm{m}] \equiv (C-V) - \beta(V-I) \qquad (1)$$

with $\alpha \equiv E(F555W-F110W)/E(F110W-F160W)$ and $\beta \equiv E(F390W-F555W)/E(F555W-F814W)$, all of which depend on stellar parameters. The median values of these stellar parameters for the proper motion sample ($T_{\rm eff} \approx 4800$ K and $\log(g) \approx 4.6$) were estimated from an isochrone chosen to overlap the observed sample (see Figure 2; several combinations of metallicity, age and extinction were tried, indicating that the parameter range for this sample is roughly 4200 K$\lesssim T_{\rm eff} \lesssim$ 5200 K and $4.5 \lesssim \log(g) \lesssim 4.7$).

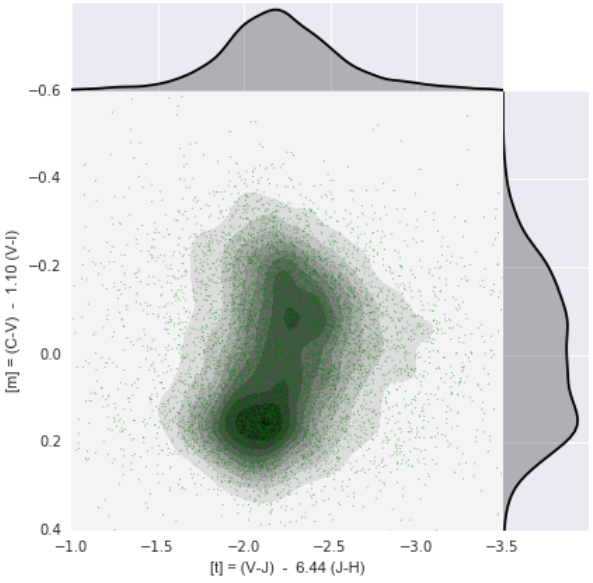

Figure 3. [t], [m] distribution of the population selected for proper motion study. In the *main panel,* green points show individual objects, black contours show the smoothed representation as a two-dimensional KDE with ten levels plotted. Marginal distributions in [t] and [m] are shown in the *top* and *right* panels, respectively. Typical estimates for measurement uncertainty in this space are presented in Figure 18. See subsection 3.3.

3.4. *Extinction estimates for reddening-free indices*

The factors α, β are three-filter extinction ratios (Brown et al. 2009). Synthetic photometry was used to estimate the relationship between reddening and extinction for the objects of interest, and to generate reddening vectors in the various filter combinations of interest. For a range of $E(B-V)$ values, `pysynphot` was used to generate synthetic stellar spectra and the run of A_X against $E(B-V)$ was fit as $A_X = k_X E(B-V)$ separately for all seven filters used in this study, over the range $0.0 \leq E(B-V) \leq 1.5$. The calculation was performed for $T_{\rm eff}$, $\log(g)$ appropriate to the SWEEPS CMD region chosen for proper motion study (Table 4). The process was repeated for low- and high-metallicity objects to estimate sensitivity of the extinction prescription to metallicity variation within the sample selected for further study, and for ($T_{\rm eff}$, $\log(g)$) for objects at the median, minimum and maximum $T_{\rm eff}$ within this sample to estimate spread of α, β along the sample. For convenience, derived quantities $A_{F606W} - A_{F814W}$ and the scale factors were also computed for MS objects.

This procedure requires a prescription for the extinction law towards the bulge. This extinction law appears to be somewhat non-standard and strongly spatially variable, with some doubt in the literature about whether a single-parameter model can accurately reproduce observed behavior from the visible to the near-infrared (e.g. Nataf et al. 2016, and references therein). As the [t], [m] indices use photometry in a very broad color-range ($CVIJH$), systematic uncertainties in the extinction prescription will in turn impact any inferences about the underlying metallicity distribution (this is one reason why we use [t], [m] only to classify objects by *relative* [Fe/H] estimates).

To make progress, we adopted a single-parameter reddening law, but with ratio of selective to total extinction $R_V = 2.5$, as suggested by the investigations of Nataf et al. (2013).[8] As this value is not among the standard parameterizations available in `pysynphot`, the coefficients $A_X/E(B-V)$ for the seven filters were estimated for $R_V = 2.1$ and $R_V = 3.1$ and linearly interpolated to $R_V = 2.5$.

Table 4 shows the adopted coefficients, along with the derived values for the F606W-F814W color, and, finally, the coefficients α, β in the [t], [m] indices. These are quite different from the MS coefficients reported in Brown et al. (2009), as expected since here we are targeting a specific population some way beneath the Main Sequence turn-off, and have used a different prescription for extinction.

Within the sample of interest, the variation of all extinction-relevant quantities appears to be small; α, β each vary by < 0.1 between the two abundance-sets tested, and, for a given abundance (and choice for R_V), by $\lesssim 0.02$ across the $T_{\rm eff}$ range of this sample. Here we adopt $(\alpha, \beta) = (6.44, 1.10)$.

3.5. *The* [t], [m] *distribution*

The ([t], [m]) distribution of objects is shown in Figure 3. Two concentrations are apparent; one near ([t],

[8] As a check, the entire kinematic analysis of Sections 3 & 4 was also performed using $R_V = 3.1$. Although the mean position of objects in the [t], [m] diagram shifts slightly when $R_V = 3.1$ is adopted instead of $R_V = 2.5$, the kinematic trends for the "metal-rich" and "metal-poor" samples are similar.

Table 4. Estimates of $A_X/E(B-V)$ and derived parameters. Here $T_{\rm eff} = 4800.0$ and $\log(g) = 4.59$. For convenience, the scale factor for the SWEEPS color index is also shown. The quantities α, β give the extinction ratios relevant for [t], [m]. Specifically, $\alpha \equiv E(F555W - F110W)/E(F110W - F160W)$ and $\beta \equiv E(F390W - F555W)/E(F555W - F814W)$. See subsection 3.3 and subsection 3.4.

Config	CCM89, R_V = 2.1: log(Z)= -3.3	CCM89, R_V = 2.1: log(Z)= -1.6	CCM89, R_V = 3.1: log(Z)= -3.3	CCM89, R_V = 3.1: log(Z)= -1.6	CCM89, R_V = 2.5: log(Z)= -3.3	CCM89, R_V = 2.5: log(Z)= -1.6
ACS/WFC1/F606W	1.847	1.849	2.786	2.788	2.222	2.224
ACS/WFC1/F814W	1.064	1.064	1.821	1.822	1.366	1.367
WFC3/UVIS1/F390W	3.507	3.492	4.489	4.475	3.899	3.885
WFC3/UVIS1/F555W	2.183	2.186	3.167	3.171	2.576	2.58
WFC3/UVIS1/F814W	1.074	1.075	1.833	1.834	1.377	1.378
WFC3/IR/F110W	0.560	0.558	1.025	1.021	0.746	0.743
WFC3/IR/F160W	0.345	0.345	0.635	0.634	0.461	0.460
$(\text{F606W-F814W})_{\text{ACS/WFC1}}$	0.784	0.785	0.965	0.966	0.856	0.857
α	7.55	7.64	5.49	5.56	6.42	6.49
β	1.19	1.18	0.99	0.98	1.10	1.09

[m]) = (-2.0, 0.15), with a second, more elongated concentration with major axis angled at about $-45°$ in Figure 3, centered near ([t], [m]) $\approx (-2.2, -0.1)$.

Figure 4 shows an attempt to reproduce the distribution of [m] only as a Gaussian Mixture Model (GMM; see Appendix A for discussion of the technique). At least two components seem to be required, although the data do not discriminate between the simplest model that fits the data (two components) and a continuum (e.g. 8 components).

In early trials using data selected only on photometric measurement uncertainty, a mixture model with more than three components would usually include an extremely broad, low-significance Gaussian component. On plotting the [m] counts on a log-scale, this component was seen to be fitting handfuls of far outliers in the [m] distribution (with $|[m]| > 0.5$; compare with the range in Figure 4). This may be expected if the outliers are not well-represented by the model form; nevertheless, the GMM implementation would attempt to assign a model component to the outliers once the model grew sufficiently complex, which in turn would distort model components much nearer to the location of the main population of objects. Circumventing this outlier problem was the main motivator for outlier removal in [t], [m] when selecting objects for further analysis (Table 3).

3.6. *Classifying samples in* [t], [m]

To draw "metal-rich" and "metal-poor" samples from the population selected for rotation curve extraction (Figure 2), the population was characterized as a Gaussian Mixture Model (GMM) in ([t], [m]) space, and members of the "metal-poor" and "metal-rich" samples identified by their formal membership probability w_{ik} (see Appendix A).

Figure 5 shows the ([m], [t]) GMM characterization of the population. To examine the impact of changing the number of model components K, the [t], [m] data were split into two equal-size samples (the "training" and "test" sets), and the GMM fit using the "training" set. Samples (of [t], [m]) were then drawn from the model and perturbed by measurement covariances $\mathbf{S}_i$ from the "test" set, and the ([t], [m]) distribution of this predicted set compared with the "test" set. The GMM predicts distributions slightly more centrally concentrated than the true distribution, but for $K = 4$ the residual "images" do not suggest the presence of a missing model component (Figure 5). Repeated trials using $K = 3$ model components consistently showed that the three-component model typically leaves a strong residual at ([t], [m]) $\approx (-2.2, -0.15)$ that is not present with $K = 4$, while the formal fit statistics appear somewhat worse for $K = 3$ than for $K = 4$. We therefore adopt a four-component Gaussian Mixture Model to characterize the observed distribution in [t], [m] space for the rest of this work.

Table 5 presents the parameters of the adopted four-parameter GMM prescription for the [t], [m] distribution. As [t], [m] each represent three-filter flux ratios expressed in logarithmic units, subject to systematics both in absolute calibration and in extinction prescription, the translation from [t], [m] to absolute $T_{\rm eff}$ and [Fe/H] is somewhat non-trivial and subject to systematic uncertainty; throughout this work, our goal is to *characterize* the observed distribution of objects in or-

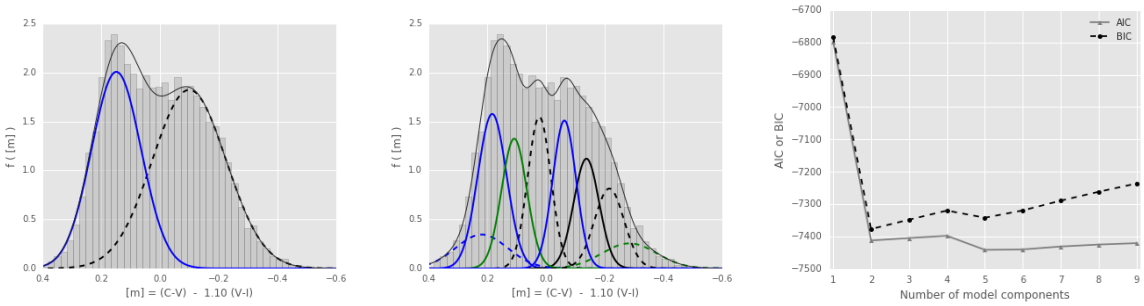

Figure 4. *Left panel:* distribution of [m], for objects satisfying $-2.8 \leq$ [t] ≤ -1.4, representing roughly the population within the outer contour in Figure 3. The gray shaded region shows the observed [m] distribution. The upper gray solid line shows a Gaussian Mixture Model trained on the [m] distribution. The colored solid and dashed curves show realizations of the individual model components. *Middle panel:* as in the left panel, but with an eight-component Gaussian mixture specified as an ansatz for a continuum of populations. *Right panel:* Formal assessment of the number of parameters required to reproduce the observed [m] distribution. Standard figures of merit, the Bayesian Information Criterion (BIC, black dashed line) and the Akiake Information Criterion (AIC, gray solid line; see e.g. Ivezić et al. 2014) are plotted as a function of the number of model components. A GMM representation of the [m] distribution seems to require at least two components, with little improvement for more complex models. See subsection 3.3.

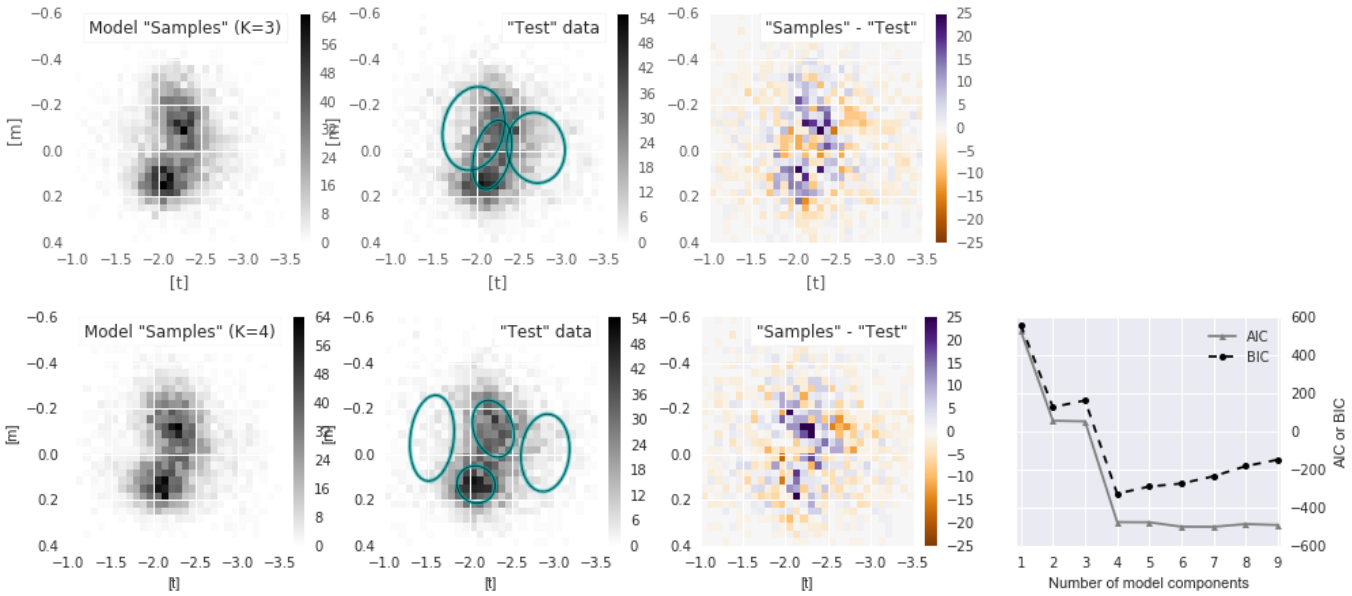

Figure 5. Gaussian Mixture Model (GMM) of the population selected for rotation curve study. The first three columns show Hess diagrams in ([t], [m]) space, using using $K = 3$ (top row) and $K = 4$ (bottom row) mixture components. *Left panels* show the histogram of samples drawn from a GMM fit to a randomly selected sample of half the data (the "training set"). The *middle-left panels* show the other half of the data (the "test set"), with the 1σ contours of the model components overplotted as thick cyan ellipses. The *middle-right panels* show the residuals (samples from the model minus the observed counts in the "test set"). The lower-right plot shows formal fit statistics as a function of the number of model components. See subsection 3.6.

der to draw samples near the extremes of the underlying relative abundance distribution.[9]

A rough estimate for the centroid [Fe/H] values of the two samples may be drawn by charting [Fe/H] contours in the [t], [m] diagram for synthetic stellar populations and interpolating to estimate [Fe/H] at the [t], [m] locations of the model component centroids (see subsection E.1 for more details on the synthetic stellar populations used). The GMM component centroids presented in Table 5 correspond to $[\mathrm{Fe/H}]_0 \approx +0.18$ for the "metal-rich" sample (using scaled-to-solar isochrones) and $[\mathrm{Fe/H}]_0 \approx -0.24$ for the "metal-poor" sample (us-

[9] Throughout this paper, the two samples are indicated with inverted commas to remind the reader of the limited scope of our interpretation of the "metal-rich" and "metal-poor" samples.

Table 5. Parameters of the Gaussian Mixture Model in [t], [m] space for stars beneath the main sequence selected for further study. Reading left-right, columns indicate the component index k, its label (if any), its (rounded) mixture fraction α_k, the two components of its centroid, and the three unique components of the covariance matrix $\mathbf{V}_k$. See subsection 3.5.

k	Name	α_k	$[t]_0$	$[m]_0$	$\sigma^2_{[t][t]}$	$\sigma^2_{[m][m]}$	$\sigma^2_{[t][m]}$
			mag	mag	(mag^2)	(mag^2)	(mag^2)
0	"metal-poor"	0.580	-2.26	-0.09	0.0451	0.0149	-0.00747
3	"metal-rich"	0.334	-2.05	0.16	0.0368	0.0039	-0.00225
1	-	0.031	-1.42	-0.05	0.0215	0.0385	0.00043
2	-	0.055	-2.96	0.02	0.0301	0.0261	-0.00396

ing α-enhanced isochrones for this model component). These centroids are roughly consistent with values suggested from spectroscopic surveys (e.g. Zoccali et al. 2017; Hill et al. 2011).

It is important to remember that we are *not* at this stage suggesting that the bulge sample of BTS is indeed bimodal in metallicity (as opposed to a continuum of populations, e.g. Gennaro et al. 2015; Debattista et al. 2017). Instead, we are using the photometric indices [t], [m] to draw samples near the extremes of relative abundance.

For an object to be classified with the "metal-rich" or "metal-poor" sample, it must show formal membership probability $w_{ik} \geq 0.7$ (Equation A1; note that an object need not be classified with either sample when there are four model components), using uncertainty propagation to approximate the suitable measurement covariance matrix for each object (see Figure 6 and Appendix A).

The threshold $w_{ik} \geq 0.7$) was chosen as a tradeoff between sample purity (typical objects should not fall into more than one model component at the chosen threshold) and the need to have a sufficient sample size (at least a few thousand) to permit the dissection of the proper motions by relative photometric parallax with sufficient resolution to chart the rotation curves.

The fiducial ridgelines for photometric parallax were determined by a simple empirical fit to the mean "metal-rich" and "metal-poor" samples in the *SWEEPS* CMD. A second-order polynomial fit adequately represents the median samples, and allows very rapid evaluation of relative photometric parallax. Figure 6 shows the samples identified with all four GMM model components, while Figure 7 shows the adopted loci for the "metal-rich" and "metal-poor" samples. The parameters of the loci themselves are given in Table 6.

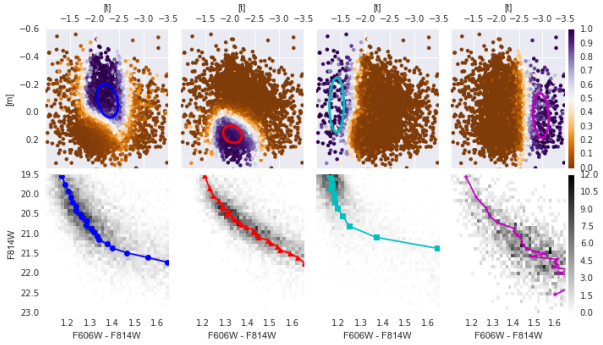

Figure 6. Drawing samples by relative abundance, using location in ([t], [m])-space. The *top row* shows the [t], [m] sample color-coded by membership probabilities w_{ik} (Equation A1) for the k'th model component in the GMM characterization of the observed distribution. The 1σ ellipse for the k'th model component is overplotted in each case as a colored ellipse. The *bottom row* plots the (F606W, F814W) color-magnitude diagram for samples with $w_{ik} > 0.7$ in each component. Reading left-right, the columns describe populations identified with the "metal-poor" sample (blue in all figures in this paper), the "metal-rich" (red in all figures), and the two populations that appear to fit different regions of the background. See the discussion in subsection 3.6.

Table 6. Ridgeline parameters in the SWEEPS color-magnitude diagram, for the "metal-poor" and "metal-rich" samples. These purely empirical ridgelines are used to rapidly evaluate photometric parallax for objects in each sample, and take the form $F814W = \Sigma_j a_j x^j$ with x the (F606W-F814W) color. See subsection 3.6 for discussion.

k	Name	a_0	a_1	a_2
		mag		(mag^{-1})
1	"metal-poor"	-19.855	53.335	-16.904
3	"metal-rich"	3.256	20.520	-5.679

3.7. *Rotation curves*

Armed with "metal-rich" and "metal-poor" samples from the BTS photometry, along with mean fiducial sequences in the SWEEPS color-magnitude diagram for the two samples, the next step is to chart their proper motion rotation curves. Figure 8 shows the raw distribution of longitudinal proper motion μ_l with relative photometric parallax for the "metal-rich" and "metal-poor" samples. The behavior against Galactic longitude is characterized in Figure 9.

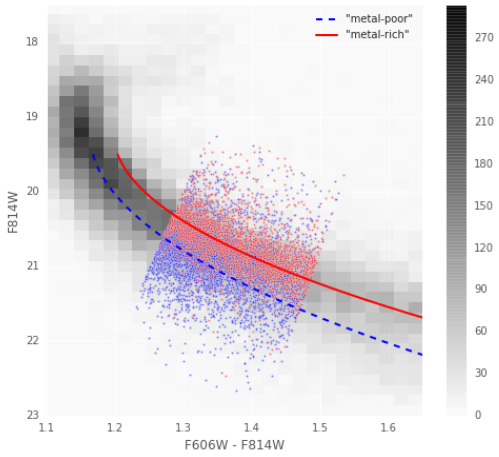

Figure 7. Ridgelines for the "metal-rich" and "metal-poor" samples. The grayscale shows the ACS/WFC(F606W, F814W) Hess diagram for the larger SWEEPS sample. Objects falling within the region of interest for our kinematic study are presented as points, color-coded by "metal-rich" (red) or "metal-poor" (blue). The empirical median-sample ridgelines for the "metal-rich" (red solid) and "metal-poor" (blue dashed) are overlaid. See subsection 3.6 and Table 6.

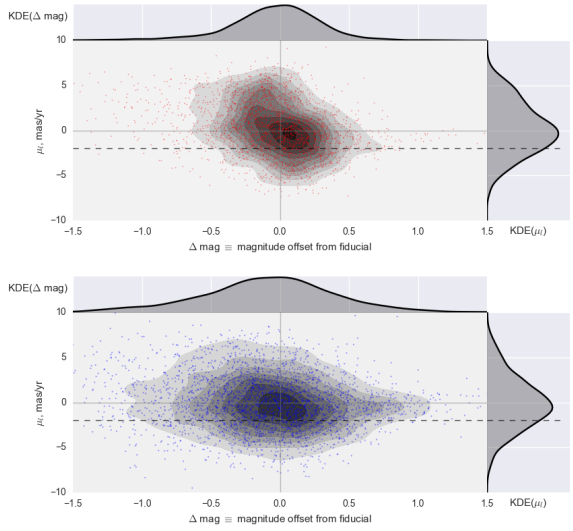

Figure 8. Raw distribution of μ_l against relative photometric parallax (π'), for the "metal-rich" (red) and "metal-poor" (blue) populations. In each figure, the points themselves are illustrated by colored scatterplots in the main panels, with density contours indicated in grayscale. In both figures, the top- and right-panels show the marginal distributions of π'(top panels) and μ_l (right panels). See subsection 3.7.

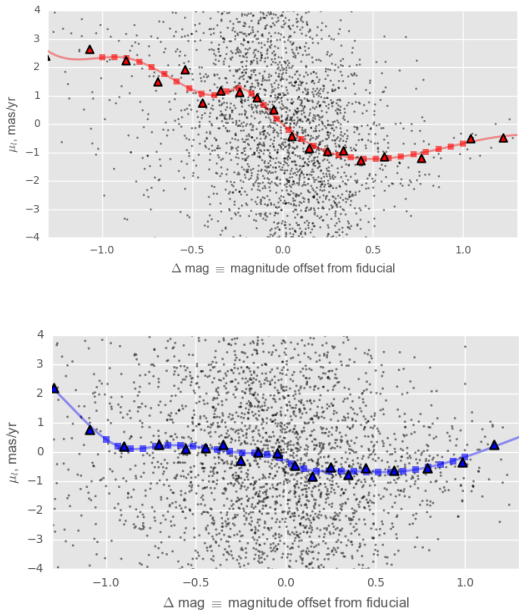

Figure 9. The raw μ_l distributions against relative photometric parallax (see Figure 8). "metal-rich" is denoted in red in the top-panel, "metal-poor" in blue in the bottom panel. The population is broken into bins in relative distance-modulus and the median value $\overline{\mu_l}$ determined for each bin (triangles). Faint continuous lines show a third-order smoothed spline approximation fit to the binned proper motions $\overline{\mu_l}$, while squares indicate equally-spaced evaluations of the spline approximation over the range of relative moduli ($-1.0 \leq (m - m_0) < +1.0$). See subsection 3.7.

Several general differences are apparent between the samples. Firstly, there is a general sense of rotation in *both* samples, with the foreground showing positive μ_l, changing to negative μ_l on the far side, although the amplitude of the difference is roughly a factor 2 higher for the "metal-rich" sample. Secondly, the "metal-poor" sample shows greater spread in relative photometric parallax (π').

3.8. *Proper motion ellipse dissected by relative photometric parallax*

With a difference in rotation curves suggested from the behavior of μ_l against relative photometric parallax, we can move to a greater level of sophistication and chart the distance-variation of the (l, b) proper motion ellipse. The approach shares several similarities to that reported in Cl08; relative photometric parallaxes were assigned to each star with reference to the fiducial sequence (appropriate for the metallicity-sample from which the star is drawn) and the sample partitioned into bins of relative photometric parallax π', with bin-widths adjusted so that each bin has the same number of objects.

The proper motion distribution within each bin was fit as a two-dimensional Gaussian, centered at $\vec{\mu}_0$ and with covariance matrix $\mathbf{V}_\mu$. Uncertainties in fitted quantities were estimated by parametric bootstrapping: synthetic samples for each bin were drawn from the best-fit model, perturbed by the estimated proper motion uncertainty, and the distribution of recovered parameters over the bootstrap trials adopted as the estimated parameter uncertainties. Because the GMM method can be sensitive to outliers, a single pass of sigma-clipping was applied to the proper motion sample within each distance bin using a $\pm 3\sigma$ threshold; this typically removed roughly 1-2% of the points per bin, with the exeption of the most distant π' bin (see Tables 15 & 16).

Several improvements have been made over the analysis reported in Cl08. For example, rather than subtracting the estimated proper motion uncertainty in quadrature from the model covariances after fitting, the "extreme deconvolution" formulation of Bovy et al. (2011) was used, which incorporates estimated measurement uncertainty as part of the fitting process (see Appendix A). The estimates of proper motion uncertainty themselves have also been improved compared to Cl08, in both the characterization of random uncertainty through the artificial star tests of Ca15 and through improved characterization of residual relative distortion (Kains et al. 2017). Details of the uncertainty estimates we adopt here are presented in subsection A.2; for the apparent magnitude range of interest here, the total proper motion uncertainty estimates ($\epsilon_i \lesssim 0.13$ mas yr^{-1}) are much smaller than the intrinsic proper motion dispersion of the bulge (~ 3 mas yr^{-1}).

4. RESULTS

4.1. *Rotation curves for the "metal-rich" and "metal-poor" samples*

The trends in observed motions are shown graphically in Figures 10 - 12, while Figure 13 shows the trends after conversion from relative photometric parallax and proper motion to distance and velocity. This information is presented in tabular form in Appendix G.

The distance conversion assumes the mean population lies at distance modulus $(m-M)_0 = 14.45$ (Ca14), converting to a reference distance ($D_0 = 7.76$ kpc) and assigning this distance to the ridgelines for the "metal-rich" and "metal-poor" samples.

Consistent with the simple treatment in Figure 9 and subsection 3.7, the "metal-rich" sample shows a higher-amplitude rotation curve than does the "metal-poor" sample, both with a steeper slope and about a factor ~ 2 greater difference in $\langle v_l \rangle$ between nearside

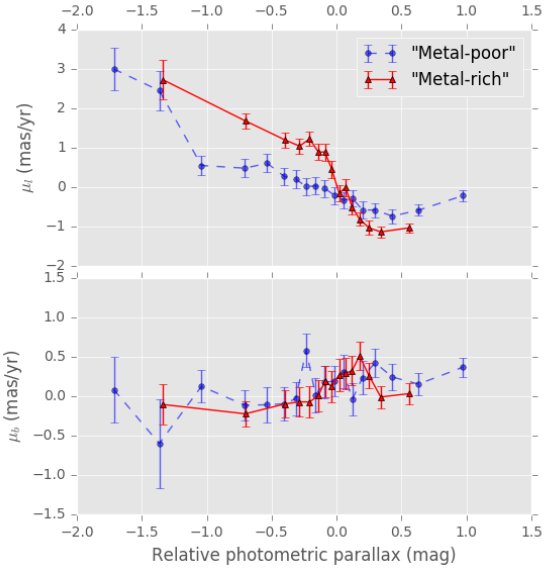

Figure 10. Variation of proper motion centroid with relative photometric parallax, for "metal-rich" (red triangles) and "metal-poor" (blue circles) samples, using a binning scheme with 200 objects per bin. The top row shows the proper motion centroid in Galactic longitude, the bottom row shows the proper motion centroid in Galactic latitude. Errorbars show 1σ uncertainties from parametric bootstrapping, using the best-fit parameters and measurement uncertainties to generate 1000 trial datasets for each distance bin. See subsection 4.1.

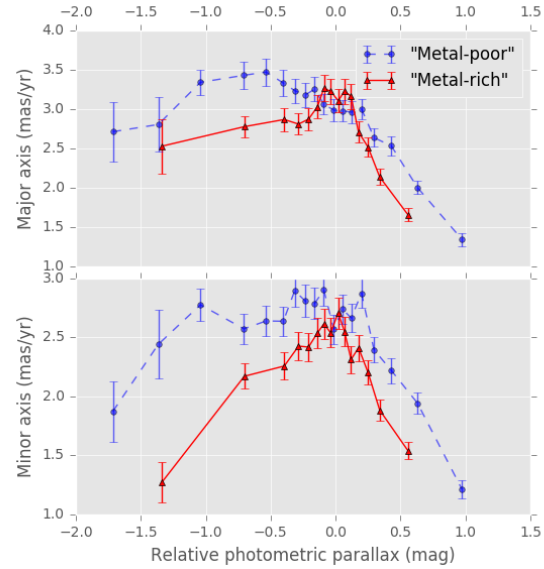

Figure 11. Semimajor (top) and semiminor (bottom) axis-lengths for the proper motion ellipse. Symbols, colors and errorbars as for Figure 10. See subsection 4.1.

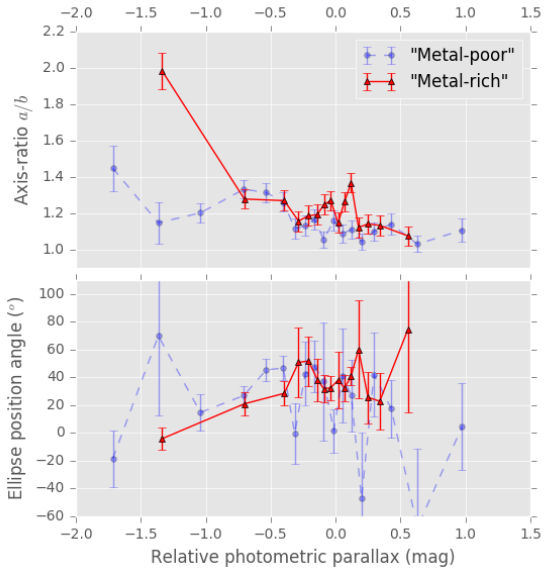

Figure 12. Variation of the proper motion ellipse axis ratio (top) and the position angle of its major axis (bottom) as a function of relative photometric parallax. Position angle $\theta = 0^\circ$ would mean the proper motion ellipse major axis aligns with the Galactic longitude axis. Symbols as Figure 10, with the "metal-poor" sample shown more faintly to avoid cluttering the plots. See subsection 4.1.

and farside of the bulge than for the "metal-poor" sample.

To quantify the rotation curve discrepancies between the samples, a simple straight-line model was fit to the rotation curves over the inner distance range ($6.4 \leq D \leq 8.0$ kpc). Since the "metal-rich" rotation curve visually appears to level off at smaller $|\pi'|$ than the "metal-poor" sample, the rotation curves to both samples were characterized over the same range in distance modulus. The 1σ ranges of $\langle \mu_l \rangle$ and $\langle v_l \rangle$ from the parametric bootstrap trials were used as estimates of measurement uncertainty in each distance-bin, and the inverse variance-weighted mean value of π' and D subtracted from the distance co-ordinates to minimze covariance in the fitted parameters. Trends were fitted to each of the (π', $\langle \mu_l \rangle$) and (D, $\langle v_l \rangle$) rotation curves separately (rather than transforming the proper motion trends into velocity trends after fitting). We did not attempt to deproject velocities to circular speeds (as discussed in Cl08) but merely attempted to characterize observed trends.

Figure 14 and Table 7 show the results. The difference in slopes is $\Delta(dv_l/dD) = -41.0 \pm 7.5$ km s^{-1} kpc^{-1} while the ratio of amplitudes is $A_{MR}/A_{MP} = 2.2 \pm 0.3$. Thus, a difference in rotation curve slopes is detected at approximately 5.5σ while a multiplication factor in the amplitude is detected at approximately 8.1σ.

Both the simple decomposition (subsection 3.7) and the fits of proper motion ellipses (subsection 3.8) suggest that the two rotation curves might intersect at slightly negative mean motion and slightly on the far-side of the Bulge (e.g. the right column of Figure 14). Since the proper motions are determined relative to the average observed bulge proper motion, across all metallicities, the proper motion zeropoint is therefore dependent on a range of selection and projection effects (see, for example, Ca14; Cl08, and Appendix A of López-Corredoira et al. 2007). Thus it is not surprising that the two sequences do not necessarily meet at $(\pi', \mu_l) = (0.0, 0.0)$.

The latitudinal motion curve (Figure 10, bottom panel) visually suggests a gentle trend from nearside to farside, consistent with previous measurements (e.g. Cl08, Soto et al. 2014). The behaviors of the two samples in μ_b are statistically similar, with slopes $dv_b/dD = -2.40 \pm 9.80$ km s^{-1} kpc^{-1} and $dv_b/dD = 22.4 \pm 6.53$ km s^{-1} kpc^{-1} for the "metal-rich" and "metal-poor" samples, respectively, corresponding to a slope difference of 20.0 ± 11.8 km s^{-1} kpc^{-1}. The samples have amplitude ratio $9.5/5.1 = 1.86 \pm 1.35$, which we do not consider to be a secure detection of differing rotation curve amplitude in the latitudinal direction.

4.2. *Proper motion ellipse morphology and amplitudes*

The velocity dispersion profiles (measured as major and minor axis lengths of the proper motion and velocity ellipsoids; Figures 11 & 13) also show differences between the samples. Both samples show a broadly centrally-peaked velocity dispersion pattern against line-of-sight distance (Figure 13), with the "metal-rich" sample showing a narrower peak, particularly in the major-axis dispersion. The "metal-rich" sample also shows generally lower velocity dispersion by $\sim 10\%$, particularly in terms of the velocity ellipse minor axis.

Consistent with previous studies (e.g. Soto et al. 2014), the proper motion ellipse appears to be weakly elongated, with the "metal-rich" population possibly the more elongated of the two samples (with axis-ratio $b/a \approx 1.25$ at $\pi' = 0$ compared to $b/a \approx 1.1$; see the top panel of Figure 12). The "metal-rich" population may show increased elongation for sample bins near the median distance.

The proper motion ellipse major axis position angle also shows trends with relative photometric parallax, although possibly at lower statistical significance than the trends reported in Cl08 despite a much longer time-baseline for proper motions (Ca14). This reduced significance may be due to the reduced sample size admitted by the cuts in [t], [m] employed in this work. It may be that only the "metal-rich" sample substantially

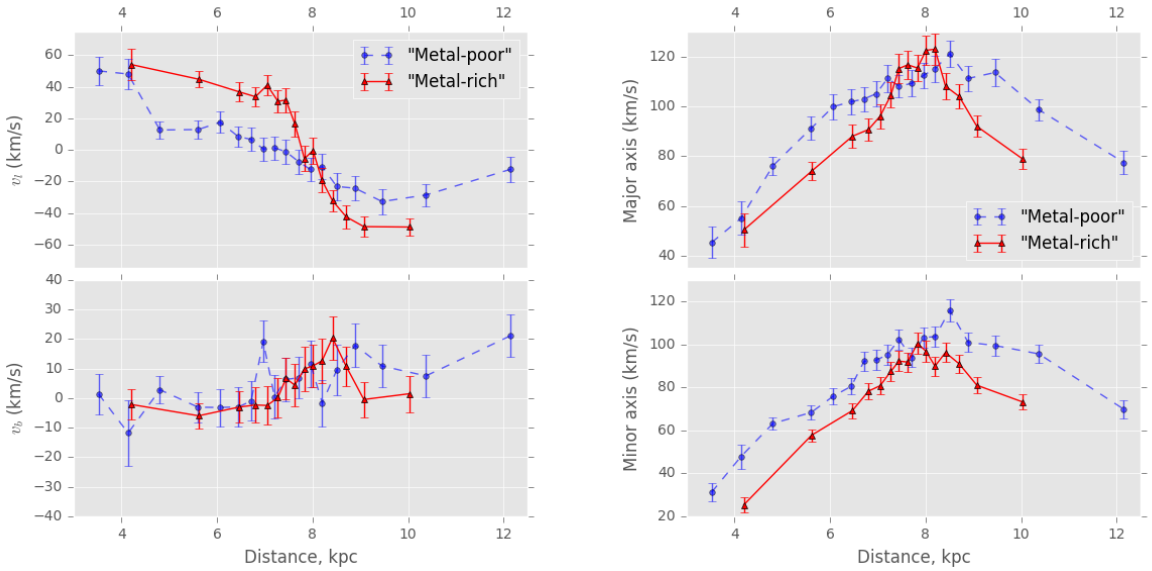

Figure 13. Transverse velocity ellipse centroids (left column) and axis lengths (right column) as a function of estimated line of sight distances. Symbols as Figures 10 & 11, except distance moduli have been converted to line of sight distances, and proper motions converted to velocities in km s^{-1}. See subsection 4.1.

Table 7. Trend parameters for the inner Bulge region. See subsection 4.1.

Sample	Gradient (μ_l) (mas yr^{-1} mag^{-1})	Amplitude (μ_l) (mas yr^{-1})	Gradient (v_l) (km s^{-1} kpc^{-1})	Amplitude (v_l) (km s^{-1})
"Metal-poor"	-1.54 ± 0.37	0.49 ± 0.06	-16.7 ± 3.65	20.2 ± 2.25
"Metal-rich"	-5.65 ± 0.61	1.20 ± 0.06	-57.7 ± 6.49	44.0 ± 2.29

shows the proper motion ellipse tilt with distance, with position angle rising to the $20° - 40°$ range (this tilt is strongly influenced by projection effects; see Section 5.1 and particularly equation (2) of Cl08 for discussion of these effects). Because the "metal-poor" population tends to be less elongated, its position angle trends are also detected at lower significance.

The very nearest relative photometric parallax bins show behavior consistent with a foreground population dominated by Galactic rotation. This seems particularly clear for the "metal-rich" sample, which shows a much more strongly elongated proper motion ellipse for the nearest bin ($a/b \approx 1.9 \pm 0.26$) and position angle consistent with zero (consistent with differential rotation in Galactic latitude).

5. DISCUSSION

The trends indicated by the union of the BTS and SWEEPS datasets, particularly the rotation curves (presented in Figures 9, 10 & 13), are quite striking. The "metal-rich" rotation curve appears to show systematically greater rotation amplitude than the "metal-poor" sample, shows a greater degree of central concentration along the line of sight (see Figure 13 as well as the raw distributions in Figure 8), and may show systematically lower velocity dispersion (Figure 13).

Before attempting to interpret the trends, however, we examine the magnitude and impact of several potential systematics that might bias the samples, whether by amplifying or even artificially generating the apparent trends in rotation curve (subsection 5.1), or by reducing them due to mixing in the ([t], [m]) space used to draw the "metal-rich" and "metal-poor" samples (subsection 5.2).

Implications of the relative photometric parallax distributions for the spatial distributions of the "metal-rich" and "metal-poor" samples are discussed in subsection 5.3, while subsection 5.4 discusses the implications of our results for the traditional selection of a "clean-bulge" sample using cuts on longitudinal proper motion μ_l.

Because a metal-poor kinematically-hot "Classical bulge" and/or "halo" bulge component may be present in the inner Milky Way (perhaps more likely among

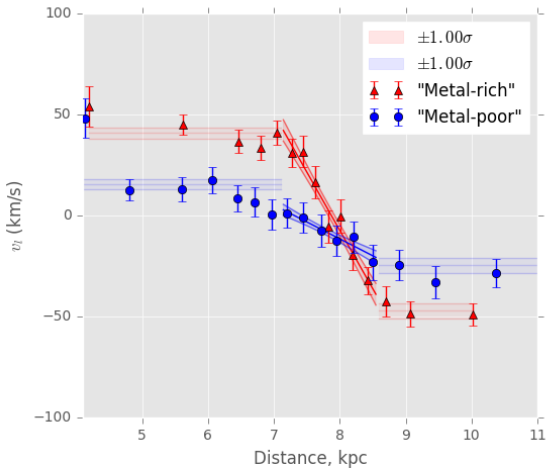

Figure 14. Straight-line fits to the inner region of the longitudinal rotation curve along the line of sight, after conversion to velocities and physical distances. The comparison-sequences for both samples are assumed to lie at distance $D_0 = 7.76$ kpc. The filled regions indicate $\pm 1.0\sigma$ regions for each sample. The horizontal shaded regions show the intervals assumed to be "flat" to estimate the rotation amplitude for each sample. See subsection 4.1 and Table 7.

"metal-poor" objects), we attempt in subsection 5.5 to dissect each of the "metal-rich" and "metal-poor" populations into two proper motion components per sample.

Finally, we address the question of whether the bulge rotation curve from proper motions indeed depends on relative abundance, in subsection 5.6, and briefly assess trends in proper motion dispersion in subsection 5.7.

5.1. *Difference amplification by photometric parallax mixing*

Throughout, relative photometric parallax (π') is estimated for each sample as the difference in apparent magnitude from a fiducial ridgeline tracing the median observed color and apparent magnitude in the SWEEPS color-magnitude diagram (Figure 7).

Differences in apparent magnitude distribution other than due to distance spread would contribute to differences in the inferred π' distributions for the "metal-rich" and "metal-poor" samples. If sufficiently severe, this differential blurring in π' might cause two identical rotation curves to be measured as discrepant. In the sense of our findings, the "metal-poor" sample might be artificially blurred in π' compared to the "metal-rich" sample, which would produce an *apparent* rotation curve discrepancy where none were present.

Several phenomena might lead the "metal-poor" sample to exhibit greater apparent magnitude scatter than the "metal-rich" sample. Firstly, since the "metal-poor" ridgeline in the SWEEPS CMD is slightly fainter than the "metal-rich" ridgeline, the "metal-poor" objects may be subject to increased photometric uncertainty. Secondly, at least in principle, if the extinction experienced by the "metal-poor" sample were in some way different to that experienced by the "metal-rich" sample, this could lead to a broader apparent magnitude distribution for the "metal-poor" sample. Thirdly, differences in binary fraction between the samples might cause the relative photometric parallax distribution of the two samples to differ, although the nature, magnitude and direction of such effects may be complex and indeed depend on the class of binaries probed (e.g. Gao et al. 2014).

Finally, differences in the *intrinsic* photometric scatter between the "metal-rich" and "metal-poor" samples might amplify differences between the rotation curves. Our own VLT spectroscopy, as well as spectroscopic campaigns from the literature (e.g. Zoccali et al. 2017; Hill et al. 2011) suggest that the [Fe/H] spread for the "metal-poor" population is greater than for the "metal-rich" population, which would in turn contribute greater π' scatter in the "metal-poor" population.

We have performed simple Monte Carlo tests to determine whether perturbations in the inferred distance distribution can be responsible for the differences in rotation curves between "metal-rich" and "metal-poor" samples. Appendices C and D provide details.

In the course of investigating the impact of the differential [Fe/H] distribution on the π' distribution, it became apparent that the BaSTI set of artificial stellar population methods used to generate synthetic [Fe/H] distributions, were (at the time of this work) imposing an apparently artificial population truncation. Section E provides details, with the method we adopted to mitigate this selection effect discussed in Appendix D.

Perturbations were tested due to additional photometric uncertainty or differential extinction variations (subsection C.1), differences in the fraction of unresolved binaries (subsection C.2), and, in the photometric parallax spread caused by differing intrinsic spreads in metallicity (Appendix D). In all three cases, the effect is either too small to bring the rotation curves into agreement (for binaries), or the required perturbation is too large to have gone un-noticed in previous studies (for extinction), possibly by an order of magnitude (for photometric uncertainty). The most substantial single contributor of relative photometric parallax mixing, is intrinsic difference in metallicity spread between the samples; this likely contributes differential distance-mixing up to a third the amount required to artificially reproduce the observed discrepancy in rotation curves. Since independent sources of additional photometric scatter

would presumably add in quadrature, their combination is very unlikely to be sufficient to bring about the observed discrepancies in trends.

We therefore conclude that differential distance scatter is not responsible for the difference in rotation curves or π' distributions, due to additional photometric uncertainty, differential extinction, differences in the unresolved binary populations, or in the differences in metallicity spread between samples.

5.2. *Difference reduction by sample cross-contamination*

While blurring in relative photometric parallax would tend to artificially increase the difference between trends in the "metal-rich" and "metal-poor" samples, cross-contamination of the samples in ([t], [m]) would tend to artificially reduce these differences. While we have used reasonably conservative thresholds in drawing our "metal-rich" and "metal-poor" samples, genuinely metal-rich objects might be moved into the "metal-poor" sample by measurement uncertainty, and vice versa.

Because of the complexities involved in rigorous reconstruction of the observed distributions (e.g. Gennaro et al. 2015), full exploration of this cross-contamination is deferred to future work. We have performed a simple Monte Carlo contamination test for the formal membership probability threshold $w_{ik} > 0.7$ used in this work (Appendix F).

Under the assumptions of that test, we find that the "metal-rich" sample is contaminated at the $\sim 8\%$ level (about half from the "metal-poor" sample), while the "metal-poor" sample is contaminated at the $\sim 5\%$ level (with $\lesssim 0.5\%$ due to the "metal-rich" sample). This is likely not severe enough for the observed low-amplitude "metal-poor" rotation curve to be entirely due to sample contamination from a small population of objects following the kinematics of the "metal-rich" sample.

5.3. *The line of sight distance distributions of the two samples*

The tendency of the "metal-poor" sample to show greater dispersion in relative photometric parallax (or, correspondingly, in distance D), is qualitatively consistent with the "kinematic fractionation" of Debattista et al. (2017). Identifying a "metal-poor" sample with an older population, this difference in line-of-sight distance distribution would also be qualitatively consistent with the observations of Catchpole et al. (2016), who find differing bar angles and degrees of central concentration for Mira variables of different ages. However, how the predictions of Catchpole et al. (2016) translate into predictions for the two samples here, is deferred to future work.

5.4. *Implications for proper motion selection*

Photometric studies of the Bulge typically impose a condition $\mu_l < -2.0$ mas yr^{-1} to isolate a clean bulge sample for further study (e.g. Kuijken & Rich 2002; Calamida et al. 2014). This procedure is appropriate because in the sight-lines typically studied near the Galactic center, the foreground disk population typically shows proper motion relative to the mean-bulge population of $\Delta\mu_l \approx +4$ mas yr^{-1}, as suggested by direct comparison of the proper motions of bulge giant branch stars with those of the upper main-sequence population of (mostly) disk foreground stars (e.g. Cl08, Soto et al. 2014).

To investigate whether and how this cut imposes selection effects on the two samples, we computed the sample counts, fractions and volume densities for objects that would pass the longitudinal proper motion cut ($\mu_l < -2.0$ mas yr^{-1}). The results are plotted in Figure 15 and presented in tabular form in Appendix G.

We find that the cut ($\mu < -2.0$ mas yr^{-1}) admits very few foreground objects from either sample; both samples show fewer than four objects passing this cut for the closest distances ($d \lesssim 4.49$ kpc and $\lesssim 4.25$ kpc for "metal-rich" and "metal-poor" samples, respectively, corresponding to the closest single and the closest two bins respectively; see Table 15 and Table 16 in Appendix G), while the foreground population's mean proper motion $\langle\mu_l\rangle$ climbs strongly for the closest distance bins (Figure 10). We therefore confirm that the traditional proper motion cut ($\mu < -2.0$ mas yr^{-1}) does indeed remove nearby objects cleanly for the SWEEPS field.[10]

Beyond this, however, the dissection by relative abundance has revealed several interesting selection effects among the kinematically-cleaned sample (Figure 15).

Firstly, as expected, there is a bias towards the far side of the bulge, but this bias is much stronger in the "metal-rich" sample than for the "metal-poor"; indeed the fraction of "metal-poor"objects passing the kinematic cut is almost flat with inferred distance between $d \lesssim 5$ kpc $\lesssim 9$ kpc.

Secondly, the raw counts of sources thus isolated in the "metal-rich" and "metal-poor" samples are of similar or-

[10] Strictly speaking, the classification of the nearest objects into "metal-rich" and "metal-poor" samples may suffer different selection effects to the rest of the samples because either or both of the stellar parameters and extinction might be different for the very nearest objects compared to the majority sample at more bulge-like distances. We are making the assumption that the relative classification of objects in the nearest distance bins, is still valid.

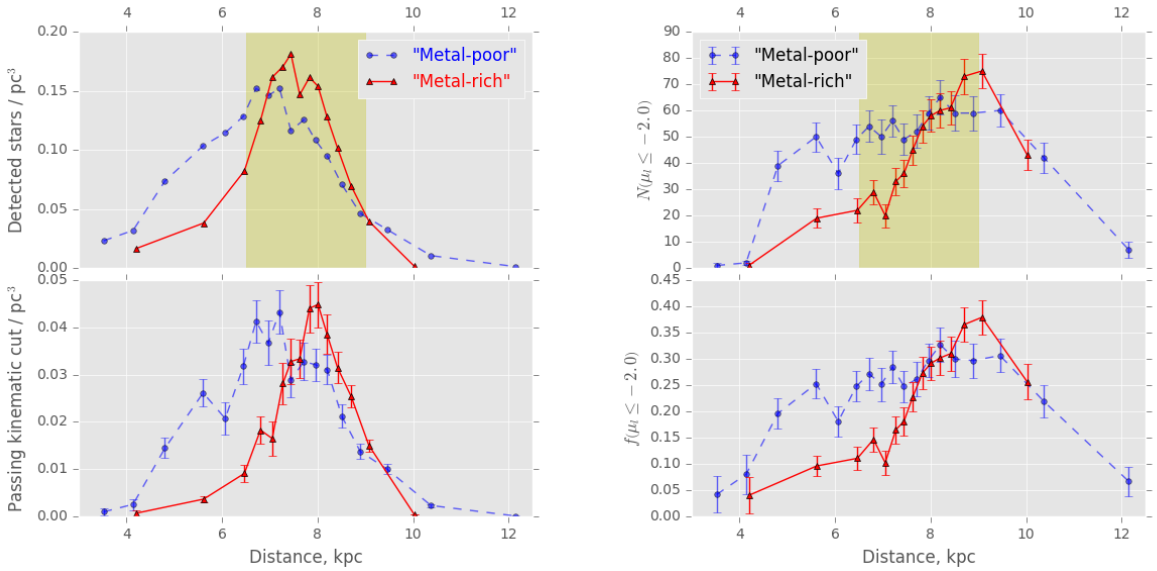

Figure 15. Selection functions imposed by the traditional kinematic cut $\mu_l \leq -2.0$ mas yr^{-1}, for the "metal-rich" (red triangles, solid line) and "metal-poor" (blue circles, dashed line) samples. *Left column:* volume density of all objects assigned to each sample (left-top) and which would pass the kinematic cut (bottom panel). *Right column:* number of objects per sample that would pass the kinematic cut (right-top) and the fraction (right-bottom) that would pass the cut. Each distance bin has the same number of detected objects by construction (subsection 3.8), so bootstrap uncertainty estimates are not applicable to the top-left panel. Because of this binning scheme, bins with the same counts generally do not indicate the same volume density of detected objects (between bins or between samples). The shaded yellow region represents inferred distances ($6.5 \leq d \leq 9.0$) kpc. For discussion, see subsection 5.4.

ders of magnitude. Considering sample sizes that pass the kinematic cut at inferred distances between 6.4 and 9.1 kpc (chosen to encompass the bulge populations; see Tables 15 and 16), the total counts in each sample are 566 ± 20 and 552 ± 20 for the "metal-rich" and "metal-poor"samples, respectively (the uncertainties, estimated from the quadrature sum of parametric bootstrap uncertainty estimates in these counts for each bin, are almost certainly underestimates). With total sample sizes within this distance range of 2381 (1984) for the "metal-rich" ("metal-poor") samples, this translates into fractions $24\% \pm 1\%$ ($28\% \pm 1\%$) of the "metal-rich" ("metal-poor") samples that pass the kinematic cut. Thus, *of objects in this distance range*, the kinematic cut appears to slightly favor the "metal-poor"sample, although the difference is small.

In principle, a population of compact objects among the foreground population, might fall into the farther distance-bins for the "metal-poor" sample [11], polluting a sample with bulge-like motions with a small population showing disk-like motions. However, with the foreground disk population at $\sim 10-15\%$ of the total, and with a substantial WD population perhaps unlikely for a typical "young" foreground population, we do not consider this a significant contaminant, and leave exploration of the impact of foreground WDs to future work.

[11] At colors typical of the "metal-poor" sample, the quiescent dwarf novae found by Ca14 at the distance of the bulge show F606W $\sim$ 28. Similar objects in a very nearby foreground disk population ($\lesssim$ 3 kpc) might fall within the faintest bins of our chosen sample.

5.5. *Are the metallicity-samples themselves composite?*

In addition to any continuous metallicity-velocity correlation, the samples may include populations from distinct entities within the Bulge region, whether interloper populations from the Halo (e.g. Koch et al. 2016) or any Thick-disk component (e.g. Ness et al. 2013a) or a small "Classical" bulge component (Kunder et al. 2016).

We have therefore performed the exercise of decomposing each of the "metal-rich" and "metal-poor" samples into two-component GMM's (in μ_l only), to determine if any minority component is distinguishable within the rotation curves formed from the two samples (figures 16 & 17).

No minority population is detected in either sample; indeed, when a two-component GMM is used, the two centroids track the mean rotation curve within each sample roughly symmetrically about the mean rotation curve, each sub-component has roughly equal weight in the mixture.

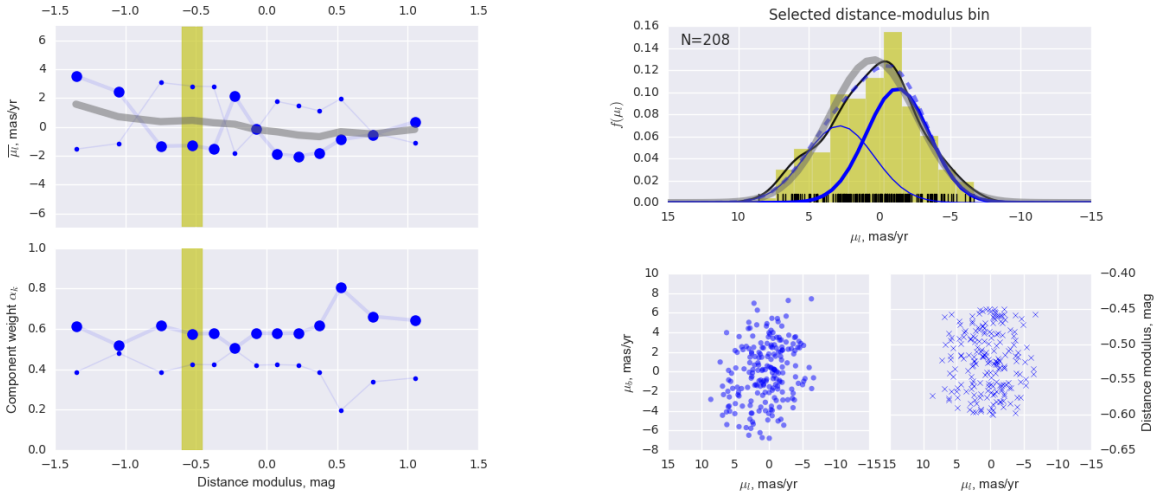

Figure 16. Representation of the "metal-poor" rotation curve as a two-component GMM in μ_l, to test the hypothesis that the "metal-poor" sample might itself be composite. *Left column:* rotation curve in μ_l as tracked by the two model components (*left top*), and the relative weights of the two model components (*left bottom*). Large dots indicate the more populous of the two model components in each bin ($\alpha_k = 0.75$ would mean three quarters of the sample came from model component k). The gray line in the left-top panel shows the rotation curve inferred using a single model component at each distance-bin. *Right column:* μ_l distribution for the bin indicated for the shaded distance-bin in the left-column. *Right top:* μ_l distribution (shaded histogram and thin black line), with the prediction of the two-component GMM (the thick and thin blue lines indicate the more- and less-populous model component, respectively, while the blue dashed line indicates the sum of the two). The gray thick line shows the prediction of the single-component model. The *bottom left* and *bottom right* panels show the vector point diagram and distance modulus distribution, respectively. See subsection 5.5.

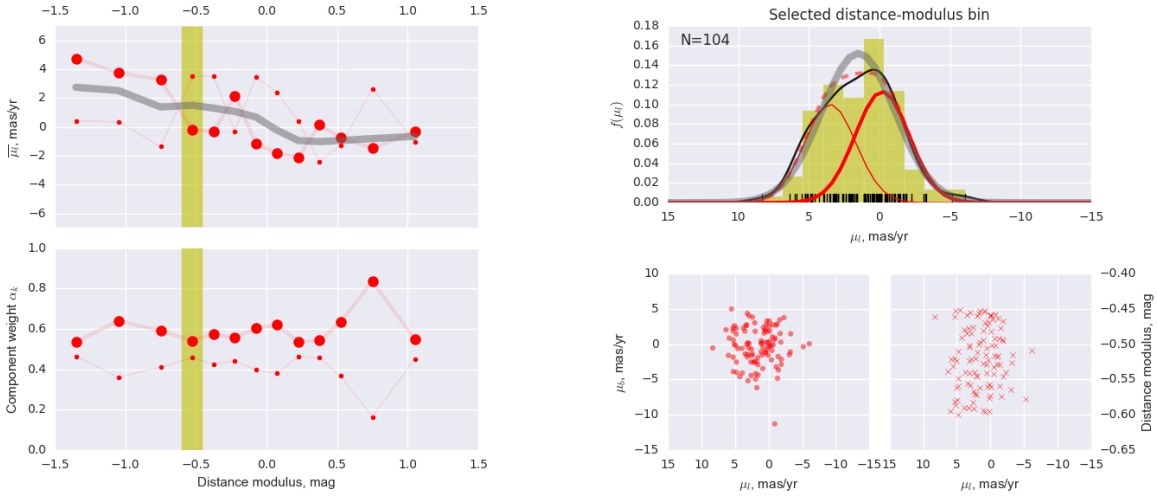

Figure 17. Representation of the "metal-rich" rotation curve as a two-component GMM in μ_l, to test the hypothesis that this sample might be a composite of two sub-populations. Symbols similar to Figure 16, except red symbols and lines are substituted for blue. See subsection 5.5.

We therefore conclude that a minority component with discrepant rotation curve is not required in either the "metal-rich" or "metal-poor" sample, but due to the small sample size ($\approx 2,000$ stars in total per sample), we cannot at this stage rule out its presence. Direct comparison with population models may allow upper limits to be set on the presence of any minority component within each sample, but this is deferred to future work.

5.6. *Does the proper motion rotation curve vary with* [Fe/H]*?*

We are finally in a position to answer the question posed by subsection 1.1. Our "metal-rich" and "metal-poor" rotation curves are inconsistent with each other at $\sim 5.5\sigma$ for the rotation curve slope and over 8σ for the nearside-farside rotation amplitude (subsection 4.1).

Here we briefly consider the implications of our results for the radial velocity-based rotation determinations. Of the radial velocity-based rotation curve estimates that probe bulge rotation curve differences with [Fe/H], only Zoccali et al. (2017) ventures as close to the Galactic midplane as the $b \approx -2.65°$ location of the SWEEPS field we report here; at $b \approx -2.0°$ Zoccali et al. (2017) find their metal-rich sample shows steeper slope (of mean radial velocity against Galactic longitude) by about 25%, at about 1.5σ significance. Thus, while we confirm the general features of the Zoccali et al. (2017) radial velocity results, rotation curve discrepancies are detected much more clearly, most likely due to selection effects that allow greater sensitivity to these differences.

The Zoccali et al. (2017) radial velocity-based rotation curves and our own proper motion-based rotation curves are somewhat in tension with the other radial velocity studies; while Williams et al. (2016) and particularly Ness et al. (2013b) do not show a metallicity-discrepancy in mean radial velocity against latitude, Kunder et al. (2016) show a very strong discrepancy (subsection 1.1). These three surveys all report results for Galactic latitudes $|b| \gtrsim 4.0°$, thus these discrepancies might indicate spatial variation in populations probed.

We also remind the reader that the radial velocity studes report line of sight depth-integrated averages for populations that are much rarer on the sky than the main sequence tracers we have used. Thus, the two classes of study may well trace different *intrinsic* behaviors, where it is the main sequence-based determinations that probe the detailed kinematic structure of the bulge most directly, particularly in regions near the Galactic center.

Having shown that the proper motion-based rotation curve does show discrepancy between "metal-rich" and "metal-poor" populations, the necessary next step is to extend our approach to more sight-lines within the inner bulge. By comparing metallicity-dissected proper motion-based rotation curves between fields, the trends with location in the bulge can be charted empirically, allowing a sharper test of the true variation of bulge rotation with the metallicity of the sample probed. This work is deferred to a future communication.

5.7. *Proper motion dispersion trends with photometric parallax*

Both the "metal-rich" and "metal-poor" samples show a clear central peak in latitudinal velocity dispersion $\sigma(v_l)$ near the photometric parallax interval where the samples are the most densely populated (Figure 13). The clear peak persists in longitudinal dispersion $\sigma(v_b)$ for the "metal-rich" sample, but is rather less clear in the "metal-poor" sample. This is broadly similar to the trends found from the combined population in previous studies (e.g. Cl08, Soto et al. 2014). That the proper motion dispersion of the "metal-poor" component is generally slightly larger than that of the "metal-rich" (particularly along the minor axis), is qualitatively consistent with expectations that a metal-poor, less rotationally-supported population should show higher velocity dispersion (e.g. Debattista et al. 2017; Ness et al. 2013b).

We may also be detecting the velocity-dispersion "inversion" detected at the inner-most fields in radial velocity studies (Babusiaux et al. 2014; Zoccali et al. 2017). Consistent with the low-latitude radial velocity dispersion trends, the proper motion-based velocity dispersion might also be greater for the "metal-rich" sample than for the "metal-poor" sample at the distance-bins closest to the center of the Bulge (see Figure 13. For the inner-most bulge regions, the proper motion-based "metal-rich" velocity dispersions also show steeper gradient than the "metal-poor", but with the gradient against line-of-sight distance rather than Galactic longitude, with the inner-most distance bin possibly showing slightly greater latitudinal velocity dispersion for the "metal-rich" sample.

6. CONCLUSIONS

We have performed an exploratory study to determine the utility of HST proper motions in charting the kinematic behaviors of "metal-rich" and "metal-poor" samples within the Galactic bulge from their proper motions, extending the rotation-curve technique first pioneered by Kuijken & Rich (2002). Merging the ultra-deep SWEEPS photometric and astrometric dataset communicated in Ca14 with the WFC3 Galactic Bulge Treasury Survey (Brown et al. 2010), "metal-rich" and

"metal-poor" samples were drawn using the [t], [m] indices of Brown et al. (2009), recomputed for the stellar parameters appropriate to the proper motion sample of interest and assuming $R_V = 2.5$, and the proper motion-based rotation curves determined from each sample using relative distance modulus as the depth co-ordinate. While detailed comparison to population models is deferred to future work, we draw the following conclusions at present:

- The union of SWEEPS and BTS datasets has revealed that indeed the "metal-rich" and "metal-poor" rotation curves are clearly discrepant from each other.
- Within 0.4 kpc from the median line of sight distance, the "metal-rich" population shows a steeper rotation curve in Galactic longitude by $\Delta(dv_l/dD) = -41.0 \pm 7.5$ km s^{-1} kpc^{-1} (i.e., a $\approx 5.5\sigma$ detection).
- The nearside-farside velocity amplitude is also determined to be discrepant; the rotation curve amplitude of the "metal-rich" sample has amplitude larger than that from the "metal-poor" sample by a factor $A_{MR}/A_{MP} = 2.2 \pm 0.3$ (a $\approx 8.1\sigma$ detection).
- While selection effects are likely complex, it does not appear to be possible to force the rotation curve of the "metal-rich" sample into consistency with that of the "metal-poor" sample by any reasonable observational perturbation of the "metal-rich" sample. Therefore, the differences in rotational behavior likely represent intrinsic behavior, *not* instrumental or observational artefacts.
- The behaviors of the two samples are qualitatively consistent with predictions from both observations and models, in which the "metal-poor" population shows a much weaker signature of rotation than the "metal-rich" sample.
- The velocity dispersion curve of both samples shows a clear peak at the line of sight distance where the samples are most dense. At the innermost distance-bins, the velocity dispersion of the "metal-rich" sample shows a steeper gradient than does the "metal-poor" sample, consistent with recent radial velocity studies.
- The traditional proper motion cut used to isolate a clean-bulge sample, $\mu_l < -2.0$ mas yr^{-1}, slightly over-selects "metal-poor" objects compared to "metal-rich", at the level of 28% compared to 24%.
- However, this selection effect is a function of relative photometric parallax; with this cut, the fraction of "metal-poor" objects selected is roughly constant while for the "metal-rich" population, the selection strongly prefers objects on the far side of the Bulge.

In addition, while exploring population systematics, we have found that:

- The current version of the widely-used BaSTI set of synthetic stellar population methods and isochrones appears to be imposing a truncation on populations near the edges of the [Fe/H] distribution found in the bulge; this includes a large part of the metallicity range traced by stellar halo models (e.g. An et al. 2013). Studies using BaSTI version 5.0.1. or earlier may be vulnerable to this truncation.

While the SWEEPS dataset represents the deepest (by far) set of images ever taken by HST towards the inner bulge, the typical apparent magnitude range probed by this study is shallow enough that we expect the techniques presented herein to be applicable to other fields for which ([t], [m]) are available. The extension of this work to the other fields in the BTS sample, is deferred to a future communication. This will provide a relatively model-independent set of observational constraints against which the trends from the most recent set of models can be compared, subjecting them to direct test. This will finally enable the Galactic bulge to be used as a quantitative test-case for the formation and development of galactic structure.

7. ACKNOWLEDGEMENTS

This work made use of the Hubble Legacy Archive, which is a collaboration between the Space Telescope Science Institute (STScI/NASA), the Space Telescope European Coordinating Facility (ST-ECF/ESA) and the Canadian Astronomy Data Centre (CADC/NRC/CSA). Support for programs 9750, 11664, 12586 and 13057 were provided by NASA through grants from STScI, which is operated by AURA, Inc., under NASA contract NAS 5-26555. This work is partly based on observations collected at the European Organisation for Astronomical Research in the Southern Hemisphere under ESO programme 073.C-0410(A).

WIC acknowledges support from the University of Michigan-Dearborn through departmental startup funds (project U039878), and from the Office of Research and Sponsored Programs (project U042549, *The Milky Way Bulge at UM-Dearborn*). WIC acknowledges equipment

funding from a Theodore Dunham, Jr. Grant from the Foundation Center. VPD is supported by STFC Consolidated grant ST/M000877/1. DM and MZ acknowledge support by the Ministry of Economy, Development, and Tourism's Millennium Science Initiative through grant IC120009, awarded to The Millennium Institute of Astrophysics (MAS), by Fondecyt Regular grants 1170121 and 1150345, and by the BASAL-CATA Center for Astrophysics and Associated Technologies PFB-06.

All the external software packages and methods used in this work are freely available to the community. This research made use of `Astropy`, a community-developed core Python package for Astronomy (Astropy collaboration, 2013).[12] This work made use of the `astroML` suite of tools for machine learning in Astronomy (Ivezić et al. 2014).[13] This work made use of `scikit-learn` (Pedregosa et al. 2011).[14] This work has made use of the `pysynphot` synthetic photometry utilities (STScI Development Team 2013).[15] This work has made use of BaSTI web tools (Pietrinferni et al. 2004).[16]

WIC thanks Jay Anderson, Andreas Koch, Jo Bovy and Oscar Gonzalez for enlightening interaction. We thank Santi Cassisi for assistance with the BaSTI synthetic stellar population tools, and for kindly providing custom synthetic populations at high metallicity.

Facilities: HST(ACS), HST(WFC3), VLT(UVES)

Software: Astropy, STSDAS, scikit-learn, astroML, BaSTI, pysynphot

REFERENCES

An, D., Beers, T. C., Johnson, J. A., et al. 2013, ApJ, 763, 65

Anderson, J., & King, I. R. 2006, PSFs, Photometry, and Astronomy for the ACS/WFC, Tech. rep.

Anderson, J., King, I. R., Richer, H. B., et al. 2008a, AJ, 135, 2114

Anderson, J., Sarajedini, A., Bedin, L. R., et al. 2008b, AJ, 135, 2055

Babusiaux, C. 2016, PASA, 33, e026

Babusiaux, C., Katz, D., Hill, V., et al. 2014, A&A, 563, A15

Bensby, T., Feltzing, S., Gould, A., et al. 2017, ArXiv e-prints, arXiv:1702.02971

Bishop, C. M. 2006, Pattern Recognition and Machine Learning (Information Science and Statistics) (Secaucus, NJ, USA: Springer-Verlag New York, Inc.)

Bovy, J., Hogg, D. W., & Roweis, S. T. 2011, Annals of Applied Statistics, 5, arXiv:0905.2979

Brown, T. M., Sahu, K., Zoccali, M., et al. 2009, AJ, 137, 3172

Brown, T. M., Sahu, K., Anderson, J., et al. 2010, ApJL, 725, L19

Calamida, A., Sahu, K. C., Anderson, J., et al. 2014, ApJ, 790, 164

Calamida, A., Sahu, K. C., Casertano, S., et al. 2015, ApJ, 810, 8

Cardelli, J. A., Clayton, G. C., & Mathis, J. S. 1989, ApJ, 345, 245

Catchpole, R. M., Whitelock, P. A., Feast, M. W., et al. 2016, MNRAS, 455, 2216

Clarkson, W., Sahu, K., Anderson, J., et al. 2008, ApJ, 684, 1110

Clarkson, W. I., Sahu, K. C., Anderson, J., et al. 2011, ApJ, 735, 37

Debattista, V. P., Ness, M., Gonzalez, O. A., et al. 2017, MNRAS, 469, 1587

Ferguson, J. W., Alexander, D. R., Allard, F., et al. 2005, ApJ, 623, 585

Fischer, D. A., & Valenti, J. 2005, ApJ, 622, 1102

Gao, S., Liu, C., Zhang, X., et al. 2014, ApJL, 788, L37

Gennaro, M., Tchernyshyov, K., Brown, T. M., & Gordon, K. D. 2015, ApJ, 808, 45

Gonzaga, S., & et al. 2012, The DrizzlePac Handbook

Gonzalez, O. A., Debattista, V. P., Ness, M., Erwin, P., & Gadotti, D. A. 2017, MNRAS, 466, L93

Gonzalez, O. A., Gadotti, D. A., Debattista, V. P., et al. 2016, A&A, 591, A7

Häfner, R., Evans, N. W., Dehnen, W., & Binney, J. 2000, MNRAS, 314, 433

Harding, P., & Morrison, H. 1993, in IAU Symposium, Vol. 153, Galactic Bulges, ed. H. Dejonghe & H. J. Habing, 297

Haywood, M., Di Matteo, P., Snaith, O., & Calamida, A. 2016, A&A, 593, A82

Hill, V., Lecureur, A., Gómez, A., et al. 2011, A&A, 534, A80

Howard, C. D., Rich, R. M., Clarkson, W., et al. 2009, ApJL, 702, L153

[12] http://www.astropy.org/index.html
[13] http://www.astroml.org/
[14] http://scikit-learn.org/stable/
[15] http://pysynphot.readthedocs.io/en/latest/
[16] http://basti.oa-teramo.inaf.it/index.html

Ivezić, Ž., Connolly, A., Vanderplas, J., & Gray, A. 2014, Statistics, Data Mining and Machine Learning in Astronomy (Princeton University Press)
Johnson, C. I., Rich, R. M., Kobayashi, C., et al. 2013, ApJ, 765, 157
Kains, N., Calamida, A., Sahu, K. C., et al. 2017, ApJ, 843, 145
Kinman, T. D., Feast, M. W., & Lasker, B. M. 1988, AJ, 95, 804
Koch, A., McWilliam, A., Preston, G. W., & Thompson, I. B. 2016, A&A, 587, A124
Kozhurina-Platais, V., Borncamp, D., Anderson, J., Grogin, N., & Hack, M. 2015, ACS/WFC Revised Geometric Distortion for DrizzlePac, Tech. rep.
Kozłowski, S., Woźniak, P. R., Mao, S., et al. 2006, MNRAS, 370, 435
Kroupa, P., Tout, C. A., & Gilmore, G. 1993, MNRAS, 262, 545
Kuijken, K. 2004, in Astronomical Society of the Pacific Conference Series, Vol. 317, Milky Way Surveys: The Structure and Evolution of our Galaxy, ed. D. Clemens, R. Shah, & T. Brainerd, 310
Kuijken, K., & Rich, R. M. 2002, AJ, 124, 2054
Kunder, A., Rich, R. M., Koch, A., et al. 2016, ApJL, 821, L25
López-Corredoira, M., Cabrera-Lavers, A., Mahoney, T. J., et al. 2007, AJ, 133, 154
Menzies, J. W. 1990, in European Southern Observatory Conference and Workshop Proceedings, Vol. 35, European Southern Observatory Conference and Workshop Proceedings, ed. B. J. Jarvis & D. M. Terndrup, 115–117
Minniti, D. 1996, ApJ, 459, 175
Mollá, M., Ferrini, F., & Gozzi, G. 2000, MNRAS, 316, 345
Nakada, Y., Onaka, T., Yamamura, I., et al. 1993, PASJ, 45, 179
Nataf, D. M. 2017, PASA, 34, e041
Nataf, D. M., & Gould, A. P. 2012, ApJL, 751, L39
Nataf, D. M., Gould, A., Fouqué, P., et al. 2013, ApJ, 769, 88
Nataf, D. M., Gonzalez, O. A., Casagrande, L., et al. 2016, MNRAS, 456, 2692
Ness, M., Freeman, K., Athanassoula, E., et al. 2013a, MNRAS, 430, 836
—. 2013b, MNRAS, 432, 2092
Pedregosa, F., Varoquaux, G., Gramfort, A., et al. 2011, Journal of Machine Learning Research, 12, 2825
Pietrinferni, A., Cassisi, S., Salaris, M., & Castelli, F. 2004, ApJ, 612, 168
—. 2006, ApJ, 642, 797
Poleski, R., Udalski, A., Gould, A., et al. 2013, ApJ, 776, 76
Rattenbury, N. J., Mao, S., Debattista, V. P., et al. 2007, MNRAS, 378, 1165
Rich, R. M. 1990, ApJ, 362, 604
Rich, R. M. 2015, in Astronomical Society of the Pacific Conference Series, Vol. 491, Fifty Years of Wide Field Studies in the Southern Hemisphere: Resolved Stellar Populations of the Galactic Bulge and Magellanic Clouds, ed. S. Points & A. Kunder, 59
Rocha-Pinto, H. J., Scalo, J., Maciel, W. J., & Flynn, C. 2000, A&A, 358, 869
Sahu, K. C., Casertano, S., Bond, H. E., et al. 2006, Nature, 443, 534
Sahu, K. C., Anderson, J., Casertano, S., et al. 2017, Science, 356, 1046
Schultheis, M., Rojas-Arriagada, A., García Pérez, A. E., et al. 2017, A&A, 600, A14
Sevenster, M. N., Chapman, J. M., Habing, H. J., Killeen, N. E. B., & Lindqvist, M. 1997, A&AS, 122, doi:10.1051/aas:1997294
Shen, J., Rich, R. M., Kormendy, J., et al. 2010, ApJL, 720, L72
Smith, L. C., Lucas, P. W., Kurtev, R., et al. 2017, ArXiv e-prints, arXiv:1710.08919
Soto, M., Rich, R. M., & Kuijken, K. 2007, ApJL, 665, L31
Soto, M., Zeballos, H., Kuijken, K., et al. 2014, A&A, 562, A41
Spaenhauer, A., Jones, B. F., & Whitford, A. E. 1992, AJ, 103, 297
Stetson, P. B. 1987, PASP, 99, 191
STScI Development Team. 2013, pysynphot: Synthetic photometry software package, Astrophysics Source Code Library, , , ascl:1303.023
Sumi, T., Wu, X., Udalski, A., et al. 2004, MNRAS, 348, 1439
Valenti, J. A., & Fischer, D. A. 2005, ApJS, 159, 141
van Loon, J. T., Gilmore, G. F., Omont, A., et al. 2003, MNRAS, 338, 857
Vanhollebeke, E., Groenewegen, M. A. T., & Girardi, L. 2009, A&A, 498, 95
Vásquez, S., Zoccali, M., Hill, V., et al. 2013, A&A, 555, A91
Vieira, K., Casetti-Dinescu, D. I., Méndez, R. A., et al. 2007, AJ, 134, 1432
Williams, A. A., Evans, N. W., Molloy, M., et al. 2016, ApJL, 824, L29
Zhao, H., Spergel, D. N., & Rich, R. M. 1994, AJ, 108, 2154
Zoccali, M., & Valenti, E. 2016, PASA, 33, e025
Zoccali, M., Renzini, A., Ortolani, S., et al. 2003, A&A, 399, 931

Zoccali, M., Vasquez, S., Gonzalez, O. A., et al. 2017, A&A, 599, A12

APPENDIX

A. GAUSSIAN MIXTURE MODELING

This work makes heavy use of Gaussian Mixture Modeling (GMM) to characterize overlapping populations in various spaces (e.g. subsection 3.3, subsection 3.6, subsection 3.8). GMM is a standard technique in unsupervised machine learning (e.g. Bishop 2006), with growing use in Astronomical data analysis (Ivezić et al. 2014 and Bovy et al. 2011 provide particularly clear and authoritative presentations of GMM in an astronomical context, including the extension of the methods to strongly non-uniform measurement uncertainty). Briefly, the likelihood is modeled as a sum of $(k = 1...K)$ Gaussian components, with the mixture weight α_k of each component (where $\Sigma_k^K \alpha_k = 1$) estimated by treating the unknown component identification of each object as a latent variable, fitting the mixture model components θ_k iteratively along with the mixture weights, usually using the Expectation Maximization algorithm or a variant thereof.

Under the GMM framework, we can write the formal membership probability w_{ik} that a given object belongs to each model component (the "responsibility" in the language of Bishop 2006), as

$$w_{ik} = \frac{\alpha_k p(\vec{x}_i|\theta_k, \mathbf{S}_i)}{\sum_{m=1}^{K} \alpha_m p(\vec{x_i}|\theta_m, \mathbf{S}_i)} \tag{A1}$$

(as has been common practice for decades in the field of globular cluster studies, under slightly different notation). Here $\vec{x_i}$ represents the measured co-ordinates of the i'th object, θ_k the components of the k'th model in the mixture (i.e., its mean and covariance matrix), α_k is the relative weight of the k'th model component, $\mathbf{S}_i$ the covariance matrix due to measurement uncertainty for the i'th object, and $p(\vec{x_i}|\theta_k, \mathbf{S}_i)$ the likelihood of measuring $\vec{x_i}$ given the k'th model parameters, assuming the object does belong to that component.

A.1. *Measurement uncertainties in* [t], [m]

From the definition of the [t], [m] indices (Equation 1), uncertainty propagation produces an approximation for the appropriate measurement uncertainty covariance $\mathbf{S}_i$ for each datapoint, which we reproduce here for convenience. We adopt

$$\mathbf{S}_i = \begin{pmatrix} \sigma_t^2 & \sigma_{tm}^2 \\ \sigma_{mt}^2 & \sigma_m^2 \end{pmatrix}_i = \begin{pmatrix} \sigma_V^2 + (1+\alpha)^2 \sigma_J^2 + \alpha^2 \sigma_H^2 & -(1+\beta)\sigma_V^2 \\ -(1+\beta)\sigma_V^2 & (1+\beta)^2 \sigma_V^2 + \sigma_C^2 + \beta^2 \sigma_I^2 \end{pmatrix}_i \tag{A2}$$

where $\left(\sigma_C^2, \sigma_V^2, \sigma_I^2, \sigma_J^2, \sigma_H^2\right)$ are the individual photometric uncertainty estimates in the BTS filters, and (α, β) the appropriate scale factors for the indices (Equation 1). Since $\alpha^2 >> (1+\beta)$ for these indices (for all populations of interest; Brown et al. 2009), we expect the covariance matrices for most of the stars to generally align with the [t] direction, with only weak uncertainty covariance. Indeed, this is usually the case, though there are exceptions (Figure 18).

We are also assuming the apparent magnitudes and their relevant linear combinations are Normally distributed, working in apparent magnitude space rather than flux space because the photometric uncertainties are already reported in magnitudes in the BTS catalog. We impose a photometric uncertainty cut of $\sigma < 0.1$ mag (Table 3) to reduce the number of objects that strongly violate this assumption. Nevertheless, long tails in the observed [t], [m] distribution for objects with relatively high photometric uncertainty may be expected.

A.2. *Proper motion measurement uncertainty*

Proper motion uncertainties from the 2004-2013 SWEEPS data are impacted by random uncertainties, by intrinsic velocity dispersion of the objects used to fit frame transformations when estimating proper motions, and by residual relative distortion between epochs.

As part of the investigation of the faintest detectable objects in the SWEEPS field, Ca15 performed extensive artificial star-tests including the injection of proper motions across the entire set of 2004-2013 epochs, yielding the run of random proper motion uncertainty in each co-ordinate with apparent magnitude, which we denote here as $\xi(F814W)$. While Ca15 thus produced separate estimates for uncertainties in the detector-X and detector-Y directions, for the apparent magnitude range of interest to this work the characterizations in the two directions are similar; in practice we use

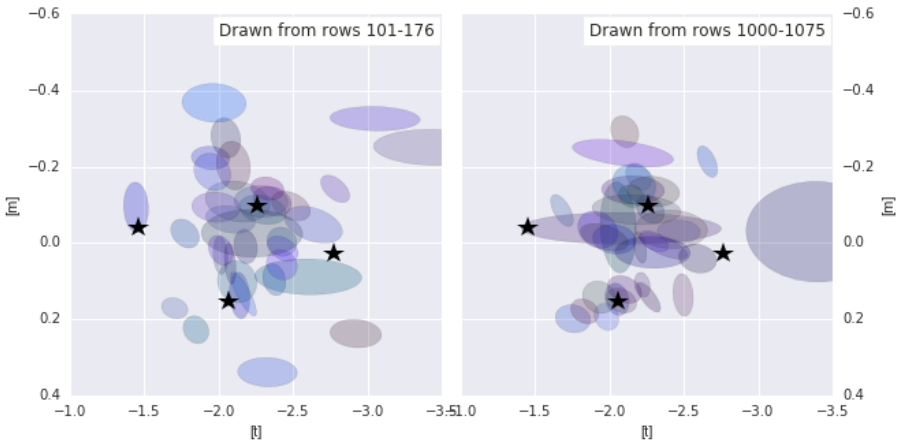

Figure 18. Covariance matrices $\mathbf{S}_i$ due to measurement uncertainty (following Equation A2), for a randomly-chosen selection of BTS measurements within the population selected for rotation-curve study (Figure 2). Black stars show the central locations of the mixture-model components. Because both [m] and [t] contain F555W measurements, an appreciable tilt in the covariance matrices is often present. In many cases, the near-infrared measurements dominate the uncertainty, as expected given the large value of the scale factor α in the definition of [t] (Equation 1). See discussion in Appendix A.

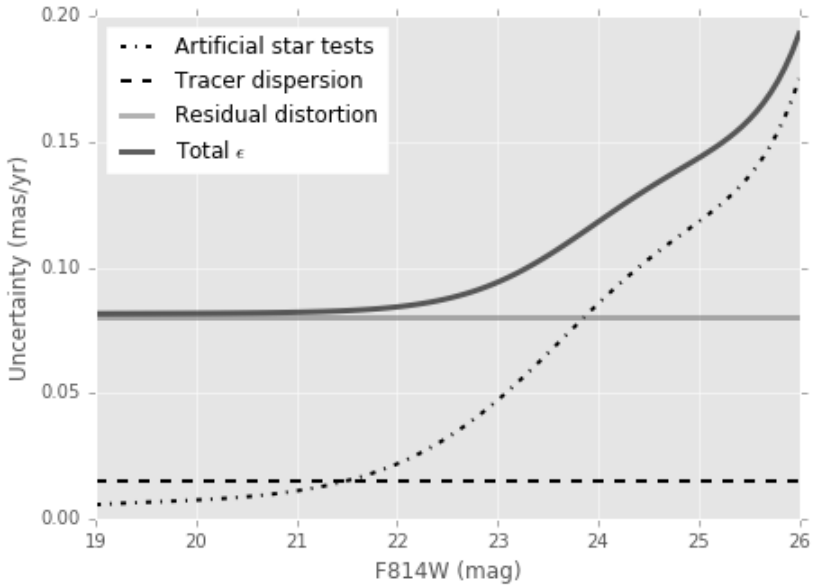

Figure 19. The run of adopted proper motion uncertainty (per co-ordinate) against F814W apparent magnitude, including random uncertainty suggested by artificial star tests (Calamida et al. 2015; dot-dashed line), the contribution due to intrinsic motion of the reference-frame tracer stars (dashed), and the estimated effect of residual differential distortion (grey solid line). See the discussion in subsection A.2.

the two runs in detector-X and detector-Y as separate samples of a symmetric underlying uncertainty distribution, characterizing $\log_{10}(\xi)$ as a fifth-order polynomial in F814W for rapid evaluation.

Improved characterization of residual distortion has also become available, as the datasets used to characterize ACS/WFC distortion have grown. In the SWEEPS filters, residual distortion is on the order of $\approx 0.01-0.02$ ACS/WFC pixels (0.5-1.0 mas at ≈ 50 mas pix^{-1}), with a complex pattern of variation with spatial scale roughly 150 ACS/WFC pixels (Kozhurina-Platais et al. 2015; Anderson & King 2006). This is consistent with a recent high-precision astromet-

ric characterization of the full set of SWEEPS epochs for astrometric microlensing (Kains et al. 2017), which indicated residual distortion corrections of $\approx \pm 0.02$ ACS/WFC pixels for the candidate astrometric microlensing sources (evaluated within 200 ACS/WFC pixels of each candidate; see Kains et al. 2017 for details), with the residual changing sign seasonally due to the mid-year 180° flip in HST's orientation angle for observations of this field. The observation dates of the 2011-2012-2013 epoch sample both HST orientations roughly equally, so the residual distortions in this epoch were to some extent averaged through when mean positions were computed per star, while central pointings in this epoch are typically within ~ 50 ACS/WFC pixels of the central pointing of the 2004 epoch. We therefore adopt $\Delta \approx 0.015$ pix (0.75 mas) as a reasonable estimate for the differential residual distortion suffered when proper motions are estimated across the two epochs.

For each object, then, the per-coordinate proper motion uncertainty ϵ_i can be estimated from the relation

$$\epsilon_i^2 \approx \xi(F814W_i)^2 + \frac{\sigma_{\rm pm}^2}{N_{\rm tr} - 2} + \left(\frac{\Delta_i}{\tau}\right)^2 \tag{A3}$$

where $\xi(F814W_i)$ is the artificial star-test random proper motion uncertainty estimate evaluated at the apparent magnitude of the object. $N_{\rm tr}$ is the number of tracer stars used to map the reference frames between epochs, and $\sigma_{\rm pm}$ the proper motion dispersion (in mas yr^{-1}) of the tracer stars (assumed to be estimated from the observed data, although if $N_{\rm tr}$ is large this assumption has little effect).[17] τ is the time-baseline for the two-epoch proper motions, and Δ_i is the positional offset (in mas) incurred at the detector due to differential residual distortion between the epochs, discussed above. (The third term Δ_i/τ in Equation A3 does not appear in equation (1) of Cl08 because local-transformations were used for that work to mitigate residual distortion.)

The random uncertainties $\xi(F814W_i)$ are small for most of the sample. Most of the objects selected for rotation curve analysis are in the range ($20.0 \leq F814W \leq 24.0$), for which the artificial star-tests of Ca15 suggest proper motion random uncertainty $0.008 \lesssim \xi_i \lesssim 0.09$ mas yr^{-1} per co-ordinate. For the second term in Equation A3, the number of tracers $N_{\rm tr}$ is large (on the order of $N_{\rm tr} \approx 4 \times 10^4$ since the full field of view was used to relate the reference frames of the 2004 and 2011-2012-2013 epochs), so the second term in Equation A3 evaluates to $\approx (0.015$ mas yr$^{-1})^2$. Finally, as discussed above, the typical magnitude and spatial scale of variation of residual distortion suggests $\Delta \approx 0.75$ mas, while the time baseline $\tau \approx 8.96$ years (Table 1) then suggests the third term in Equation A3 can be estimated as $(\Delta_i/\tau)^2 \approx (0.08$ mas yr$^{-1})^2$.

Figure 19 shows the adopted characterization of the proper motion uncertainty, plotted over an apparent magnitude range that encompasses the proper motion sample used herein ($20.5 \lesssim F814W \lesssim 25$). Differential residual distortion is likely the largest contributor to the proper motion uncertainty for most of the proper motion sample, although the random uncertainty becomes roughly as large at the faint end of the proper motion sample considered here.[18] Since the magnitude of the residual distortion Δ_i actually suffered by each object is unknown, some caution is warranted when interpreting the magnitude of the proper motion based velocity dispersion from these data. However, the total proper motion uncertainty estimates ($\epsilon_i \lesssim 0.13$ mas yr^{-1}) are still far smaller than the intrinsic proper motion dispersion of the bulge (~ 3 mas yr^{-1}) and so the reported trends should be reasonably robust against proper motion measurement uncertainty.

B. SPECTROSCOPIC ESTIMATE OF THE [Fe/H] SPREAD IN SWEEPS-FIELD BULGE STARS

An estimate of the spectroscopic metallicity distribution in this field is useful to calibrate synthetic stellar populations when investigating possible systematic effects. To perform this estimate, we use a deep set of VLT spectroscopic observations originally performed to provide radial-velocity follow-up to the SWEEPS transiting planet candidates; details can be found in Sa06, here we outline the relevant features for the present paper.

B.1. *Spectroscopic observations of the SWEEPS field*

Fiber-fed echelle spectroscopy were taken using *UVES* between 2004 June 22-25 (ESO program 073.C-0410(A), PI Dante Minniti). [M/H] estimates were produced in a similar manner to the analysis in Fischer & Valenti (2005) and Valenti & Fischer (2005); typically ~ 50 absorption features from a Solar spectrum (numerically degraded to the

[17] Because the artificial star tests inject few enough stars per trial to avoid altering the image crowding, they do not significantly alter the sample of moving tracer stars used to map reference frames between epochs when recovering injected proper motion; thus, artificial star tests are only minimally sensitive to $\sigma_{\rm pm}$.

[18] Note that random uncertainty will dominate the proper motion uncertainty for $F814W \gtrsim 25$; thus the artificial star tests of Ca15 do indeed capture nearly all of the proper motion uncertainty appropriate for the white dwarfs of Ca14 and the low-mass end of the MS charted in Ca15.

Table 8. GMM fits to the SWEEPS spectroscopic sample of 93 likely-bulge objects.Two GMM implementations are reported: "XD" refers to the `scikit-learn XDGMM` implementation while "ED" refers to the `extreme-deconvolution` method of Bovy et al. (2011). Reported ranges denote the standard deviation over 500 non-parametric bootstrap resampling trials. Parameter-sets are reported for 2- and 3-component mixture models.

k	α_k (XD)	$[Fe/H]_0$ (XD)	$\sigma_{[Fe/H]}$ (XD)	α_k (ED)	$[Fe/H]_0$ (ED)	$\sigma_{[Fe/H]}$ (ED)
1	0.31 ± 0.049	-0.42 ± 0.079	0.24 ± 0.059	0.26 ± 0.057	-0.49 ± 0.056	0.16 ± 0.042
2	0.69 ± 0.049	0.24 ± 0.025	0.19 ± 0.020	0.74 ± 0.057	0.22 ± 0.027	0.19 ± 0.023
1	0.28 ± 0.046	-0.48 ± 0.049	0.17 ± 0.041	0.28 ± 0.059	-0.48 ± 0.061	0.17 ± 0.044
2	0.36 ± 0.086	0.13 ± 0.068	0.12 ± 0.062	0.27 ± 0.202	0.11 ± 0.110	0.11 ± 0.075
3	0.36 ± 0.086	0.34 ± 0.052	0.17 ± 0.039	0.45 ± 0.209	0.31 ± 0.176	0.18 ± 0.074

spectral resolution of the observations) are scaled and shifted to find the best match to the observed spectra. In addition to radial velocities, this process also yielded estimates for [M/H] (as well as $\log(g)$ and $T_{\rm eff}$). The [M/H] determination used mainly metal lines, with very few C and O lines in the templates used, which reduces sensitivity in the [M/H] estimates to systematic differences between giants and main sequence objects (Valenti & Fischer 2005).

The 123 objects in the resulting catalog were trimmed by longitudinal proper motion ($\mu_l < -2.0$ mas yr^{-1}) to produce a sample of 93 likely-bulge objects with spectroscopic [M/H] estimates.

B.2. *GMM characterization of the VLT spectroscopic sample*

Following previous works, which use multi-component Gaussian mixtures to model the [Fe/H] distributions (e.g. Zoccali et al. 2017; Schultheis et al. 2017; Hill et al. 2011), we also characterize the abundance distribution of the 93 spectroscopically-measured likely-bulge objects (subsection B.1) as a Gaussian mixture (Figure 20). Two implementations of GMM with uncertainties are used; the `extreme-deconvolution` method of Bovy et al. (2011), and `scikit-learn XDGMM` (Pedregosa et al. 2011). The parameters fitted by the two implementations are generally consistent with each other, and are shown in Figure 20 and Table 8.

Although the 93 objects have somewhat limited statistical power to distinguish models, it does appear that at least a two-component mixture is preferred. At four or more components, both implementations always include a very broad, almost insignificant component, which suggests over-fitting - and indeed the AIC and BIC do not suggest more than two components are required by these data (Figure 20, right column).

The parameters of the two-component GMM are consistent with those reported by spectroscopic surveys of nearby fields (e.g. Zoccali et al. 2017; Schultheis et al. 2017), both of which find at least two spectroscopic components with similar fractions α_k, centroids, and dispersions. The sample does not include a more metal-poor component that might be suggestive of a Halo component (e.g. Schultheis et al. 2017; Ness et al. 2013a).

C. DIFFERENTIAL SPREAD IN PHOTOMETRIC PARALLAX

Since the distance determination is based on relative photometric parallax (π'), in principle the "metal-poor" population might be subject to additional photometric scatter that causes it to be more mixed in *apparent* distance than the "metal-rich" population (subsection 5.1). Might differential distance blurring be responsible for the apparent differences in rotation curves, even if the *intrinsic* kinematic trends for both samples were identical?

To address this question, we perform simple Monte Carlo tests, communicated in this section. Differences in *absolute* magnitude distribution due to the differing stellar parameter ranges between the selected samples - particularly [Fe/H] - require a more sophisticated analysis and are discussed in Appendix D.

Individual objects in the "metal-rich" sample are perturbed in apparent magnitude and the proper motion rotation curve for the distance-blurred "metal-poor" sample compared to the observed rotation curve for the "metal-poor"sample, by computing and comparing the smoothed rotation curves between distance moduli ($-1.0 \leq \pi' \leq +1.0$) for both samples.

For each form of distance-modulus blurring, a run of 30 effect scales are considered. A thousand realizations were run at each of the effect scales, and the match between the distance-blurred "metal-rich" and the observed "metal-

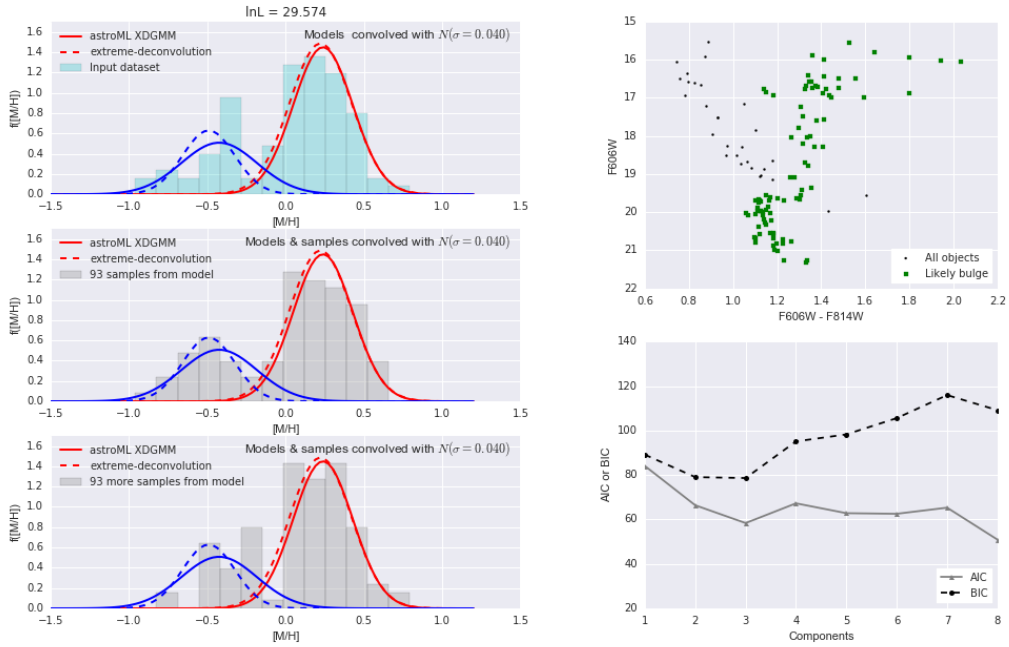

Figure 20. *Left column:* GMM decomposition of the 93 kinematically-identified bulge objects with spectroscopic [Fe/H] estimates (subsection B.1). *Left:* visualization of a two-component GMM fit to the individual datapoints, over the histogram of the samples (left-top) and two realizations of the GMM model (left-middle and left-bottom). Solid lines refer to the model fit with the `scikit-learn XDGMM` implementation (Pedregosa et al. 2011), while dashed lines show the parameteres fit using the `extreme-deconvolution` implementation of Bovy et al. (2011). The algorithm fits the underlying model distribution after correction for measurement uncertainty; the models and model samples have therefore been convolved with a Gaussian with the median measurement uncertainty for visualization. See Figure 20 and Appendix B. *Right column:* Sample selection and mixture fit-criteria for the characterization of the *VLT* spectroscopic abundance estimates (subsection B.1). *Top panel:* SWEEPS color-magnitude diagram showing all 123 spectroscopically-sampled objects (black points) and the subset of 93 objects kinematically identified with the Bulge (green squares). The bulge main sequence turn-off, giant branch, and disk main sequence are each apparent. *Bottom:* the variation of formal figures of merit as a function of the number of model components. See Figure 20 and Appendix B.

poor" rotation curves evaluated. Three figures of merit are assessed: (i) The root-mean-square difference between the two trends is used as the primary badness-of-match statistic, where the longitudinal proper motion offset between the two observed trends ($\approx +0.4$ mas yr^{-1}) is subtracted from the "metal-rich" sample to ease interpretation (so that a perfect match between the two trends would produce badness-of-match value zero). In addition, the difference in distribution of π' between the blurred-"metal-rich" and observed "metal-poor" samples is quantified by the difference in (ii) the π' standard deviations for each distribution, and (iii) the skewness of the two π' distributions, since the observed "metal-poor" distance modulus distribution does exhibit an asymmetry towards the near-side of the median population (e.g. Figures 8 & 9).

To determine the ranges of these figures of merit that would be consistent with a match, for every trial a control test is performed. A set of π' values is drawn following the observed distribution of π' values for the "metal-poor" sample, and the observed "metal-poor" rotation curve (and proper motion dispersion curve) sampled at the generated π' values. For this generated sample, the rotation curve and comparison statistics are obtained exactly as for the blurred-"metal-rich" sample. In this way, the figures of merit are also produced for a set of samples when the "metal-poor" distribution is compared against a statistical clone of itself, allowing the range of badness-of-fit values to be charted that suggest the underlying samples are drawn from the same distribution.

Two forms of potential distance-modulus blurring are considered independently. Additional scatter in the intrinsic flux distribution is discussed in subsection C.1, which accounts for additional photometric uncertainty or differences

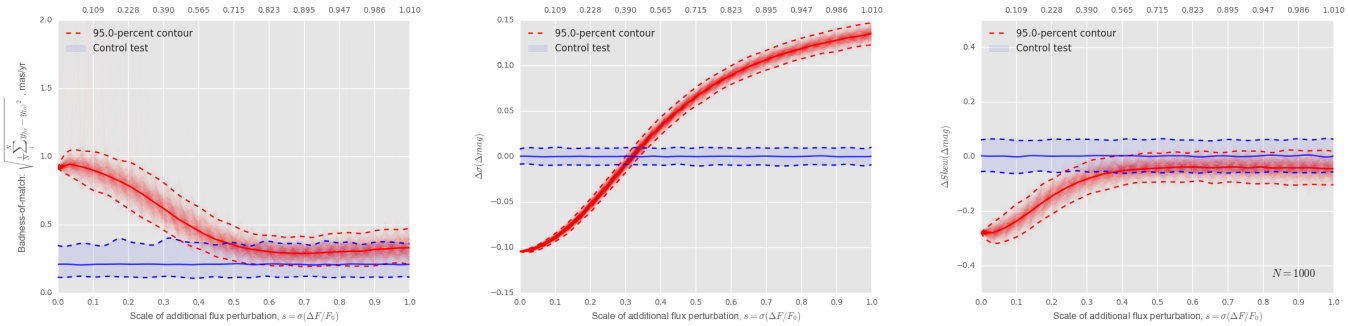

Figure 21. Testing the hypothesis that additional flux scatter ΔF can by itself cause identical rotation curves and π' distributions to exhibit the observed discrepancies between "metal-poor" and "metal-rich" samples. In each panel, the lower horizontal axes each show the scale s of the fractional flux perturbation, while the upper horizontal axes show $s_{\rm mag}$, the corresponding sample standard deviation in apparent magnitude. Reading left-right, panels show the badness-of-match statistic, the difference in distance modulus standard deviations, and the difference in distance modulus skewness, respectively. Solid red lines show the median of each statistic, and 95% of the samples fall within the dashed contours. The blue shaded region and contours show the control test. See subsection C.1.

in extinction (or indeed any perturbation that would lead to an additional flux perturbation of the same general form). The impact of differing binary fraction is discussed separately in subsection C.2, because its imprint on the flux distribution takes a different form.

C.1. *Additional photometric scatter in the "metal-poor" population*

Additional photometric scatter is simulated as a perturbation in flux. The apparent magnitudes in the "metal-rich" sample are perturbed by amount Δm_p, defined as

$$\begin{aligned}\Delta m_{p,i} &= -2.5\log_{10}\left(\frac{F_{0,i}+\Delta F_i}{F_{0,i}}\right)\\ &= -2.5\log_{10}\left(1+s\mathcal{N}(0,1)_i\right)\end{aligned} \tag{C4}$$

where ΔF_i is the perturbation in flux, assumed Normally distributed, s the scale of the additional flux uncertainty as a multiple of the original unperturbed flux $F_{0,i}$ and $\mathcal{N}(0,1)_i$ a draw from the unit Normal distribution. For large values of s, the Normally distributed flux perturbation can cause the perturbed flux values for some simulated objects to go negative; the simulation treats these cases as nondetections and removes affected objects from consideration, thus penalizing simulations with very large simulated flux uncertainty.

Figure 21 shows indications from this test. The rotation curve badness-of-match statistic suggests observed rotation curve discrepancy can result from increased photometric scatter for scale factor $s \gtrsim 0.35$ (in apparent magnitude, $s_{\rm mag} \gtrsim 0.48$) while the π' distribution of the "metal-poor" sample is brought into rough agreement with that observed, for scale factor range $0.25 \lesssim s \lesssim 0.35$ (or in magnitudes, $0.30 \lesssim s_{\rm mag} \lesssim 0.48$).

To aid interpretation in terms of apparent magnitude, we also characterize the sample standard deviation in apparent magnitude caused by the perturbation (which we denote $s_{\rm mag}$), displaying it alongside the input scale s of flux perturbation; the quantity $s_{\rm mag}$ is plotted along the top axes in Figure 21.

It is difficult to see how the "metal-poor" sample might be subject to such a large additional photometric scatter. For example, the additional photometric scatter is likely far larger than the difference in photometric precision in the two samples from the SWEEPS measurements. Figure 22 shows the *internal* photometric precision (defined as the root-mean-square of the apparent magnitude measurements along the set of images) as a function of apparent magnitude and π' for objects in the "metal-rich" and "metal-poor" samples. The "metal-poor" population shows only a slight increase in internal photometric uncertainty compared to the "metal-rich" population, and both are very small (on the order of a few mmag; these objects are well above the photometric completeness limit for the SWEEPS survey). While indeed the internal precision refers to the *random* component of photometric uncertainty and not the absolute photometric accuracy, a sample difference in photometric uncertainty of $\sim 0.3-0.5$ magnitudes seems highly unlikely for these data.

A difference in extinction distribution between the samples, characterized in any way (e.g. by change in $E(B-V)$, in R_V, or by functional form such as introducing and varying a second parameter), if large enough to bring about the

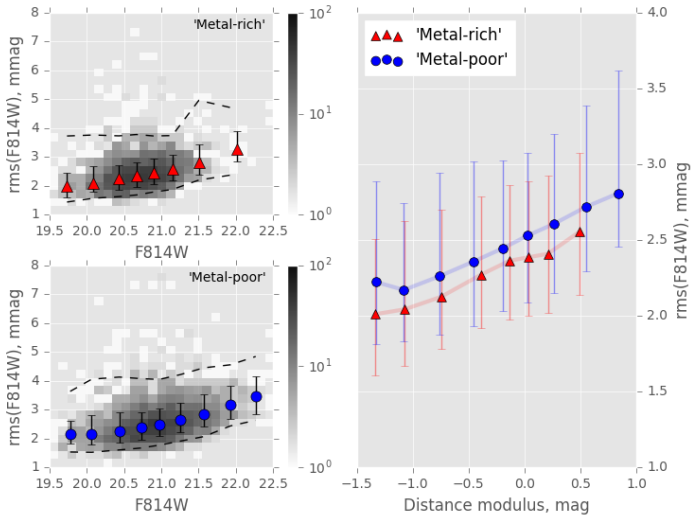

Figure 22. Comparison of internal photometric precision for the "metal-rich" and "metal-poor" samples as a function of apparent magnitude (left) and distance modulus (right). Errorbars indicate the upper- and lower-bounds within which 68% of objects are found in each bin, the dashed contours encompass 95% of objects per bin and the plot symbols show the medians. The grayscale shows object counts in the two samples, on a logarithmic scale. See subsection C.1.

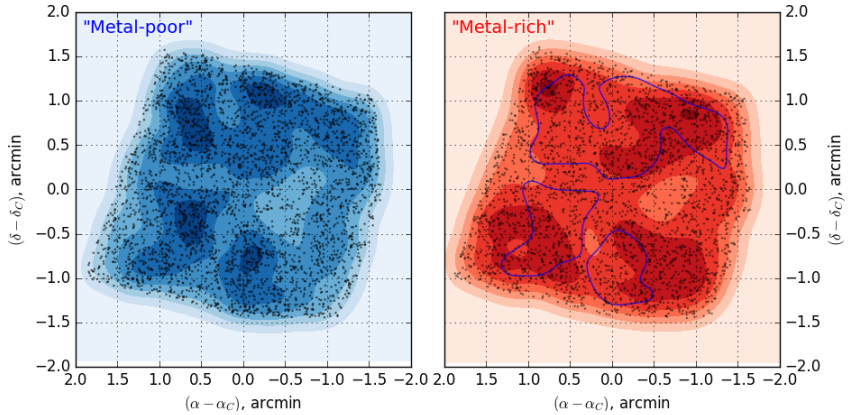

Figure 23. Spatial distributions of the "metal-poor" (blue, left) and "metal-rich" (red, right) populations discussed in subsection 3.6, over the $\sim (3' \times 3')$ of the BTS-SWEEPS cross-matched field. In each panel, points represent the individual objects, while the filled contours indicate the KDE representation of the local density at each point. In both panels, contours correspond to six equally-spaced density levels. To aid visual comparison, the outer contour of the second-highest level from the metal-poor population is plotted over the metal-rich distribution in the right-hand panel. See subsection 3.6.

$s_{\rm mag} \sim 0.3-0.5$-magnitude additional scatter required, would surely have led to additional observational consequences that are not seen in these data.

For example, the observed F814W dispersion of the Red Clump Giants (RCG) in the SWEEPS dataset is close to $\sigma(F814W) \approx 0.17$ magnitudes (Cl08). Even if *all* this dispersion were due to extinction, which seems unlikely, this would still be a factor $\gtrsim 2$ too low to bring about the observed discrepancies between "metal-rich" and "metal-poor" samples.

When the depth of the bulge along the line of sight is considered, the allowed contribution of differential extinction to π' blurring becomes somewhat smaller. For example, assuming the bulge RCG are scattered along this line of sight by ± 0.50 kpc allows room for only 0.1 mag of photometric blurring due to extinction of any prescription. Since

extinction effects would need to apply *differentially* to the "metal-poor" sample compared to the "metal-rich" sample to bring the two rotation curves into agreement, we conclude that differential extinction effects are likely at least a factor 3-5 too small to account for the observed rotation curve discrepancy.

Secondly, it is not clear why the "metal-poor" sample would be subject to a strongly discrepant extinction distribution (however parameterized) in the first place. The two populations are not strongly different in their projected distributions on the sky (Figure 23), which would seem to argue against, say, the "metal-poor" sample being located within a region on the sky showing stronger, clumpier extinction than the "metal-rich" sample. Additionally, the RCG apparent magnitude distribution in this field does not appear to be bimodal (e.g. Nataf et al. 2013; Clarkson et al. 2011).

We point out that this test applies to the *dispersion* of differential extinction, not to differences in the median extinction between the two samples. Although a difference in median R_V might affect the drawing of the "metal-rich" and "metal-poor" samples using [m], [t] (because those indices are computed in terms of extinction ratios, which are dependent on the prescription for extinction), it would not by itself change the π' dispersion for a given population (R_V variations are considered in more detail in subsection D.5). The π' values for "metal-rich" and "metal-poor" populations are both constructed by reference to the *observed* median loci in the SWEEPS color-magnitude diagram. While the interpretation of a given locus with a particular set of population parameters (like [Fe/H], $E(B-V)$, f_{bin}, q_{min}, and to a lesser extent for this CMD region, age) does depend on the median $E(B-V)$, this does not impact the locus of the observed median populations on the SWEEPS color magnitude diagram.

We thus reject additional photometric scatter as a cause for the "metal-rich" and the "metal-poor" samples to be drawn from the same kinematic population, because, whatever the cause, its likely magnitude is much too low to have gone unnoticed elsewhere in these data.

C.2. *Differences in binary fraction*

If the "metal-poor" sample has a highly discrepant binary fraction or binary companion mass ratio distribution from the "metal-rich" sample, then this might produce a population with larger distance-spread, where the additional inferred distance scatter would be biased to closer distances than the mean-population - qualitatively similar to the trends observed (e.g. Figure 9).

The binary fraction f_{bin}, minimum binary (initial) mass ratio q_{min} and indeed the shape of the distribution of mass ratio q, are not known for the bulge (see, e.g. Calamida et al. 2015), and are difficult to constrain observationally for the sample selected for the present proper motion study (e.g. Figure 2).

A complete search of (f_{bin}, q_{min}) parameter space, and indeed of the form of the mass ratio distribution, is beyond the scope of the present investigation. Instead, we characterize statistically the distribution of Δm_{bin} due to unresolved binaries, for the CMD region of interest to this study (Figure 2), and draw from this distribution $f(\Delta m_{bin})$ for each realization of the Monte Carlo trial.

To maximize the impact of a difference in binary fraction between the "metal-rich" and "metal-poor" samples, we assume for the purposes of this test that the "metal-rich" population has no binaries at all, and perturb it using an unresolved binary fraction to approximate the "metal-poor" population. (This thus allows the excess binary fraction to be tested in the range $0 \leq f_{bin} \leq 1$; if we assume the "metal-rich" sample has a binary fraction of 0.3, then only tests in the range $f_{bin} < 0.7$ would be meaningful). We also assume for this test that it is *only* the population of unresolved binaries that differs between the two samples (i.e. there is no difference in metallicity distribution between the two samples).

Version 5.0.1. of the BaSTI[19] suite of simulation tools and stellar population models (Pietrinferni et al. 2004, 2006) is used to produce a representative set of distributions $f(\Delta m_{bin})$, to characterize for the Monte Carlo draws. Thanks to the capability of BaSTI to accept user-defined random number seeds, simulations that are almost identical but for small changes in input parameters can be run. This allows us to compare synthetic populations on a star-by-star basis, with and without the addition of unresolved binaries.[20]

To combine the sophistication of BaSTI with the speed necessary for Monte Carlo trials, the distribution $f(\Delta m_{bin})$ itself is characterized non-parametrically, using the method outlined in Ivezić et al. (2014, their Section 3.7) - and thus does not depend on a functional form for $f(\Delta m_{bin})$. This resampling is 10^{5-6} times faster than running a BaSTI sim-

[19] http://basti.oa-teramo.inaf.it/

[20] The populations returned by BaSTI are not quite identical for identical random number seeds; $\sim 1/1000$ of the objects in the binary-free simulation are missing in the binary-equipped simulation. Thus re-matching of rows across simulations is required even for identical seeds.

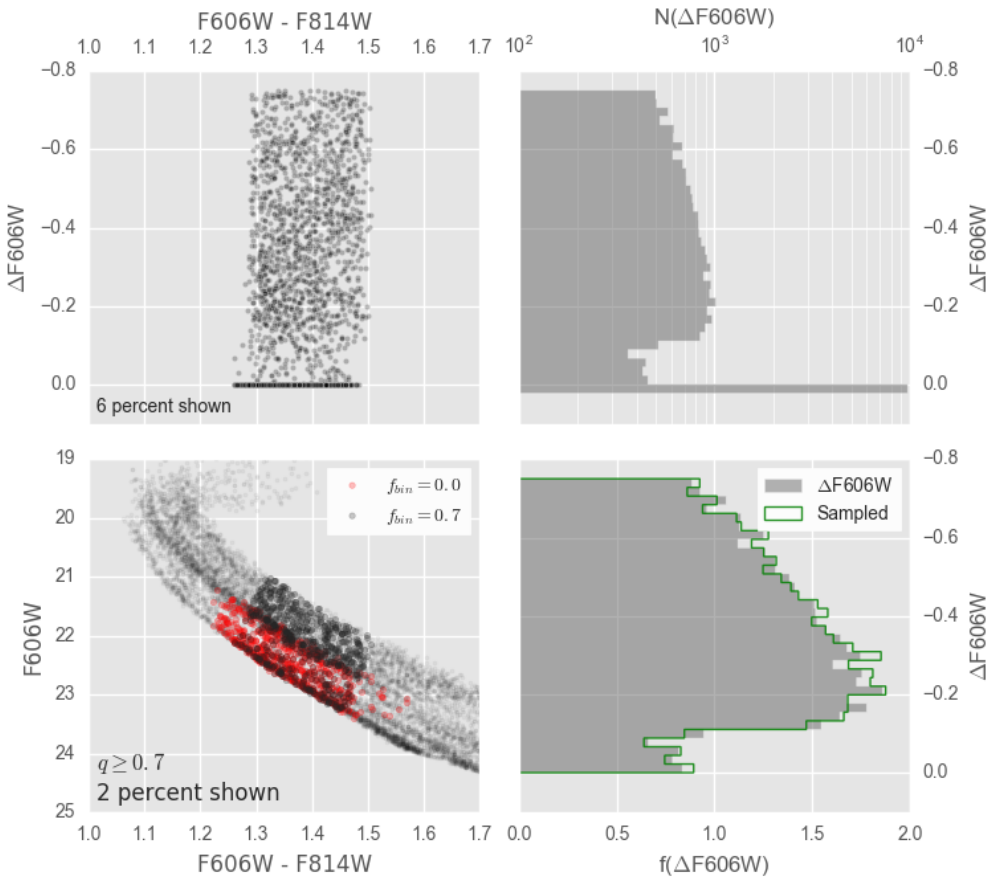

Figure 24. Characterization of the distribution of apparent magnitude perturbation due to unresolved binaries, using the BaSTI suite of models and stellar population tools. Reading clockwise from lower-left: *Lower-left:* synthetic stellar populations in the SWEEPS filter-set. Red points show the simulation without binaries, gray the population with binaries. Faint points show a representative set of the entire simulation in each case, dark points show the objects which fall within the CMD selection region in the presence of unresolved binaries. *Upper-left:* Δm_{bin} due to the presence of unresolved binaries, for objects only within the selection region. *Upper-right:* the distribution of Δm_{bin} (on a log scale), with histogram boundaries at the upper end of each bin. This panel includes objects not assigned a binary companion in the simulation. *Lower-Right:* Normalized distribution of Δm_{bin} for objects assigned a binary companion (gray shading). The green open histogram shows the distribution of draws from a non-parametric resampling of $f(\Delta m_{bin})$. See subsection C.2.

ulation for each iteration, and brings into reach Monte Carlo exploration of the impact of binaries for our purposes here.

BaSTI simulations are run for four choices of the minimum binary initial mass ratio: $q_{min} = (0.0, 0.3, 0.5, 0.7)$. The "bulge" star-formation history (Mollá et al. 2000) within BaSTI is used to populate the sample, with Scaled-to-solar heavy element abundances and the Kroupa et al. (1993) initial mass function. Absolute magnitudes are converted to apparent magnitudes using a fiducial distance and reddening. This allows $f(\Delta m_{bin})$ to be characterized specifically for the population we have selected for proper motion study. For $q_{min} = 0.0$, the distribution $f(\Delta m_{bin})$ turns out to closely resemble $f(\Delta m_{bin}) = 1/\Delta m_{bin}$, while for $q_{min} > 0$ the distribution becomes more complicated and nonparametric resampling is preferred (Figure 24).

In none of the cases ($q_{min} = 0.0, 0.3, 0.5, 0.7$) do we find that the presence of an additional binary population can account for the difference between the observed "metal-rich" and "metal-poor" rotation curves. (Figure 25 shows the cases $q_{min} = 0.0$ and $q_{min} = 0.7$). Only the skewness of the π' distribution ever approximates that of the "metal-poor" population (at $f_{bin} \gtrsim 0.5$), while the rotation curve and π' spread do not overlap for any binary fraction.

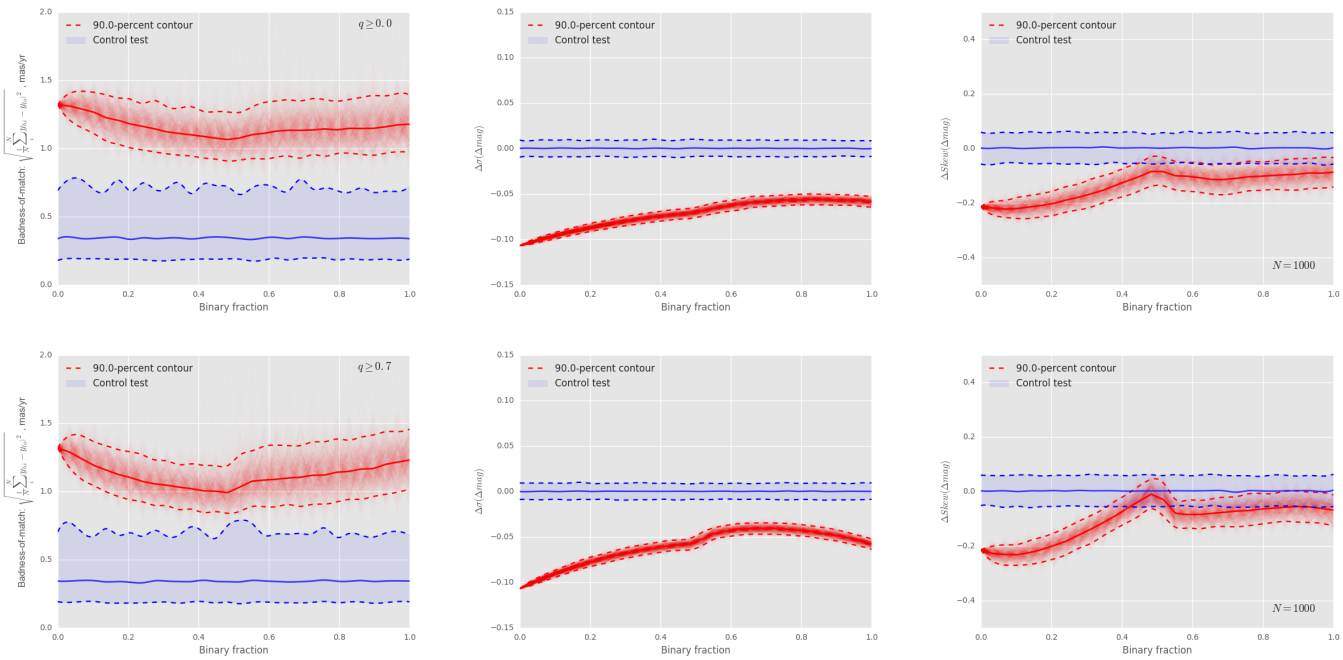

Figure 25. Evaluation of the impact of a difference in binary fraction between "metal-rich" and "metal-poor" populations, in this case for $q \geq 0$ (top row) and $q \geq 0.7$ (bottom row). Panels, colors and symbols as with Figure 21; here, the binary fraction f_{bin} is varied between trials. Similarly to Figure 21, 95% of the samples fall within the dashed contours. See subsection C.2

We therefore conclude that an excess of unresolved binaries in the "metal-poor" over the "metal-rich" population is highly unlikely to be responsible for the difference in rotation curves.

D. THE IMPACT OF DIFFERENTIAL [Fe/H] DISPERSION ON PHOTOMETRIC PARALLAX

Under a model in which the bulge contains at least two metallicity components, with differing [Fe/H] dispersions, the spread in inferred photometric parallax within identified "metal-poor" and "metal-rich" samples will also differ, even if there is no difference in intrinsic distance distribution along the line of sight. Here we examine the likely magnitude of this systematic.

The method is outlined in subsection D.1, with simulated population components described in subsection D.2. In the course of this investigation, it became apparent that the widely-used BaSTI simulation framework truncates samples at [Fe/H] values well within the limits of likely values in the SWEEPS field; the technique used to characterize absolute magnitude spread in the presence of this truncation is described in subsection D.3. Finally, the differential scatter between "metal-rich" and "metal-poor" populations is presented in subsection D.4. (The BaSTI truncation itself is characterized in Appendix E.)

D.1. *General method*

To estimate the differential scatter in photometric parallax produced by differing [Fe/H] dispersions between "metal-rich" and "metal-poor" samples, a synthetic composite stellar population is produced for the SWEEPS field by sampling BaSTI simulations (computed for all three cameras and resampled in the manner of subsection C.2), which include the effects of age, [Fe/H] spread, and unresolved stellar binaries. The synthetic populations are perturbed by photometric uncertainty (in all seven filters), photometric parallax, and reddening, where the width of the distributions in all three quantities can be specified separately for each population.

This produces a SWEEPS CMD and [t], [m] distribution for the synthetic population. Synthetic objects are selected for further "study" in a similar manner as for the real data (e.g. Table 3); in particular, synthetic SWEEPS CMD objects must fall within the selection box in the SWEEPS filters (Figure 2). The surviving synthetic objects are then classified as likely "metal-poor" and "metal-rich" populations in the same manner as for the observed data (using

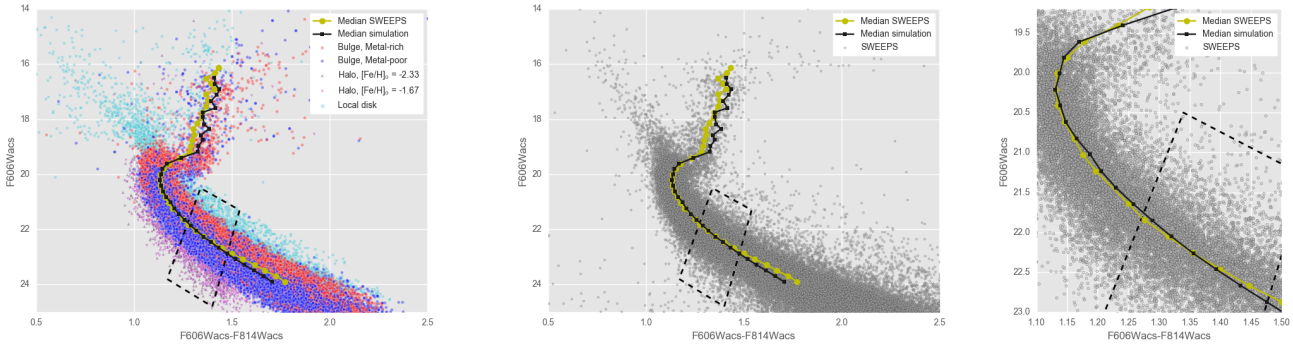

Figure 26. Composite simulated SWEEPS population. *Left:* the synthetic populations. Red and blue circle points show metal-rich and metal-poor Bulge components, respectively, violet and gray triangle points the Halo components, cyan squares the Local Disk populations. *Middle & Right panels:* the observed SWEEPS CMD, with the median simulated (black line and squares in all three panels) and SWEEPS (yellow line and circles in all three panels) populations. See subsection D.2 for details.

the GMM components in [t], [m] that were fitted to the real data), isolating "observed" samples of "metal-rich" and "metal-poor" objects. In this manner, the synthetic samples are isolated in a similar fashion to those drawn from the real data.

Finally, best-fit loci are determined for the model *absolute* magnitudes of the synthetic "metal-rich" and "metal-poor" samples, and the differences ΔM_V from these loci determined for every object in the samples. The model absolute magnitude is used rather than the apparent magnitude because we wish to isolate the impact of metallicity spread on *intrinsic* magnitude scatter - i.e., before distance, reddening, and photometric uncertainty have perturbed the measurements (which impacts the sample selection), but *including* the intrinsic effects of age, [Fe/H], and binarity.

Modeling the selection cuts on the synthetic samples requires simulating the composite stellar population of the SWEEPS field. This field is somewhat complex, consisting of at least three distinct populations (bulge, local disk, halo), each of which could well consist of multiple sub-populations or a continuum.

Full population decomposition presents a formidable challenge (e.g. Gennaro et al. 2015), and is complicated by the difficulty in adequately accounting for extinction across the broad wavelength range of the BTS photometry in the inner Bulge region (e.g. Nataf et al. 2016). To produce a reasonable approximation to the selection effects at work in the SWEEPS field, a multi-component stellar population is instead simulated with parameters drawn from the literature and the [Fe/H] spread estimated in this work (Appendix B). About a dozen synthetic populations with various parameter settings are simulated using BaSTI, and then mixed to produce a synthetic composite population for the SWEEPS field, with mixture parameters tuned by hand to provide an approximate match to the observed SWEEPS CMD and [t], [m] distribution.

D.2. *Synthetic population components*

All population components used the same prescription for binaries, with binary fraction 0.35 and minimum binary mass ratio 0.0. The Initial Mass Function followed the Kroupa et al. (1993) prescription for all components over the BaSTI default mass range ($0.1 \leq M/M_\odot \leq 120$). Convective core overshooting was *not* selected for any model component, and mass-loss parameter $\eta = 0.4$ was used throughout. When not using a pre-determined star formation history supplied by BaSTI, the star-formation histories were specified as a series of single bursts at given ages, with [Fe/H] described as a Gaussian with user-specified centroid and standard deviation. Specific details for various population components follow below.

For the foreground disk, the formation history of Rocha-Pinto et al. (2000) was used (the default "Local Disk" scenario within BaSTI), typically forming $5\% - 10\%$ of the stars in the simulation sets.

Stellar halo components were simulated using the bimodal [Fe/H] distribution reported by An et al. (2013) from SDSS photometry; this model consists of a very metal-poor component centered at [Fe/H] ≈ -2.33 and another slightly less metal-poor component centered at [Fe/H] ≈ -1.67. For a bimodal bulge population following any of the GMM fits to our spectroscopic data, or for the [Fe/H] distribution of Zoccali et al. (2017) near the SWEEPS field, this separate halo component is necessary to populate the regions in [t], [m] space for objects with [Fe/H] $\lesssim -2.0$.

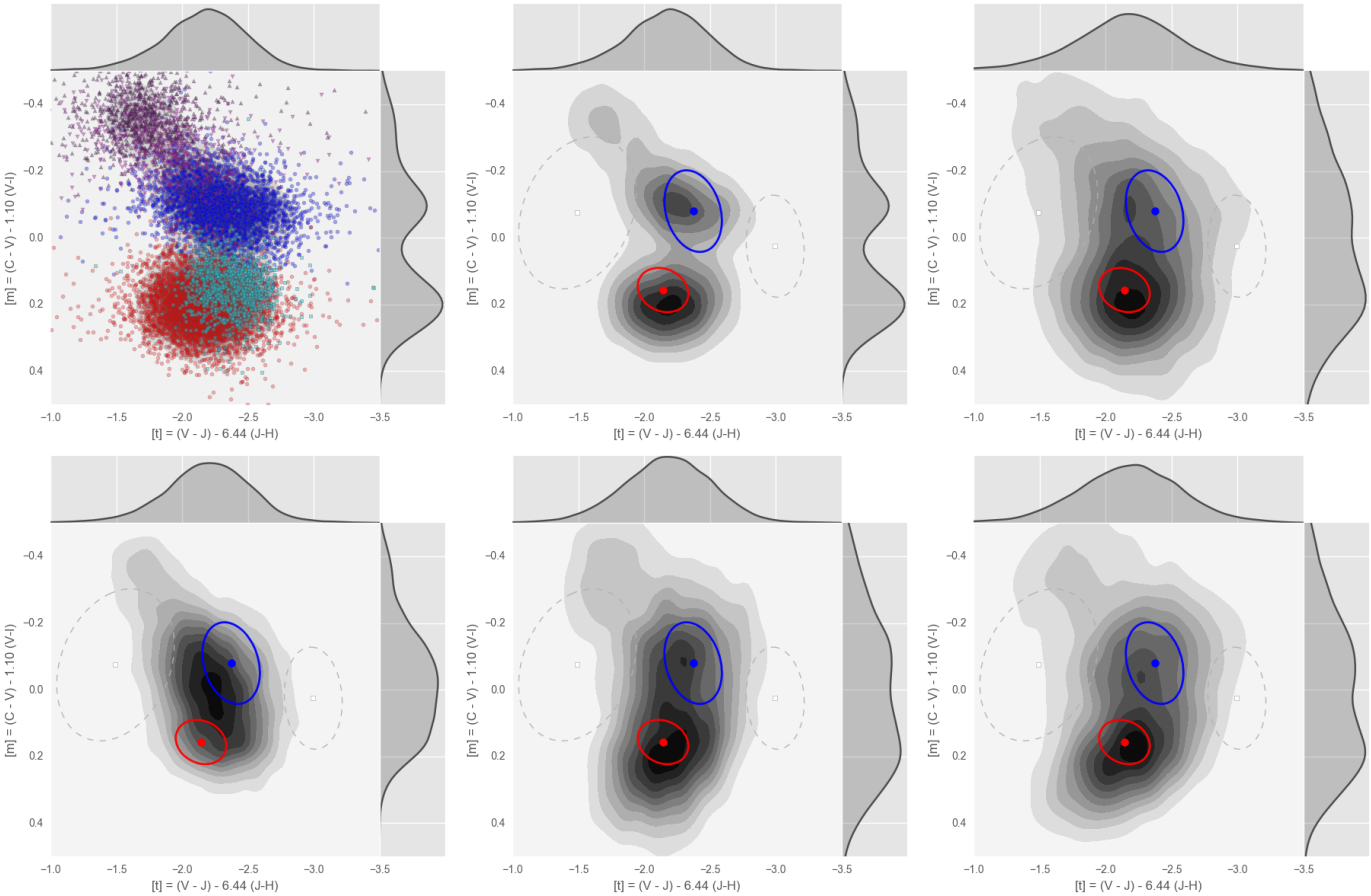

Figure 27. Example synthetic populations used to estimate metallicity effects on sample selection and measured relative photometric parallax distributions; all panels show the [t], [m] distributions of the model populations with marginal distributions of [t] and [m] plotted over the top and right axes, respectively (compare with Figure 3). All but the bottom-left panel show populations with the same intrinsic parameters, modified observationally in different ways. *Top-left:* Example [t], [m]distribution; symbols label components of origin in the same way as in Figure 26. *Top-middle:* KDE representation of the simulation in the top-left panel, with the "metal-rich" and "metal-poor" model components overlaid as ellipses. *Top-right:* population parameters as with the top-middle panel, but with photometric uncertainties in the BTS filters multiplied by a factor two to enhance scatter. *Bottom-left:* bulge components drawn from BaSTI's "bulge" star formation history (Mollá et al. 2000), using one set each with BaSTI's α-enhanced and scaled-to-Solar isochrone-sets. *Bottom-middle:* population parameters as for the top-middle panel, but with [t], [m] each blurred by independent Gaussians, with width parameter $\sigma_{[t]} = 0.15$ and $\sigma_{[m]} = 0.05$. *Bottom-right:* population parameters as per the top-middle panel, but with R_V Normally distributed at $R_V = 2.5 \pm 0.52$ in order to bring the marginal distributions roughly into line with those observed. See subsection D.2 for details.

Bulge components were constructed separately as Normally-distributed [Fe/H] distributions specified through the BaSTI web interface, using the characterization presented in Appendix B, both for the two- and three-component GMM decompositions. For components less metal-rich than $[\mathrm{Fe/H}]_0 < +0.3$, separate runs were simulated using the "Scaled-to-Solar" and "α-enhanced" options within BaSTI in order to allow some exploration of α-enhancement on population spread in the [t], [m] diagram. A variety of age prescriptions were attempted, mostly to improve the match at the bright end of the SWEEPS CMD, by ascribing either a single burst of star formation to each metallicity, or by assigning several bursts to each metallicity (e.g. bursts at 5.0, 6.0 and 7.0 Gy for a component with $[\mathrm{Fe/H}]_0 = -0.42$). We have not yet explored more sophisticated age-metallicity prescriptions through user-defined star formation histories (e.g. Bensby et al. 2017; Haywood et al. 2016).

The more continuous bulge star formation history of Mollá et al. (2000, used as a default in BaSTI) was also tried, for "Scaled-to-Solar," "α-enhanced" isochrones, and for varying admixtures of the two.

We have not yet explored a separate "thick-disk" component in this context. The metal-poor wing of the bulge distribution or the metal-rich wing of the halo component could mimic such a population in the [t], [m] diagram and we do not make the distinction here.

Figures 26 and 27 show examples of the synthetic populations thus produced. None of the population mixtures that we have produced quite reproduces both the observed SWEEPS CMD and the [t], [m] diagram, although in view of both the challenges of extinction characterization and apparent simulation truncations imposed by BaSTI itself (subsection D.3), full reproduction is likely to be difficult. The basic two-component bulge we simulate here produces an [t], [m] distribution that is much more strongly bimodal than that observed (e.g. Figure 3), while the ten-component "Bulge" star-formation history within BaSTI (Mollá et al. 2000) produces an [t], [m] distribution that is too smooth compared to that observed.

Several methods were attempted to bring the simulated [t], [m] distribution into closer agreement with that of the observed data in Figure 3. One simple ansatz is to simply multiply the BTS estimated photometric uncertainties by a factor two before selection and computation of [t], [m] (Figure 27, upper-right panel). Another is to apply Gaussian blurring in [t] and [m] separately (lower-middle panel of Figure 27). Varying R_V with a Gaussian of width $\sigma_{R_V} = 0.52$ does bring the marginal distribution reasonably close to that observed (lower-right panel of Figure 27), although the [t], [m] distribution that results is distorted compared to the observed sample (particularly the "metal-rich" sample), and in addition the required σ_{R_V} is at least a factor ~ 2 larger than that suggested by the SWEEPS color-magnitude diagram (subsection D.5, which also shows the [t], [m]-blurring effect due to R_V variations that are compatible with the SWEEPS data).

For the purposes of estimating the impact of varying [Fe/H] distribution on relative photometric parallax variations, we retain the two-component bulge model with and without BTS uncertainty scaling, for further investigation; the former is consistent with estimated [Fe/H] distributions and estimates of photometric uncertainty, while the latter is the "broadened" option among those tried that closely resembles the observed distribution (Figure 3).

D.3. *Characterizing excess variability in the presence of truncation*

While conducting tests on the simulated datasets, it quickly became apparent that samples generated with the current version of BaSTI[21] show truncation at extremes of both high- and low-metallicity, leading to a hard edge in the CMD of the simulated population that has no counterpart in the reported [Fe/H] distribution. This truncation, characterized in Appendix E, impacts the metal-rich simulated bulge sample more strongly than its metal-poor simulated counterpart and thus could artificially enhance the discrepancy in absolute magnitude breadth between the metal-rich and metal-poor simulated components.

This hidden systematic complicates efforts to characterize the excess magnitude scatter due to differing [Fe/H] distributions, with much of the most metal-rich end of the metal-rich simulated sample assigned apparently incorrect magnitudes (absolute and apparent). We therefore adopt a restricted-sample estimate of the magnitude scatter, by sampling only the fainter side of the magnitude distribution for both samples in the comparison. Specifically, we use the quantity $\sigma_{\rm hi}$ defined by[22]

$$\sigma_{\rm hi}^2 \equiv \frac{1}{N(m \geq \overline{m})} \sum_{m \geq \overline{m}} (m_i - \overline{m})^2 \tag{D5}$$

where, for the special case of a large, strictly symmetric distribution, $\sigma_{\rm hi}$ closely approximates the sample standard deviation. A practical challenge is to identify the median magnitude $\overline{m}$ from a truncated asymmetric distribution. For these simulations, $\overline{m}$ is estimated by discarding the most negative Δm samples (thus discarding objects near and outside the truncation limits) and fitting a Gaussian function to the *histogram* of Δm values. This fit is only used to estimate $\overline{m}$, which thus allows $\sigma_{\rm hi}$ to be estimated following Equation D5. This then allows the restricted-sample scatter $\sigma_{\rm hi}$ to be estimated for the metal-poor and metal-rich samples separately, and the excess difference characterized as the quadrature difference between the two.

The final step is then to convert the excess scatter $\sigma_{\rm hi}$ estimated from the simulated population components, to the additional flux scatter s felt by the metal-poor sample compared to the metal-rich sample. To enable this conversion, the relationship between restricted-sample scatter $\sigma_{\rm hi}$ and the flux perturbation scale s that generated it, was deter-

[21] BaSTI version 5.0.1.

[22] (Equation D5 uses $1/N$ instead of $1/(N-1)$ because the median $\overline{m}$ is determined from a fit to a larger sample than the set over which σ_{hi} is evaluated. In practice, with $N(m \geq \overline{m})$ always larger than a few hundred objects, the distinction is unimportant.)

Table 10. Characterization of the additional absolute magnitude scatter due to [Fe/H] for simulated Metal-rich and Metal-poor populations. The quadrature difference between the two samples is reported in the final line. $\sigma_{\rm hi}$ reports an estimate of the asymmetrically-sampled absolute magnitude scatter (subsection D.3), while s reports the scatter in the flux perturbation due to [Fe/H] spread. The first column-pair shows results for the simulated populations and estimated uncertainties; the final column-pair shows results for [t], [m] distribution broadened to more accurately match the observed distribution. See subsection D.4.

Component	$\sigma_{\rm hi}$	s	$\sigma_{\rm hi}$(broadened)	s(broadened)
Metal-poor	0.137	0.112	0.153	0.124
Metal-rich	0.103	0.087	0.119	0.099
Excess	0.090	0.071	0.097	0.075

Table 9. Polynomial coefficients relating the flux spread s (subsection C.1) to apparent magnitude scatter $\sigma_{\rm hi}$ (Equation D5), over the domain ($0.01 \leq \sigma_{\rm hi} \leq 1.0$). The forms used are: $\log_{10}(\sigma_{\rm hi}) = \sum b_i \log_{10}(s)^i$ and $\log_{10}(s) = \sum a_i \log_{10}(\sigma_{\rm hi})^i$. See Figure 28 and subsection D.3.

Coeff	$i=7$	6	5	4	3	2	1	0
a_i	0.2621	1.9750	6.0299	9.5353	8.1928	3.4773	1.2929	-0.2817
b_i	0.6190	4.3495	11.7411	14.7695	7.7084	0.0234	0.1323	0.1298

mined by simulation. Synthetic populations with perturbation flux distribution were produced following Equation C4, subject to the same censoring for negative flux as before (subsection C.1). The apparent magnitude scatter $\sigma_{\rm hi}$ was then found for each synthetic population as described above (and as performed for the simulated BaSTI datasets). Finally, the relationship between $\sigma_{\rm hi}$ and s was characterized by fitting a 7th-order polynomial in both directions. Table 9 and Figure 28 show this characterization. This allows us to relate the restricted-sample scatter found from BaSTI simulations, back to the flux ratio perturbation scale s, and finally to compare the scale of the perturbation suggested by differing [Fe/H] distributions to the additional scale of flux perturbations s that our observational data would require if the "metal-poor" sample really were a blurred version of the "metal-rich" sample.

D.4. *Differential photometric parallax dispersion due to differential* [Fe/H] *dispersion*

We are finally in a position to estimate the additional scatter in absolute magnitude due to differential metallicity scatter. Figure 29 shows the results of applying the selection criteria to the simulation including the two-component bulge model, a two-component halo, and local disk component.

Figure 30 illustrates the characterization of absolute magnitude scatter $\sigma_{\rm hi}$, while Table 10 shows the evaluation of the excess flux scatter s for "metal-poor" compared to "metal-rich" samples. Two simulated populations were evaluated in this manner; one including the two-component bulge model; the other with the BTS uncertainties multiplied by a factor 2 before selection to broaden the distribution in [t], [m]. In both cases, the excess fractional flux scatter s is less than 0.1; we find $s \approx 0.09$ for the two-component bulge model, while $s \approx 0.07$ for the enhanced-uncertainty version of this model.

We contacted the authors of the BaSTI web tools regarding its internal truncation (detailed in Appendix E). In response, Santi Cassisi (2017, private communication) kindly added a high-metallicity point to BaSTI's internal metallicity grid (since in BaSTI version 5.0.1, the metallicity range covered by the simulator is more restrictive than

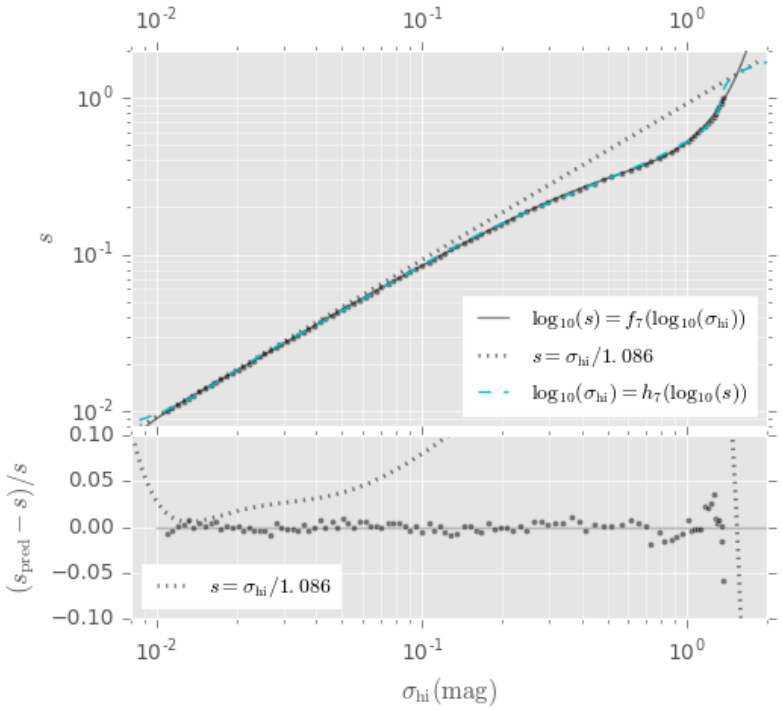

Figure 28. Charting the relationship between the flux standard deviation s (subsection C.1) and the apparent magnitude scatter $\sigma_{\rm hi}$ for truncated samples (Equation D5). Simulated perturbed populations are generated following Equation C4 and the absolute magnitude distribution of the resulting sample is characterized by $\sigma_{\rm hi}$. Standard uncertainty propagation predicts $s \approx \sigma/1.086$ (with σ the apparent magnitude standard deviation); in practice, we fit functional forms to transform between s and $\sigma_{\rm hi}$. The top panel shows s and $\sigma_{\rm hi}$ along with the functional forms in both directions (seventh-order polynomials in $\log_{10}$-space). The bottom panel shows fractional residuals when $\sigma_{\rm hi}$ is used to predict s (residuals in the reverse direction are not shown); the polynomial approximation f_7 is accurate to better than 2% over most of the range of interest. See subsection D.3 and Table 9.

that covered by the isochrone set), and re-computed sets of synthetic populations using the updated version of the simulator.[23] Visual inspection of the [t], [m] distribution and the SWEEPS CMD drawn from the Cassisi simulations show similar behavior to those from v5.0.1, except without the sharp edges truncating the metal-rich end of the synthetic population.

In this paper we retain the statistics derived using BaSTI v5.0.1 since that is the version currently available to the community. However, the comparison with the Cassisi version is instructive. Application of the half-sample techniques of subsection D.3 to both the Cassisi and v5.0.1 simulations yielded highly similar results ($\sigma_{\rm hi}$ differing by $< 4\%$), as might be expected since this measure uses the side of the ΔM distibution far from the truncation limit. The Cassisi simulations also allow a direct estimate of the accuracy of the one-sided measure adopted in subsection D.3, by comparing $\sigma_{\rm hi}$ to the ΔM standard deviation of the objects in the dominant component of the Cassisi simulation (see Figure 29 for the dominant and "background" components for metal-rich and metal-poor simulated populations). In the Cassisi simulations, the ΔM standard deviation is roughly 20% *smaller* than the estimate $\sigma_{\rm hi}$, suggesting our estimates of the excess photometric scatter in Table 10 may be over-estimates.

We therefore find that the combination of differing metallicity spreads between "metal-poor" and "metal-rich" samples, with differing selection effects in both the [t], [m] distribution and SWEEPS CMD, together contribute differential flux scatter that is not larger than $\sigma_{\rm hi} \approx 0.1$ magnitudes, or additional flux standard deviation $s \approx 0.08$. This additional scatter is a factor 3 too small to bring the observed "metal-poor" and "metal-rich" proper motion-based rotation

[23] We refer to these new simulations as the "Cassisi" simulations, and the simulations ran using the current publicly-available BaSTI suite as "v5.0.1"

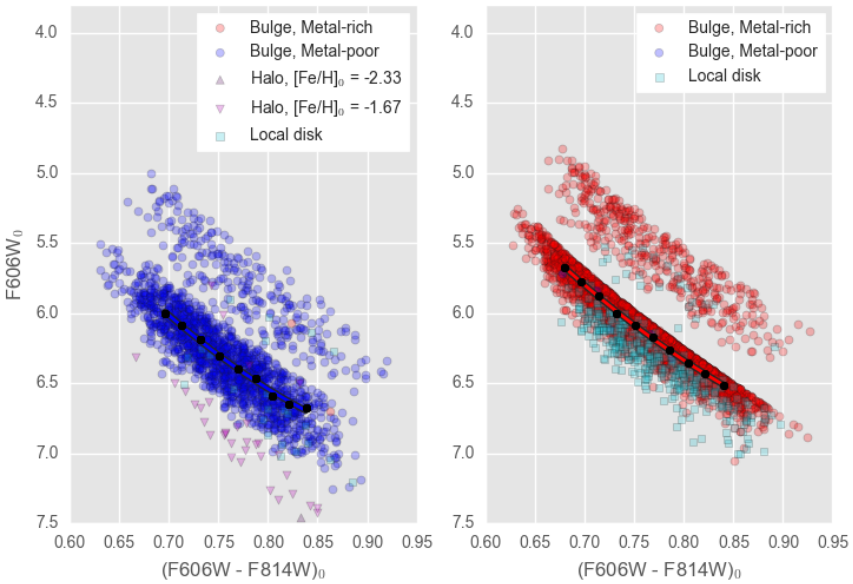

Figure 29. Estimating the ridgelines for simulated objects that would be selected in the "metal-poor" (left panel) or "metal-rich" (right panel) samples. In each case absolute magnitudes are plotted in the SWEEPS filters. The component of origin for each simulated object surviving selection criteria, is indicated by color and plotting symbol. See subsection D.4.

curves into agreement by itself (Figure 21), and we conclude that the apparent difference in proper motion rotation curves between the two samples is *not* an artefact of differences in the underlying [Fe/H] distribution.

As a second check, we can compare the [Fe/H] distribution of the objects classified as "metal-poor" and "metal-rich" with the simulated [Fe/H] values for the relevant Bulge model components. We find that indeed the misclassification rate in this synthetic population-based simulation appears to be low (Figure 31). Possible contaimination is explored further in a purely empirical manner in Appendix F.

D.5. *The impact of R_V variations*

The framework of this Appendix also allows us to investigate the impact of R_V variations on [t], [m]-based determinations. The extinction-free indices [t], [m] assume a particular extinction prescription (Cardelli et al. 1989 using R_V=2.5). While [t], [m] are therefore insensitive to variations in $E(B-V)$ for a particular value of R_V, variations in R_V could impact the distribution of points in the [t], [m] diagram, by altering the relationships between apparent magnitudes in the BTS filters from those assumed when computing [t], [m].

We appeal to the SWEEPS color-magnitude diagram to estimate limits on the magnitude of R_V variations in this field. Assuming the distance distribution due to the physical depth of the bulge can in this field be characterized by a Gaussian with width parameter σ_d kpc, the observed apparent magnitude scatter of Red Clump Giants (RCG) in this field then sets an upper limit on R_V variations for assumed $E(B-V)$. In the SWEEPS dataset, the observed F814W dispersion of the RCG is $\sigma(F814W) \approx 0.17$ magnitudes (Cl08).

For this subsection we adopt $E(B-V)$=0.5 (Ca14) as a representative value (the implied R_V variations would become smaller for larger $E(B-V)$). The extreme case of distance dispersion, $\sigma_d = 0$, then admits R_V variation of $\sigma_{R_V} \approx 0.45$. However, the bulge has nonzero depth along the line of sight; picking a representative distance distribution of $\sigma_d \approx 0.5$ kpc, suggests variation closer to $\sigma_{R_V} \approx 0.25$ is more likely. Both estimates for σ_{R_V} are conservative *upper* limits, since they ascribe none of the observed RCG apparent magnitude dispersion to photometric uncertainty, luminosity variations within the RCG sample, or $E(B-V)$ variation.

To estimate the impact of R_V variation on the [t], [m] distribution (and thus sample selection and cross-contamination), a synthetic population was constructed using BaSTI population components tuned to the estimated metallicity distribution for this field. Full details of this procedure, which was implemented to explore metallicity-dependent selection and characterization systematics (subsection 5.1), can be found in Appendix D.

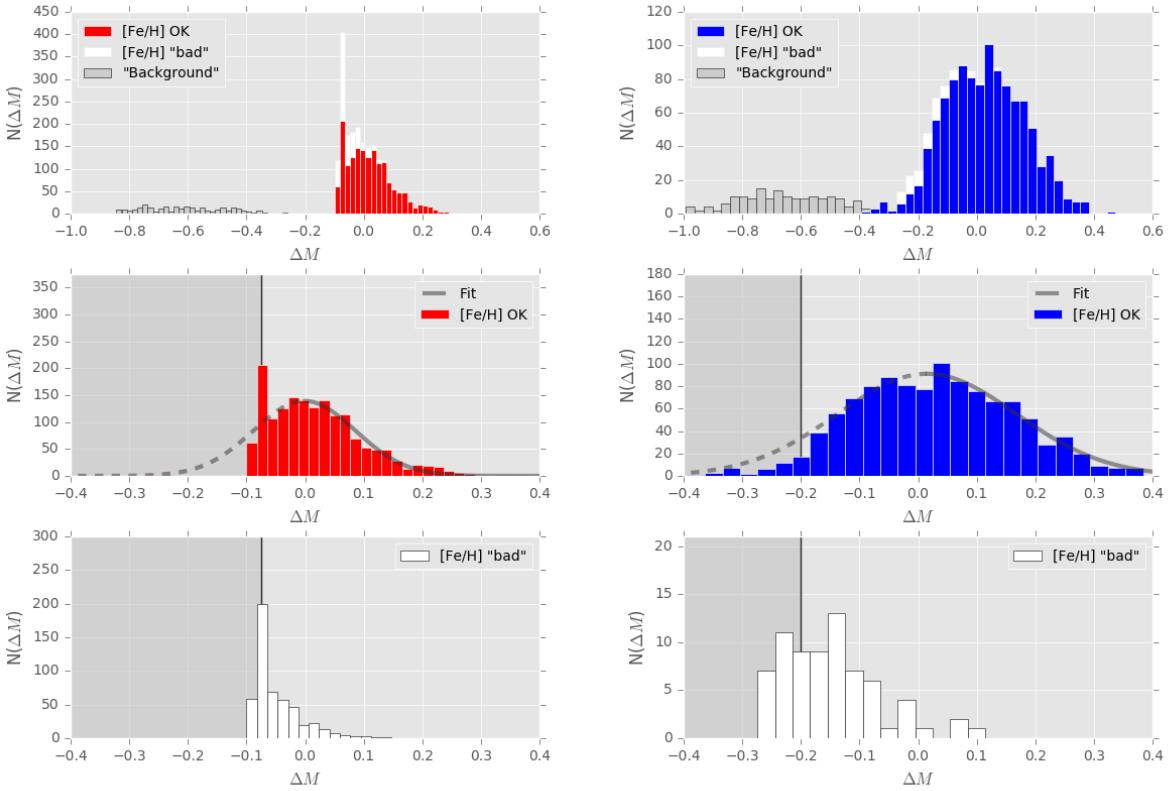

Figure 30. Characterizing the magnitude scatter $\sigma_{\rm hi}$ (Equation D5) for simulated populations in the presence of truncation. The left column shows the simulated metal-rich population, the right column the simulated metal-poor. White-shaded bars in each figure show objects with [Fe/H] outside the adopted BaSTI metallicity range (using scaled-to-Solar isochrones for the metal-rich column, α-enhanced for metal-poor). Reading top-bottom, rows show: the full distribution (top), objects with simulated [Fe/H] within the nominal ranges (middle), and those outside the nominal ranges (bottom). The gray regions in the middle and bottom rows (delimited by the solid vertical line) show regions of ΔM excluded from the Gaussian fits to the distributions (smooth lines). The fitted median of ΔM is marked by a transition from solid to broken line in the curves. Before characterization, each simulated sample is classified into a dominant and secondary component; the secondary component, mostly made up of unresolved binaries and labeled "Background" in the panels here, is excluded from further consideration. Note that (i). *both* the metal-rich and metal-poor samples include objects with reported [Fe/H] above the adopted upper limit; (ii). the truncation appears to impact objects even with [Fe/H] nominally within the adopted [Fe/H] limits, particularly for the metal-rich simulated population, and (iii). the strong truncation in the metal-rich sample leads to a large gap between the dominant and secondary component. See subsection D.4.

Figure 32 shows the comparison of a simulated [t], [m] population, with and without R_V variations at the $\sigma_{R_V} = 0.25$ level admitted by the SWEEPS dataset. For each relevant WFC3 filter, the scale factors $A_X/E(B-V)$ were estimated by linear interpolation in R_V using information shown in Table 4. The simulated magnitudes were thus perturbed into "observed" magnitudes using different R_V values for each star, but the [t], [m] were computed using the α, β values appropriate for R_V=2.5. This then mimics the use of a single R_V value to compute [t], [m] for a population that in reality shows R_V variations.

Comparing the synthetic [t], [m] distributions with and without R_V variations (Figure 32), it seems unlikely that R_V variations at the level admitted by the SWEEPS color magnitude diagram can contribute a strong effect on GMM fitting or sample selection in [t], [m]; the impact of R_V variations is simply too small. We therefore proceed under the assumption that indeed $R_V \approx 2.5$ for all objects in the SWEEPS field of view.

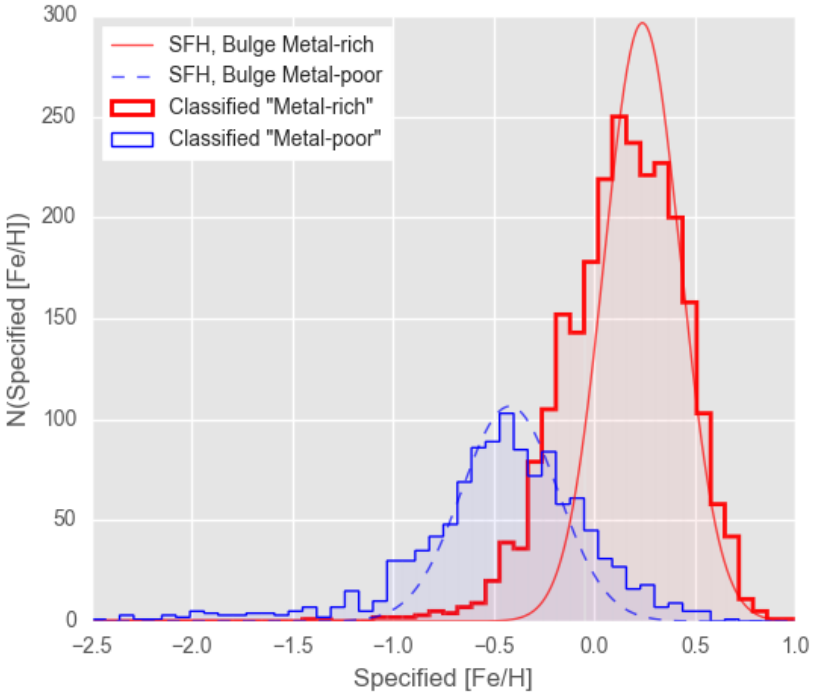

Figure 31. Comparison of recovered and input samples for the five-component BaSTI-based synthetic composite SWEEPS field population (e.g. Figure 29). The histograms show the objects classified with the "metal-poor" (blue, thin stepped line) and "metal-rich" (red, thick stepped line) samples. The smooth Gaussian [Fe/H] distributions that were specified for the two Bulge components are overlaid; the Metal-poor (blue-dashed curve) and the Metal-rich (red solid curve) components. The [Fe/H] values are those reported in the BaSTI output tables (see discussion in Appendix E). See Appendix D.

E. TESTING THE BEHAVIOR OF THE BaSTI STELLAR EVOLUTIONARY MODELS

Because stars in the SWEEPS field likely span a very wide [Fe/H] range, including possibly objects outside the ranges traced by the BaSTI evolutionary models, we test the behavior of the BaSTI synthetic population framework when objects with very low or very high metallicities are simulated.

We find that BaSTI v5.0.1 appears to be imposing an internal truncation on the simulated populations, probably on [Fe/H] or on an internal variable that correlates with metallicity (for clarity, we refer to internal limits as [Fe/H] limits throughout this section). This in turn leads to a discrepancy between the requested and simulated population, and between the reported [Fe/H] values in the simulated output and the resulting population. Since BaSTI is used very widely in studies of resolved stellar populations (with over 600 refereed citations), we report here our investigation into this truncation.[24]

A variety of synthetic populations were simulated using BaSTI's "user-specified SFH" option. This allows the user to build a population from a series of bursts of star formation, with the mean and standard deviation [Fe/H] specified for each population, as well as the number of years elapsed since the burst took place. In addition to the components that might make up the scene in the SWEEPS field of view (e.g. subsection D.2), we simulated a number of "test-pattern" populations, with components regularly (or nearly-regularly) spaced in [Fe/H].

The behavior of the color-magnitude diagram in the SWEEPS filters is then examined for consistency with the specified [Fe/H] distribution and also the [Fe/H] values reported in the simulated population. For regions in the CMD approximately near the selection region used in this communication, the absolute magnitude difference ΔM is

[24] The analysis and figures in Appendix E can be reproduced using the notebook `2017-09-08_quicklookBaSTi_truncation.ipynb` in the repository at `https://github.com/willclarkson/bastiTest`. This repository includes the full set of simulations and input parameters, as well as relevant methods used to generate the figures in this section.

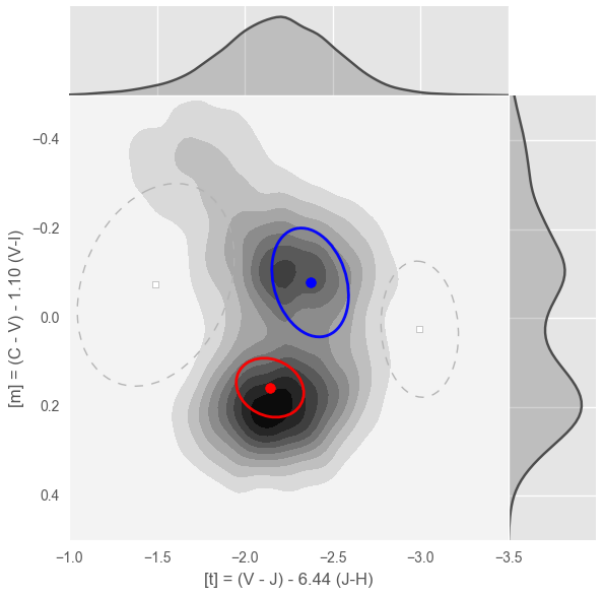

Figure 32. Estimating the impact of R_V variations in the [t], [m] diagram. The middle-top pattern of Figure 27 shows a simulated [t], [m] distribution using estimated photometric uncertainties and [Fe/H] distribution, and with $R_V = 2.5$ for all objects. This figure shows the same simulation but this time varying R_V by $\sigma_{R_V} = 0.25$. The 1σ ellipses from the GMM decomposition of the observed data are shown to allow rough comparison between this simulation and the true dataset, and the top and side panels show the marginal distributions of [t] and [m], respectively. See subsection D.5.

computed from a fitted median sequence (in much the same manner as is done for the observed population), and the distribution of ΔM examined for hard edges that are not present in the requested [Fe/H] distribution.

The BaSTI documentation was used to estimate median [Fe/H] values near the limits of its metallicity range.[25] Specifically, we assumed the appropriate [Fe/H] limits to be $(-2.27 \leq [\mathrm{Fe/H}] \leq +0.40)$ for scaled-to-Solar models, and $(-2.62 \leq [\mathrm{Fe/H}] \leq +0.05)$ for α-enhanced models. Results for a representative set of test-cases are reported below, which suggest the following effects:

- Any bursts of star formation with specified median [Fe/H] outside internal limits, are clipped to these limits before generation of the stellar population (subsection E.1);
- If the specified [Fe/H] distribution leads to individual objects with [Fe/H] outside the limits, the absolute magnitudes of these objects are truncated internally, but the reported [Fe/H] values appear to be unaffected, leading to a discrepancy between reported and applied [Fe/H] values (subsection E.2);
- The truncation behavior appears more complex than a simple clipping or substitution; discrepant objects can appear quite deep into the main body of the selected population, and the effective [Fe/H] limits might differ from those suggested by the documentation (subsection E.3).

E.1. *BaSTI selection applied to median populations*

To investigate whether BaSTI is applying the truncation to the median population in a requested sample, test-populations were simulated for bursts of star formation of equal magnitude but with very narrow [Fe/H] distributions. Figure 33 shows an example for a scaled-to-Solar set of isochrones, with $[\mathrm{Fe/H}] = \{-3.0, -2.5, -2.0, -1.5, -1.0, -0.5, +0.0, +0,4, +0.5\}$, all with spread $\sigma_{[\mathrm{Fe/H}]} = 0.0001$ dex to isolate selection effects applied to the mean populations in each case. The two most metal-poor and the single most metal-rich populations are found to be forced away from their specified values, probably to some internal limit. Reading off the figure, the most metal-poor populations seem to be brought up [Fe/H] ≈ -2.3 with the most metal-rich brought down to

[25] See http://basti.oa-teramo.inaf.it/main_mod.php and links therein.

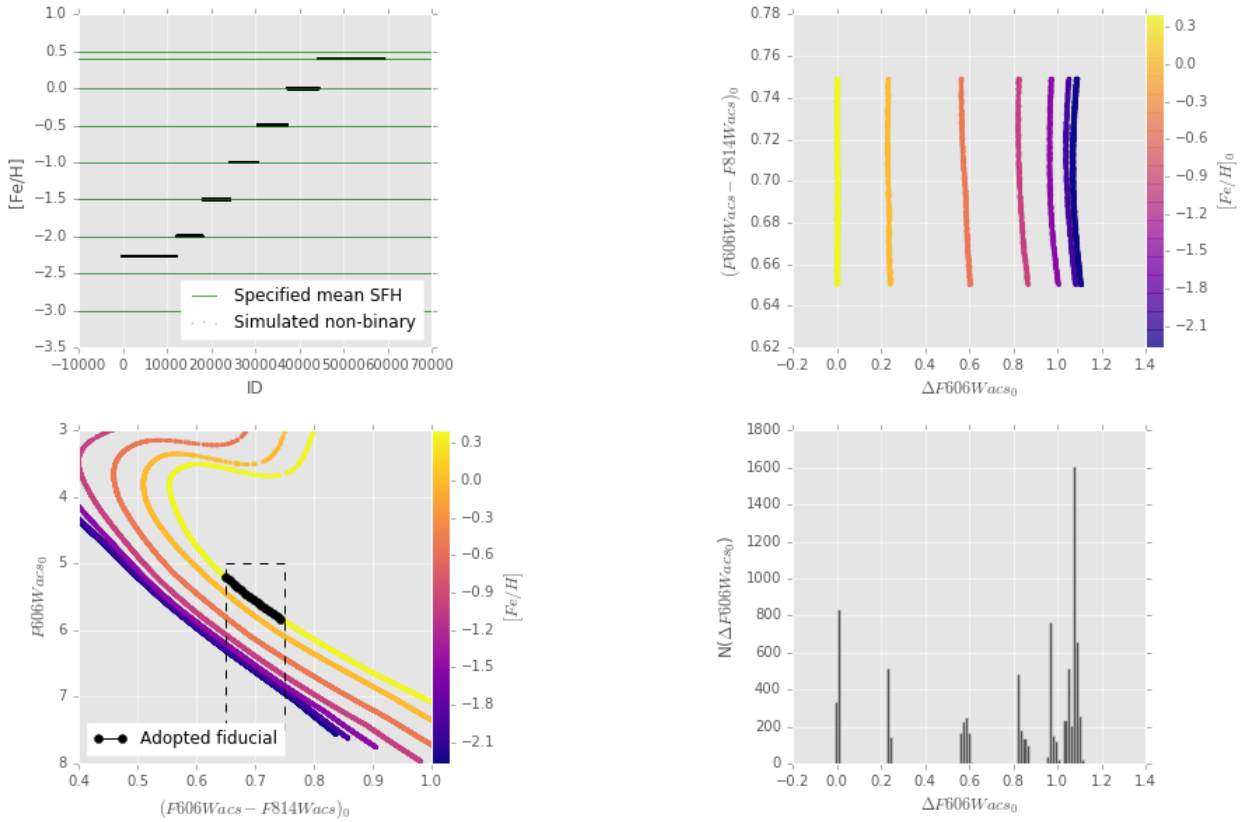

Figure 33. Testing the relationship between specified and simulated metallicities when bursts of star formation with a very wide range of median [Fe/H] values is requested with the BaSTI interface. *Left top:* specified and simulated [Fe/H] median values. The green horizontal lines show the median [Fe/H] values for the bursts of star formation, with the gray points indicating [Fe/H] values reported in the output simulation. In this example, specified bursts are ordered from bottom to top and left to right in the simulated objects. *Left bottom:* absolute magnitude CMD in the SWEEPS filters of the resulting population, color coded by reported [Fe/H]. The black dots and line refer to the fitted fiducial in the selection region and a polynomial fit to the fiducial, respectively. *Right top:* absolute magnitude offsets ΔM from the adopted fiducial, ordered by SWEEPS color, with symbols color-coded by [Fe/H] reported in the simulated population. *Right bottom:* histogram of ΔM. Here the specified median [Fe/H] values were $\{-3.0, -2.5, -2.0, -1.5, -1.0, -0.5, +0.0, +0, 4, +0.5\}$, all with specified spread $\sigma_{[Fe/H]} = 0.0001$ dex. Populations with [Fe/H] $\lesssim -2.3$ or [Fe/H] $\gtrsim +0.4$ seem to have been wrapped by BaSTI to the metallicity limits. See subsection E.1.

[Fe/H] $\approx +0.40$. These values are entirely consistent with the [Fe/H] limits suggested by the BaSTI documentation referenced earlier.

This suggests that BaSTI enforces [Fe/H] limits on the median populations requested in a simulation.

E.2. *BaSTI truncation near the* [Fe/H] *limits*

To investigate whether BaSTI applies a truncation to [Fe/H] values that are carried outside internal [Fe/H] limits due to the specified population spread, test-populations were simulated including a single population well away from the limits, and one component each just inside the two limits. Components were specified with [Fe/H] $= \{-2.5, -1.2, +0.05\}$, all with specified spread $\sigma_{[Fe/H]} = 0.1$ dex, to ensure that the two components near the [Fe/H] limits each include substantial numbers of objects outside these limits, while the middle population has very few such objects.

Figure 34 shows the resulting simulation. Curiously, although the [Fe/H] values reported in the simulated populations show no truncation, the CMD and the simulated absolute magnitudes quite clearly do show truncation, with a hard edge at both the upper and lower [Fe/H] extrema.

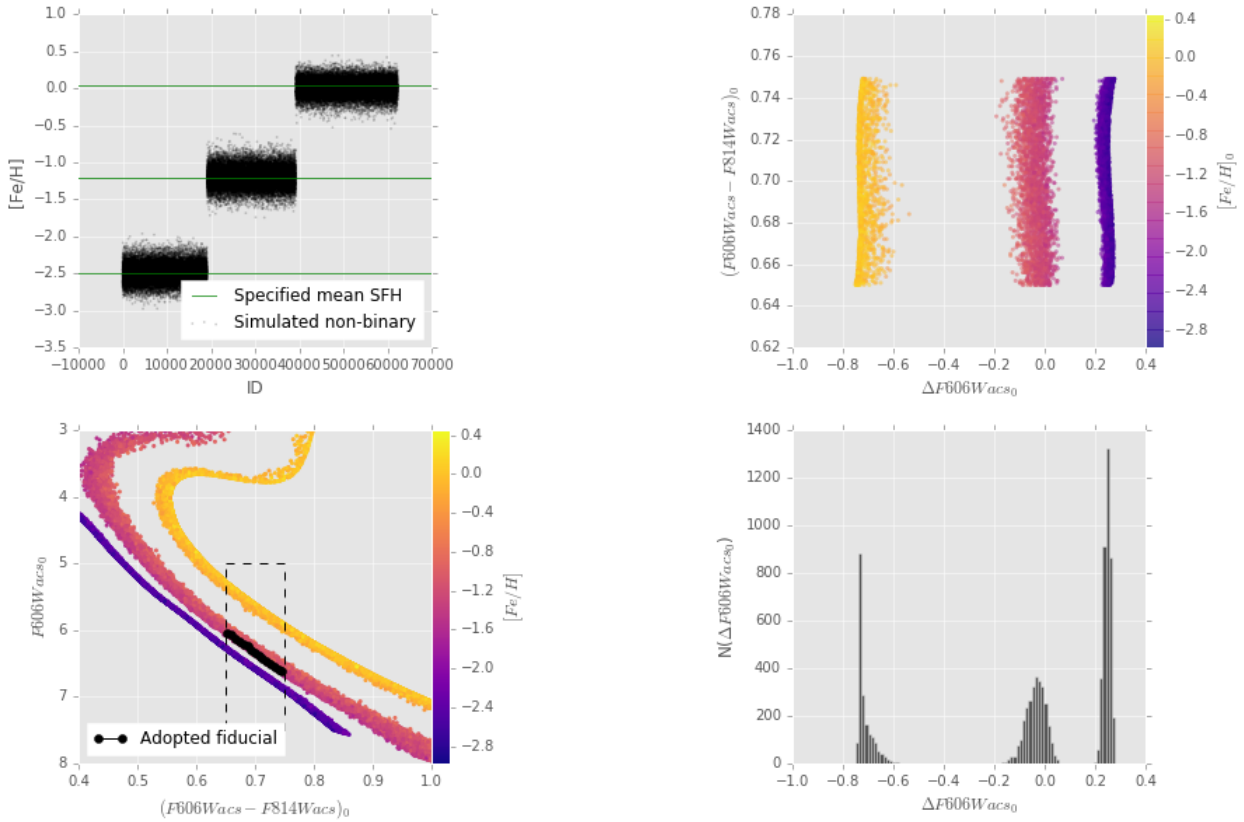

Figure 34. Testing the behavior of BaSTI simulations for populations with [Fe/H] close to the internal boundaries. *Left column:* panels and symbols as Figure 33, with specified bursts ordered bottom-top and their simulated populations ordered left-right. Here a three-component α-enhanced population is simulated, with [Fe/H] $= \{-2.5, -1.2, +0.05\}$, all with specified spread $\sigma_{[\mathrm{Fe/H}]} = 0.1$ dex. The metal-poor and metal-rich populations show sharp cut-offs in both the CMD and the ΔM distribution, which are not present in either the central population (well away from the [Fe/H] limits), nor are the cutoffs present in the reported [Fe/H] distributions of the metal-poor and metal-rich populations. (Curvature in the metal-poor hard-edge is likely due to differences in the shape of the median-population for [Fe/H] $= -2.5$ and that for [Fe/H] $= -1.2$.) The simulated magnitudes of the resulting populations show hard edges at the metal-rich and metal-poor ends, suggesting truncation in the delivered populations. Curiously, however, there is no such truncation in the corresponding *reported* [Fe/H] values. This suggests that a truncation is being applied *after* the assignment of [Fe/H] values to simulated objects. See subsection E.2.

We therefore find that BaSTI does not truncate [Fe/H] values at the stage of assignment to simulated objects, and these non-truncated [Fe/H] values are carried through to the output simulated population. However, a truncation *is* applied at some stage before the absolute magnitudes are included in the simulated population. This results both in a hard edge to the distribution of simulated absolute magnitudes, and also a discrepancy between the reported [Fe/H] values and the absolute magnitudes, in the simulation output.

E.3. *BaSTI truncation near the metal-rich limit*

To chart the behavior of the truncation near the [Fe/H] limits in more detail, we simulated a single test population near the metal-rich limit. Figure 35 shows the result for a scaled-to-Solar component with [Fe/H] $= +0.24$ and scatter $\sigma_{[\mathrm{Fe/H}]} = 0.19$. In this case, the truncation appears to be quite dramatic, with a narrow, highly over-represented component in the ΔM distribution.

However, the behaviour of the simulator near an [Fe/H] limit is not as straightforward as a simple substitution of the [Fe/H] limit for all objects beyond it. Figure 30 shows a simulated metal-rich population partitioned by [Fe/H], which allows us to distinguish objects that were assigned [Fe/H] values above the metal-rich limit (and thus would be assumed to be truncated). Objects with outlier [Fe/H] values do *not* only appear at the location where absolute

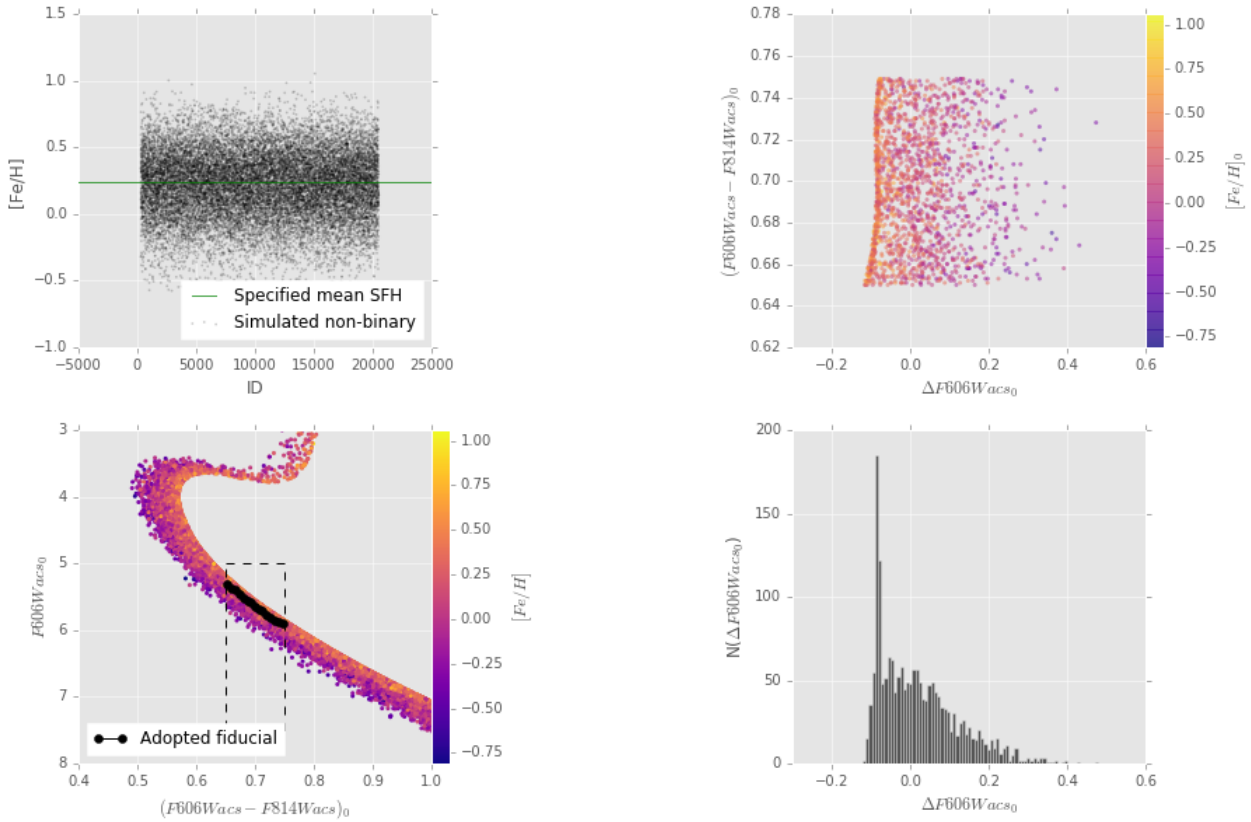

Figure 35. Charting detailed behavior of BaSTI truncation near the metal-rich limit. Panels and symbols are as in Figure 34; here a single scaled-to-Solar component is simulated with [Fe/H] = +0.24 and scatter $\sigma_{[Fe/H]} = 0.19$. A strong pile-up is observed at the bright end of the ΔM distribution (curvature in this component is likely due to systematics in the determination of the fiducial ridgeline, which was determined from the simulated CMD, as would be the case for observed populations, rather than specified using an isochrone). Again, while a strong truncation is observed in the simulated absolute magnitudes, no such hard edge is present in the reported [Fe/H] values. See subsection E.3 and Figure 30.

magnitudes pile up; a substantial fraction show magnitudes deeper into the main population (see the bottom-left panel of Figure 30).

That the pile-up implying truncation is also observed at the metal-rich edge of the population with simulated metallicities *within* the limits according to the BaSTI documentation, suggests that the *effective* metallicity limits may differ from those documented; see the middle-left panel of Figure 30. (We have not yet dissected this simulated population by binarity, which might offer another avenue for objects to wander into truncation territory.)

We therefore find that the internal truncation applied by BaSTI is not limited to a simple pegging of values to an internal boundary. The behavior probably necessitates some sort of selection on ΔM to produce a cleaner unaffected sample. We adopt one such approach in subsection D.3.

F. CROSS-CONTAMINATION IN THE [t], [m] DIAGRAM

We consider here the mixing of the "metal-rich" and "metal-poor" samples (and thus rotation curves) due to cross-contamination in the [t], [m] space from which the two samples were drawn (subsection 5.2).

While the formal membership probability threshold $w_{ik} \geq 0.7$ was chosen to be somewhat conservative, some amount of sample contamination in [t], [m] is highly likely. Since the ([t], [m]) each represent flux ratios constructed from photometry in three filters, it is likely that objects best characterized at one side of the abundance range for the bulge, might be classified to an object in the other due to photometric uncertainty. In principle, a nearly-flat rotation curve for one sample could be polluted by samples from another sample with a large-amplitude rotation curve, and vice

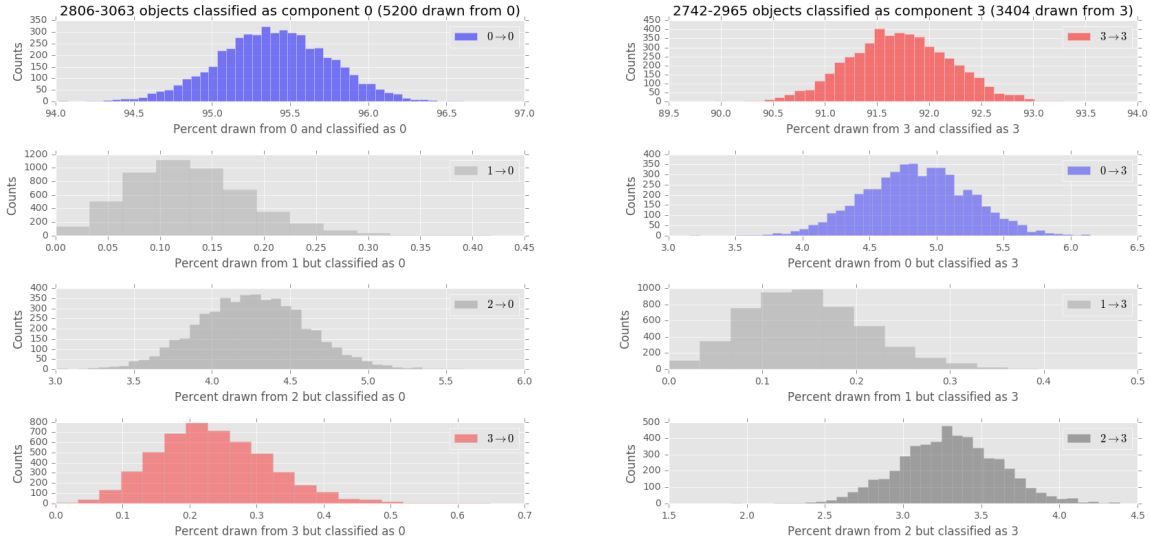

Figure 36. Simple Monte Carlo test for cross-contamination of the "metal-rich" and "metal-poor" samples in ([t], [m]) space. Objects are simulated from the best-fit 4-component GMM in ([t], [m]) space (whose parameters are given in Table 5), perturbed by measurement uncertainty, and re-characterized using another 4-component GMM. The model component assigned to each object in the characterization is then compared to the component from which the object was drawn. The *left column* shows the distribution of origin components for objects classified as "metal-poor" (top left, blue), the *right column* shows the origin components for objects classified as "metal-rich" (top right, red). In each column the top panel shows the distributions of objects classified correctly, the others show the distributions of objects classified with a different (indicated) component. In both columns, component "0" (blue) is the "metal-poor" component, component "3" (red) is the "metal-rich" component, and components "1" & "2" (gray) are the remaining components, used to characterize the background in ([t], [m]). See Appendix F.

versa, sufficiently to weaken the trends in the high-amplitude sample while imprinting a signal on the other that is not in fact present.

A rigorous exploration of the cross-contamination in ([t], [m]) requires a somewhat involved set of computations. For example, flat priors in observed flux (for each the five filters used in BTS) are unlikely to translate into flat priors in ([t], [m]) space, as suggested graphically by the degeneracy exhibited by very metal-poor populations in the ([t], [m]) diagram (e.g. Brown et al. 2009). To properly account for cross-contamination likely requires simulations of the underlying metallicity and temperature distributions (for which a range of shape parameters for the distributions would also need exploration), then translating them forward into the probability density function in ([t], [m]) including full accounting for the shape of the measurement uncertainty distributions and covariances in each of the filters. We consider this beyond the scope of the present work.

Instead, we have performed a simpler quantitative estimate of the degree of cross-contamination in ([t], [m]) space. We assume that the four-component Gaussian Mixture Model (GMM) is indeed a reasonable characterization of the *observed* distribution of ([t], [m]) values, and also that the measurement uncertainties in this space can be described as two-dimensional Gaussians for each object. Samples in ([t], [m]) are simulated by drawing from the best-fit 4-component GMM and perturbing each object by an uncertainty covariance matrix (Equation A2) drawn randomly without replacement from the observed population. Then a four-component GMM is fit to each sample, and objects classified to belong to a model component using the $w_{ik} \geq 0.7$ threshold that was used on the observed dataset (an object cannot satisfy this condition for more than one model component by construction). Finally, the model component classification for each object is compared to the model component from which it was originally drawn, to measure the contamination for each component (i.e. the fraction of objects classified with component K but drawn from $k \neq K$).

Figure 36 shows the results of 5,000 simulation sets. Generally, the "metal-poor" component is relatively uncontaminated by the "metal-rich" population (at $< 1\%$), but is more strongly contaminated (at the $\sim 5\%$ level) by broad background component "2." Under the assumptions of this simulation, the "metal-poor" sample suffers $\lesssim 5.5\%$ contamination from the other components (see the left column of Figure 36).

The "metal-rich" component is more strongly contaminated. Roughly 5% of this sample is contaminated by the "metal-poor" component, with the broad background component "2" contributing $\sim 3.5\%$. Under the simulation assumptions, the "metal-rich" component suffers $\sim 8.5\%$ contamination from the other components (see the right column of Figure 36).

These ranges almost certainly underestimate the true contamination between samples in ([t], [m]). The observed ([t], [m]) distribution tends to be less centrally peaked than the model samples (Figure 5), suggesting the model likely generates samples whose classification by [t], [m] is artificially less vulnerable to contamination than in reality. Furthermore, even if the distribution in flux ratio due to measurement uncertainty is Gaussian for a given filter, for uncertainties $\sigma(\Delta F/F_0) \gtrsim 0.1$ the apparent magnitude uncertainty distribution will deviate substantially from a Gaussian.

Full exploration of these effects is deferred to future work. For the present, our limited simulation suggests that the two samples are contaminated in ([t], [m]) at the $\sim 5\% - 10\%$ level, using the $w_{ik} > 0.7$ threshold for classification.

G. ROTATION CURVES AND BIN STATISTICS IN TABULAR FORM

Full characterization of the variation of the proper motion ellipse with photometric parallax for the two samples can be found in Tables 11 and 13, while Tables 12 and 14 present the same results after converting from relative photometric parallax and proper motion to distance and transverse velocity. The bin statistics for the fine-grained binning scheme are presented in Table 15 and Table 16.

For ease of interpretation and to aid direct comparison with other work, we also tabulate the rotation curves and bin statistics for a binning scheme with constant-width bins (in photometric parallax) for each sample; see Tables 17-22.

Table 11. Observed rotation trend for the "metal-rich" sample, with uncertainty ranges given as 1σ limits based on 1000 parametric bootstrap trials. See discussion in subsection 4.1.

π'	Bin edges	N	$\langle\mu_l\rangle$	$\langle\mu_b\rangle$	a_μ	b_μ	ϕ_{lb}	a/b	σ^2_{ll}	σ^2_{bb}	C_{lb}
mag	mag		(mas yr^{-1})	(mas yr^{-1})	(mas yr^{-1})	(mas yr^{-1})	(°)		(mas^2 yr^{-2})	(mas^2 yr^{-2})	(mas^2 yr^{-2})
-1.34	-1.60,-1.19	25	2.72 ± 0.499	-0.11 ± 0.256	2.5 ± 0.34	1.3 ± 0.17	-4.1 ± 8.11	1.98 ± 0.101	6.38 ± 1.740	1.65 ± 0.434	0.34 ± 0.594
-0.70	-1.18,-0.52	198	1.68 ± 0.187	-0.22 ± 0.156	2.8 ± 0.14	2.2 ± 0.11	20.9 ± 8.58	1.28 ± 0.053	7.33 ± 0.716	5.10 ± 0.506	-1.00 ± 0.443
-0.40	-0.52,-0.34	199	1.20 ± 0.193	-0.10 ± 0.174	2.9 ± 0.15	2.3 ± 0.12	28.5 ± 8.57	1.27 ± 0.055	7.52 ± 0.766	5.81 ± 0.609	-1.31 ± 0.462
-0.29	-0.34,-0.24	198	1.04 ± 0.188	-0.07 ± 0.183	2.8 ± 0.14	2.4 ± 0.12	50.7 ± 24.90	1.16 ± 0.056	7.09 ± 0.689	6.69 ± 0.712	-0.99 ± 0.500
-0.21	-0.24,-0.17	196	1.23 ± 0.184	-0.07 ± 0.195	2.9 ± 0.14	2.4 ± 0.12	51.7 ± 17.76	1.19 ± 0.057	7.34 ± 0.682	6.77 ± 0.756	-1.17 ± 0.522
-0.14	-0.17,-0.11	200	0.89 ± 0.202	0.01 ± 0.194	3.0 ± 0.15	2.5 ± 0.13	38.2 ± 15.31	1.19 ± 0.055	8.13 ± 0.834	7.49 ± 0.754	-1.33 ± 0.547
-0.09	-0.11,-0.06	199	0.89 ± 0.218	0.19 ± 0.200	3.3 ± 0.17	2.6 ± 0.13	31.7 ± 9.70	1.25 ± 0.055	9.60 ± 0.984	7.89 ± 0.823	-1.71 ± 0.626
-0.04	-0.06,-0.01	198	0.46 ± 0.221	0.12 ± 0.197	3.2 ± 0.16	2.5 ± 0.12	32.5 ± 8.67	1.27 ± 0.054	9.27 ± 0.914	7.59 ± 0.742	-1.80 ± 0.591
0.02	-0.01, 0.04	198	-0.15 ± 0.215	0.27 ± 0.202	3.1 ± 0.15	2.7 ± 0.13	37.9 ± 20.30	1.15 ± 0.055	8.78 ± 0.851	8.21 ± 0.825	-1.13 ± 0.615
0.07	0.04, 0.09	199	-0.01 ± 0.220	0.29 ± 0.193	3.2 ± 0.16	2.5 ± 0.13	32.2 ± 9.36	1.27 ± 0.053	9.30 ± 0.903	7.61 ± 0.787	-1.76 ± 0.604
0.12	0.09, 0.15	199	-0.50 ± 0.201	0.32 ± 0.191	3.2 ± 0.16	2.3 ± 0.12	40.9 ± 6.67	1.37 ± 0.052	8.02 ± 0.810	7.35 ± 0.727	-2.31 ± 0.575
0.18	0.15, 0.21	197	-0.81 ± 0.171	0.51 ± 0.184	2.7 ± 0.13	2.4 ± 0.11	60.1 ± 35.28	1.12 ± 0.054	6.96 ± 0.604	6.20 ± 0.717	-0.66 ± 0.467
0.25	0.21, 0.29	200	-1.03 ± 0.177	0.26 ± 0.160	2.5 ± 0.12	2.2 ± 0.10	25.6 ± 18.43	1.14 ± 0.053	6.07 ± 0.595	5.14 ± 0.498	-0.58 ± 0.389
0.34	0.29, 0.42	198	-1.13 ± 0.147	-0.01 ± 0.139	2.1 ± 0.10	1.9 ± 0.09	22.8 ± 20.19	1.13 ± 0.054	4.42 ± 0.446	3.70 ± 0.381	-0.37 ± 0.282
0.56	0.42, 1.43	168	-1.03 ± 0.120	0.03 ± 0.130	1.7 ± 0.08	1.5 ± 0.07	74.2 ± 59.47	1.08 ± 0.053	2.73 ± 0.259	2.41 ± 0.303	-0.10 ± 0.199

Table 12. As Table 11 but with photometric parallaxes and proper motions converted into distances and velocities using a reference distance of 7.76 kpc. See discussion in subsection 4.1.

d	$d_{\rm lo}, d_{\rm hi}$	N	$\langle v_l \rangle$	$\langle v_b \rangle$	a_v	b_v	ϕ_{lb}	a/b	$\sigma^2_{ll,v}$	$\sigma^2_{bb,v}$	$\sigma^2_{lb,v}$
kpc	kpc		(km s^{-1})	(km s^{-1})	(km s^{-1})	(km s^{-1})	(°)		(km^2 s^{-2})	(km^2 s^{-2})	(km^2 s^{-2})
4.19	3.71,4.49	25	54.17 ± 9.921	-2.11 ± 5.082	50 ± 6.9	25 ± 3.4	-4.1 ± 8.11	1.98 ± 0.101	126.8 ± 34.60	32.8 ± 8.63	6.8 ± 11.80
5.61	4.50,6.12	198	44.80 ± 4.978	-5.96 ± 4.163	74 ± 3.6	58 ± 2.8	20.9 ± 8.58	1.28 ± 0.053	195.2 ± 19.05	135.6 ± 13.48	-26.7 ± 11.79
6.47	6.12,6.64	199	36.75 ± 5.926	-2.99 ± 5.333	88 ± 4.5	69 ± 3.5	28.5 ± 8.57	1.27 ± 0.055	230.6 ± 23.50	178.1 ± 18.68	-40.3 ± 14.17
6.80	6.64,6.95	198	33.68 ± 6.053	-2.31 ± 5.896	91 ± 4.4	78 ± 3.8	50.7 ± 24.90	1.16 ± 0.056	228.8 ± 22.22	215.9 ± 22.96	-31.8 ± 16.12
7.05	6.95,7.16	196	41.03 ± 6.158	-2.47 ± 6.504	96 ± 4.8	81 ± 4.0	51.7 ± 17.76	1.19 ± 0.057	245.2 ± 22.80	226.4 ± 25.26	-39.2 ± 17.44
7.27	7.16,7.36	200	30.81 ± 6.968	0.21 ± 6.703	104 ± 5.0	88 ± 4.3	38.2 ± 15.31	1.19 ± 0.055	280.4 ± 28.75	258.3 ± 25.98	-45.9 ± 18.86
7.44	7.36,7.53	199	31.56 ± 7.699	6.67 ± 7.052	115 ± 5.9	92 ± 4.6	31.7 ± 9.70	1.25 ± 0.055	338.7 ± 34.72	278.3 ± 29.05	-60.3 ± 22.07
7.63	7.54,7.74	198	16.67 ± 7.973	4.42 ± 7.117	117 ± 5.7	92 ± 4.5	32.5 ± 8.67	1.27 ± 0.054	335.0 ± 33.05	274.4 ± 26.82	-65.0 ± 21.37
7.83	7.74,7.92	198	-5.63 ± 7.987	9.89 ± 7.483	115 ± 5.5	100 ± 4.9	37.9 ± 20.30	1.15 ± 0.055	325.9 ± 31.59	304.8 ± 30.61	-42.0 ± 22.82
8.01	7.92,8.09	199	-0.36 ± 8.334	10.93 ± 7.326	122 ± 5.9	97 ± 4.8	32.2 ± 9.36	1.27 ± 0.053	353.0 ± 34.28	288.9 ± 29.89	-66.8 ± 22.95
8.20	8.10,8.30	199	-19.36 ± 7.792	12.61 ± 7.417	123 ± 6.2	90 ± 4.5	40.9 ± 6.67	1.37 ± 0.052	311.5 ± 31.47	285.4 ± 28.26	-89.6 ± 22.33
8.42	8.30,8.54	197	-32.24 ± 6.807	20.39 ± 7.329	108 ± 5.2	96 ± 4.5	60.1 ± 35.28	1.12 ± 0.054	277.8 ± 24.10	247.2 ± 28.61	-26.2 ± 18.62
8.70	8.54,8.88	200	-42.48 ± 7.289	10.76 ± 6.595	104 ± 4.8	91 ± 4.2	25.6 ± 18.43	1.14 ± 0.053	250.4 ± 24.53	212.0 ± 20.55	-23.9 ± 16.04
9.07	8.88,9.40	198	-48.71 ± 6.329	-0.45 ± 5.969	92 ± 4.3	81 ± 3.9	22.8 ± 20.19	1.13 ± 0.054	190.0 ± 19.16	159.2 ± 16.38	-15.7 ± 12.15
10.02	9.40,14.99	168	-48.96 ± 5.681	1.49 ± 6.154	79 ± 3.9	73 ± 3.6	74.2 ± 59.47	1.08 ± 0.053	129.8 ± 12.30	114.4 ± 14.38	-4.7 ± 9.46

Table 13. Observed rotation trend for the "metal-poor" sample, with uncertainty ranges given as 1σ limits based on 1000 parametric bootstrap trials. See discussion in subsection 4.1.

π'	Bin edges	N	$\langle\mu_l\rangle$	$\langle\mu_b\rangle$	a_μ	b_μ	ϕ_{lb}	a/b	σ^2_{ll}	σ^2_{bb}	C_{lb}
mag	mag		(mas yr^{-1})	(mas yr^{-1})	(mas yr^{-1})	(mas yr^{-1})	(°)		(mas^2 yr^{-2})	(mas^2 yr^{-2})	(mas^2 yr^{-2})
-1.72	-2.02,-1.57	24	3.00 ± 0.542	0.08 ± 0.413	2.7 ± 0.37	1.9 ± 0.26	-18.4 ± 20.37	1.45 ± 0.126	6.98 ± 1.973	3.89 ± 1.101	1.16 ± 1.048
-1.37	-1.53,-1.31	25	2.45 ± 0.501	-0.60 ± 0.561	2.8 ± 0.34	2.4 ± 0.29	69.8 ± 56.91	1.15 ± 0.113	7.64 ± 1.630	6.19 ± 2.100	-0.62 ± 1.352
-1.04	-1.30,-0.83	199	0.55 ± 0.233	0.12 ± 0.205	3.3 ± 0.16	2.8 ± 0.13	14.7 ± 12.98	1.20 ± 0.054	10.95 ± 1.070	7.93 ± 0.789	-0.85 ± 0.679
-0.71	-0.83,-0.62	198	0.48 ± 0.227	-0.12 ± 0.196	3.4 ± 0.17	2.6 ± 0.13	26.9 ± 7.10	1.33 ± 0.051	10.72 ± 1.096	7.67 ± 0.766	-2.08 ± 0.651
-0.53	-0.62,-0.47	199	0.61 ± 0.228	-0.11 ± 0.219	3.5 ± 0.17	2.6 ± 0.13	45.3 ± 7.83	1.32 ± 0.052	9.54 ± 0.969	9.49 ± 0.968	-2.55 ± 0.699
-0.40	-0.47,-0.36	198	0.27 ± 0.211	-0.10 ± 0.216	3.3 ± 0.16	2.6 ± 0.13	46.7 ± 8.95	1.26 ± 0.054	9.15 ± 0.869	8.91 ± 0.896	-2.07 ± 0.643
-0.31	-0.35,-0.27	199	0.21 ± 0.233	-0.03 ± 0.208	3.2 ± 0.15	2.9 ± 0.13	-0.3 ± 21.70	1.12 ± 0.054	10.47 ± 1.052	8.39 ± 0.831	0.01 ± 0.662
-0.23	-0.27,-0.19	199	0.02 ± 0.223	0.58 ± 0.214	3.2 ± 0.15	2.8 ± 0.14	42.5 ± 22.82	1.13 ± 0.056	9.10 ± 0.941	8.90 ± 0.888	-1.11 ± 0.662
-0.16	-0.19,-0.13	197	0.04 ± 0.215	0.01 ± 0.218	3.3 ± 0.16	2.8 ± 0.13	47.7 ± 18.59	1.17 ± 0.054	9.31 ± 0.894	9.05 ± 0.945	-1.41 ± 0.648
-0.09	-0.13,-0.05	198	-0.03 ± 0.212	0.18 ± 0.210	3.1 ± 0.13	2.9 ± 0.13	37.2 ± 42.45	1.06 ± 0.046	9.03 ± 0.859	8.77 ± 0.886	-0.46 ± 0.628
-0.01	-0.05, 0.02	199	-0.21 ± 0.218	0.19 ± 0.189	3.0 ± 0.15	2.6 ± 0.12	1.5 ± 15.78	1.16 ± 0.056	8.93 ± 0.906	6.61 ± 0.656	-0.06 ± 0.548
0.05	0.02, 0.09	199	-0.33 ± 0.203	0.31 ± 0.211	3.0 ± 0.13	2.7 ± 0.12	41.2 ± 33.67	1.09 ± 0.050	8.28 ± 0.837	8.10 ± 0.806	-0.69 ± 0.567
0.12	0.09, 0.16	199	-0.27 ± 0.204	-0.04 ± 0.203	3.0 ± 0.14	2.7 ± 0.12	26.8 ± 25.51	1.11 ± 0.052	8.43 ± 0.858	7.44 ± 0.737	-0.67 ± 0.555
0.20	0.16, 0.25	197	-0.58 ± 0.217	0.24 ± 0.209	3.0 ± 0.13	2.9 ± 0.13	-47.2 ± 47.68	1.05 ± 0.045	8.67 ± 0.871	8.62 ± 0.874	0.38 ± 0.614
0.30	0.25, 0.36	199	-0.58 ± 0.180	0.42 ± 0.176	2.6 ± 0.12	2.4 ± 0.11	41.9 ± 30.33	1.10 ± 0.051	6.41 ± 0.623	6.28 ± 0.610	-0.61 ± 0.448
0.43	0.36, 0.50	196	-0.73 ± 0.179	0.24 ± 0.162	2.5 ± 0.13	2.2 ± 0.11	17.3 ± 20.36	1.14 ± 0.057	6.29 ± 0.654	5.06 ± 0.509	-0.43 ± 0.422
0.63	0.50, 0.80	192	-0.58 ± 0.143	0.15 ± 0.145	2.0 ± 0.09	1.9 ± 0.09	-67.9 ± 56.38	1.03 ± 0.044	3.99 ± 0.390	3.81 ± 0.394	0.08 ± 0.279
0.97	0.80, 1.45	105	-0.21 ± 0.136	0.37 ± 0.123	1.3 ± 0.08	1.2 ± 0.08	4.5 ± 31.03	1.11 ± 0.064	1.81 ± 0.245	1.47 ± 0.202	-0.03 ± 0.153

Table 14. As Table 13 but with photometric parallaxes and proper motions converted into distances and velocities using a reference distance of 7.76 kpc. See discussion in subsection 4.1.

d	$d_{\rm lo}, d_{\rm hi}$	N	$\langle v_l \rangle$	$\langle v_b \rangle$	a_v	b_v	ϕ_{lb}	a/b	$\sigma^2_{ll,v}$	$\sigma^2_{bb,v}$	$\sigma^2_{lb,v}$
kpc	kpc		(km s^{-1})	(km s^{-1})	(km s^{-1})	(km s^{-1})	(°)		(km^2 s^{-2})	(km^2 s^{-2})	(km^2 s^{-2})
3.52	3.07,3.77	24	50.08 ± 9.046	1.37 ± 6.900	45 ± 6.2	31 ± 4.3	-18.4 ± 20.37	1.45 ± 0.126	116.5 ± 32.94	65.0 ± 18.38	19.3 ± 17.50
4.14	3.83,4.25	25	48.08 ± 9.827	-11.79 ± 11.002	55 ± 6.7	48 ± 5.7	69.8 ± 56.91	1.15 ± 0.113	149.9 ± 31.97	121.4 ± 41.19	-12.1 ± 26.53
4.80	4.26,5.30	199	12.59 ± 5.303	2.83 ± 4.667	76 ± 3.6	63 ± 3.0	14.7 ± 12.98	1.20 ± 0.054	249.3 ± 24.36	180.7 ± 17.97	-19.4 ± 15.47
5.60	5.30,5.84	198	12.87 ± 6.039	-3.07 ± 5.204	91 ± 4.6	68 ± 3.4	26.9 ± 7.10	1.33 ± 0.051	284.7 ± 29.10	203.8 ± 20.35	-55.2 ± 17.28
6.07	5.84,6.26	199	17.52 ± 6.555	-3.14 ± 6.286	100 ± 5.0	76 ± 3.7	45.3 ± 7.83	1.32 ± 0.052	274.4 ± 27.86	272.7 ± 27.84	-73.2 ± 20.10
6.45	6.26,6.59	198	8.36 ± 6.449	-2.97 ± 6.609	102 ± 5.0	81 ± 3.9	46.7 ± 8.95	1.26 ± 0.054	279.6 ± 26.56	272.2 ± 27.37	-63.3 ± 19.64
6.71	6.59,6.85	199	6.67 ± 7.412	-1.01 ± 6.625	103 ± 4.9	92 ± 4.3	-0.3 ± 21.70	1.12 ± 0.054	333.2 ± 33.47	266.9 ± 26.44	0.4 ± 21.06
6.97	6.85,7.09	199	0.53 ± 7.374	19.19 ± 7.061	105 ± 5.1	93 ± 4.5	42.5 ± 22.82	1.13 ± 0.056	300.6 ± 31.09	294.0 ± 29.32	-36.7 ± 21.85
7.20	7.10,7.32	197	1.19 ± 7.355	0.48 ± 7.435	111 ± 5.3	95 ± 4.6	47.7 ± 18.59	1.17 ± 0.054	318.0 ± 30.53	309.0 ± 32.26	-48.0 ± 22.12
7.44	7.32,7.59	198	-1.15 ± 7.480	6.32 ± 7.416	108 ± 4.4	102 ± 4.7	37.2 ± 42.45	1.06 ± 0.046	318.5 ± 30.29	309.3 ± 31.26	-16.3 ± 22.16
7.71	7.59,7.82	199	-7.60 ± 7.952	6.91 ± 6.919	109 ± 5.3	94 ± 4.5	1.5 ± 15.78	1.16 ± 0.056	326.3 ± 33.11	241.5 ± 23.97	-2.3 ± 20.02
7.95	7.82,8.08	199	-12.42 ± 7.656	11.62 ± 7.962	112 ± 5.0	103 ± 4.7	41.2 ± 33.67	1.09 ± 0.050	312.3 ± 31.55	305.4 ± 30.39	-25.9 ± 21.36
8.20	8.08,8.35	199	-10.67 ± 7.919	-1.61 ± 7.878	115 ± 5.3	104 ± 4.7	26.8 ± 25.51	1.11 ± 0.052	327.8 ± 33.37	289.3 ± 28.65	-26.2 ± 21.59
8.51	8.35,8.69	197	-23.22 ± 8.762	9.51 ± 8.411	121 ± 5.2	116 ± 5.1	-47.2 ± 47.68	1.05 ± 0.045	349.7 ± 35.10	347.4 ± 35.22	15.3 ± 24.74
8.89	8.69,9.16	199	-24.36 ± 7.600	17.90 ± 7.432	111 ± 5.0	101 ± 4.5	41.9 ± 30.33	1.10 ± 0.051	270.3 ± 26.24	264.8 ± 25.73	-25.6 ± 18.89
9.45	9.17,9.75	196	-32.79 ± 8.016	10.86 ± 7.281	114 ± 5.6	99 ± 4.8	17.3 ± 20.36	1.14 ± 0.057	281.9 ± 29.29	226.8 ± 22.82	-19.0 ± 18.92
10.37	9.76,11.21	192	-28.63 ± 7.042	7.53 ± 7.152	99 ± 4.2	96 ± 4.3	-67.9 ± 56.38	1.03 ± 0.044	196.0 ± 19.18	187.5 ± 19.36	4.2 ± 13.71
12.15	11.22,15.15	105	-12.30 ± 7.846	21.15 ± 7.072	77 ± 4.7	70 ± 4.4	4.5 ± 31.03	1.11 ± 0.064	104.0 ± 14.10	84.8 ± 11.64	-1.5 ± 8.83

Table 15. Bin statistics for the rotation curves of the "metal-rich" sample. Wedge volumes V and densities ρ assume the reference sample lies at distance 7.76 kpc. $N(\mu_l)$ and $\rho(\mu_l)$ denote the counts and number densities of objects that would pass a kinematic cut of $\mu_l < -2.0$ mas yr^{-1}. The binning scheme is the same as Table 11. The uncertainties quoted refer to 1σ ranges from 1000 parameteric bootstrap trials. See subsection 5.4.

π'	$\pi'_{\rm hi} - \pi'_{\rm lo}$	d	$d_{\rm hi} - d_{\rm lo}$	N	V	ρ	$N(\mu_l)$	$f(\mu_l)$	$\rho(\mu_l)$
mag	mag	kpc	kpc		(pc^3)	(pc^{-3})			(pc^{-3})
-1.34	0.415	4.19	0.782	25	1523.9	0.016	1 ± 0.9	0.04 ± 0.034	0.001 ± 0.0006
-0.70	0.664	5.61	1.611	198	5198.6	0.038	19 ± 3.7	0.10 ± 0.019	0.004 ± 0.0007
-0.40	0.179	6.47	0.525	199	2420.2	0.082	22 ± 4.6	0.11 ± 0.023	0.009 ± 0.0019
-0.29	0.097	6.80	0.303	198	1588.7	0.125	29 ± 4.7	0.15 ± 0.024	0.018 ± 0.0029
-0.21	0.066	7.05	0.214	196	1214.5	0.161	20 ± 4.4	0.10 ± 0.023	0.016 ± 0.0036
-0.14	0.059	7.27	0.197	200	1173.6	0.170	33 ± 5.2	0.17 ± 0.026	0.028 ± 0.0044
-0.09	0.051	7.44	0.175	199	1098.9	0.181	36 ± 5.4	0.18 ± 0.027	0.033 ± 0.0049
-0.04	0.058	7.63	0.204	198	1350.3	0.147	45 ± 5.6	0.23 ± 0.028	0.033 ± 0.0041
0.02	0.049	7.83	0.177	198	1228.2	0.161	54 ± 6.2	0.27 ± 0.031	0.044 ± 0.0050
0.07	0.048	8.01	0.177	199	1294.1	0.154	58 ± 6.2	0.29 ± 0.031	0.045 ± 0.0048
0.12	0.054	8.20	0.205	199	1556.7	0.128	60 ± 6.5	0.30 ± 0.033	0.039 ± 0.0042
0.18	0.062	8.42	0.241	197	1937.4	0.102	61 ± 6.4	0.31 ± 0.032	0.031 ± 0.0033
0.25	0.083	8.70	0.335	200	2878.9	0.069	73 ± 6.7	0.36 ± 0.033	0.025 ± 0.0023
0.34	0.123	9.07	0.519	198	4990.1	0.040	75 ± 6.5	0.38 ± 0.033	0.015 ± 0.0013
0.56	1.012	10.02	5.582	168	105291.0	0.002	43 ± 5.7	0.26 ± 0.034	0.000 ± 0.0001

Table 16. As Table 15 but for the "metal-poor" sample. See subsection 5.4.

π'	$\pi'_{\rm hi} - \pi'_{\rm lo}$	d	$d_{\rm hi} - d_{\rm lo}$	N	V	ρ	$N(\mu_l)$	$f(\mu_l)$	$\rho(\mu_l)$
mag	mag	kpc	kpc		(pc^3)	(pc^{-3})			(pc^{-3})
-1.72	0.450	3.52	0.706	24	1038.4	0.023	1 ± 0.8	0.04 ± 0.035	0.001 ± 0.0008
-1.37	0.225	4.14	0.418	25	783.9	0.032	2 ± 0.9	0.08 ± 0.037	0.003 ± 0.0012
-1.04	0.475	4.80	1.042	199	2701.7	0.074	39 ± 5.8	0.20 ± 0.029	0.014 ± 0.0022
-0.71	0.211	5.60	0.541	198	1914.0	0.103	50 ± 5.6	0.25 ± 0.028	0.026 ± 0.0029
-0.53	0.148	6.07	0.413	199	1740.3	0.114	36 ± 5.9	0.18 ± 0.030	0.021 ± 0.0034
-0.40	0.110	6.45	0.327	198	1542.5	0.128	49 ± 5.7	0.25 ± 0.029	0.032 ± 0.0037
-0.31	0.082	6.71	0.254	199	1310.3	0.152	54 ± 6.0	0.27 ± 0.030	0.041 ± 0.0046
-0.23	0.077	6.97	0.247	199	1364.6	0.146	50 ± 6.4	0.25 ± 0.032	0.037 ± 0.0047
-0.16	0.066	7.20	0.219	197	1295.1	0.152	56 ± 6.0	0.28 ± 0.031	0.043 ± 0.0047
-0.09	0.079	7.44	0.269	198	1702.3	0.116	49 ± 6.0	0.25 ± 0.030	0.029 ± 0.0035
-0.01	0.066	7.71	0.236	199	1587.5	0.125	52 ± 6.4	0.26 ± 0.032	0.033 ± 0.0040
0.05	0.070	7.95	0.257	199	1839.3	0.108	59 ± 6.4	0.30 ± 0.032	0.032 ± 0.0035
0.12	0.072	8.20	0.272	199	2096.1	0.095	65 ± 6.5	0.33 ± 0.033	0.031 ± 0.0031
0.20	0.086	8.51	0.338	197	2782.7	0.071	59 ± 6.7	0.30 ± 0.034	0.021 ± 0.0024
0.30	0.114	8.89	0.470	199	4291.1	0.046	59 ± 6.6	0.30 ± 0.033	0.014 ± 0.0015
0.43	0.134	9.45	0.586	196	6000.0	0.033	60 ± 6.2	0.31 ± 0.032	0.010 ± 0.0010
0.63	0.301	10.37	1.449	192	18176.3	0.011	42 ± 5.8	0.22 ± 0.030	0.002 ± 0.0003
0.97	0.652	12.15	3.929	105	87265.7	0.001	7 ± 3.0	0.07 ± 0.028	0.000 ± 0.0000

Table 17. Observed rotation trend for the "metal-rich" sample, using a constant-width binning scheme and with uncertainty ranges given as 1σ limits based on 1000 parametric bootstrap trials. See discussion in subsection 4.1.

π'	Bin edges	N	$\langle\mu_l\rangle$	$\langle\mu_b\rangle$	a_μ	b_μ	ϕ_{lb}	a/b	σ^2_{ll}	σ^2_{bb}	C_{lb}
mag	mag		(mas yr^{-1})	(mas yr^{-1})	(mas yr^{-1})	(mas yr^{-1})	(°)		(mas^2 yr^{-2})	(mas^2 yr^{-2})	(mas^2 yr^{-2})
-0.82	-0.86,-0.78	26	2.05 ± 0.543	-1.42 ± 0.341	2.8 ± 0.38	1.7 ± 0.23	6.5 ± 14.08	1.63 ± 0.116	8.03 ± 2.161	3.12 ± 0.807	-0.57 ± 0.996
-0.73	-0.77,-0.69	31	0.18 ± 0.465	0.54 ± 0.449	3.0 ± 0.37	2.0 ± 0.25	40.6 ± 16.95	1.52 ± 0.114	6.73 ± 1.725	5.95 ± 1.469	-2.48 ± 1.184
-0.65	-0.69,-0.60	38	1.64 ± 0.447	0.18 ± 0.337	2.8 ± 0.31	2.0 ± 0.22	13.4 ± 18.67	1.39 ± 0.103	7.81 ± 1.777	4.37 ± 1.019	-0.87 ± 0.932
-0.55	-0.60,-0.51	58	1.67 ± 0.356	-0.19 ± 0.305	2.8 ± 0.23	2.3 ± 0.19	-18.0 ± 25.20	1.21 ± 0.091	7.36 ± 1.326	5.44 ± 0.994	0.69 ± 0.821
-0.46	-0.51,-0.43	63	1.55 ± 0.320	-0.05 ± 0.324	2.7 ± 0.21	2.3 ± 0.19	37.3 ± 36.92	1.14 ± 0.079	6.52 ± 1.158	6.09 ± 1.141	-0.78 ± 0.774
-0.38	-0.42,-0.34	133	1.07 ± 0.247	-0.16 ± 0.213	3.0 ± 0.18	2.2 ± 0.13	27.4 ± 8.95	1.33 ± 0.064	7.94 ± 0.962	5.74 ± 0.690	-1.55 ± 0.590
-0.29	-0.34,-0.25	172	1.00 ± 0.194	-0.05 ± 0.207	2.8 ± 0.14	2.5 ± 0.12	52.4 ± 33.57	1.12 ± 0.056	7.01 ± 0.712	6.60 ± 0.753	-0.77 ± 0.526
-0.21	-0.25,-0.16	260	1.22 ± 0.156	-0.06 ± 0.163	2.9 ± 0.12	2.4 ± 0.10	54.8 ± 12.08	1.21 ± 0.048	7.33 ± 0.552	6.47 ± 0.636	-1.21 ± 0.426
-0.12	-0.16,-0.08	315	0.94 ± 0.173	0.14 ± 0.160	3.2 ± 0.13	2.6 ± 0.10	29.5 ± 8.45	1.23 ± 0.044	9.55 ± 0.774	7.75 ± 0.629	-1.50 ± 0.477
-0.03	-0.07, 0.01	316	0.39 ± 0.179	0.13 ± 0.156	3.2 ± 0.13	2.6 ± 0.10	34.2 ± 7.87	1.24 ± 0.043	9.19 ± 0.737	7.86 ± 0.634	-1.68 ± 0.479
0.06	0.01, 0.10	358	-0.21 ± 0.156	0.37 ± 0.145	3.1 ± 0.11	2.6 ± 0.10	36.0 ± 8.53	1.20 ± 0.043	8.45 ± 0.607	7.55 ± 0.568	-1.38 ± 0.432
0.14	0.10, 0.19	297	-0.56 ± 0.170	0.27 ± 0.159	3.1 ± 0.12	2.4 ± 0.10	40.3 ± 7.16	1.27 ± 0.043	7.86 ± 0.643	7.28 ± 0.599	-1.74 ± 0.436
0.23	0.19, 0.27	234	-0.97 ± 0.160	0.29 ± 0.156	2.5 ± 0.11	2.2 ± 0.10	34.2 ± 17.35	1.15 ± 0.052	5.90 ± 0.561	5.32 ± 0.476	-0.73 ± 0.375
0.31	0.28, 0.36	164	-1.13 ± 0.156	0.21 ± 0.165	2.2 ± 0.11	2.0 ± 0.10	58.1 ± 44.44	1.10 ± 0.057	4.48 ± 0.467	4.11 ± 0.496	-0.37 ± 0.330
0.40	0.36, 0.45	92	-1.15 ± 0.234	-0.30 ± 0.209	2.2 ± 0.15	2.0 ± 0.13	7.0 ± 29.69	1.13 ± 0.069	4.95 ± 0.717	3.93 ± 0.578	-0.13 ± 0.459
0.49	0.45, 0.54	52	-0.99 ± 0.264	0.41 ± 0.272	2.0 ± 0.17	1.8 ± 0.15	-58.2 ± 50.02	1.12 ± 0.083	3.72 ± 0.650	3.36 ± 0.700	0.36 ± 0.502
0.56	0.54, 0.62	31	-0.80 ± 0.317	0.38 ± 0.267	1.7 ± 0.19	1.5 ± 0.16	-19.9 ± 37.90	1.16 ± 0.103	2.89 ± 0.724	2.31 ± 0.565	0.24 ± 0.434
0.67	0.63, 0.71	22	-1.38 ± 0.334	-0.25 ± 0.366	2.1 ± 0.31	1.2 ± 0.17	51.0 ± 16.87	1.77 ± 0.117	3.13 ± 0.767	2.52 ± 0.924	-1.43 ± 0.668

Table 18. As Table 17 (i.e., using a constant-width binning scheme) but with photometric parallaxes and proper motions converted into distances and velocities using a reference distance of 7.76 kpc. See discussion in subsection 4.1.

d	$d_{\rm lo}, d_{\rm hi}$	N	$\langle v_l \rangle$	$\langle v_b \rangle$	a_v	b_v	ϕ_{lb}	a/b	$\sigma^2_{ll,v}$	$\sigma^2_{bb,v}$	$\sigma^2_{lb,v}$
kpc	kpc		(km s^{-1})	(km s^{-1})	(km s^{-1})	(km s^{-1})	($^\circ$)		(km^2 s^{-2})	(km^2 s^{-2})	(km^2 s^{-2})
5.33	5.22,5.43	26	51.73 ± 13.719	-35.89 ± 8.624	72 ± 9.5	44 ± 5.8	6.5 ± 14.08	1.63 ± 0.116	202.7 ± 54.58	78.9 ± 20.39	-14.3 ± 25.16
5.53	5.43,5.65	31	4.61 ± 12.194	14.16 ± 11.770	78 ± 9.8	51 ± 6.6	40.6 ± 16.95	1.52 ± 0.114	176.4 ± 45.24	156.1 ± 38.52	-65.0 ± 31.06
5.75	5.66,5.88	38	44.65 ± 12.192	4.91 ± 9.198	77 ± 8.4	56 ± 6.0	13.4 ± 18.67	1.39 ± 0.103	212.9 ± 48.43	119.2 ± 27.78	-23.7 ± 25.40
6.02	5.89,6.12	58	47.66 ± 10.146	-5.40 ± 8.711	79 ± 6.7	65 ± 5.5	-18.0 ± 25.20	1.21 ± 0.091	209.8 ± 37.84	155.3 ± 28.37	19.8 ± 23.43
6.27	6.13,6.37	63	46.01 ± 9.532	-1.39 ± 9.623	79 ± 6.2	70 ± 5.7	37.3 ± 36.92	1.14 ± 0.079	193.9 ± 34.45	181.2 ± 33.95	-23.1 ± 23.01
6.53	6.38,6.64	133	33.16 ± 7.649	-4.89 ± 6.577	91 ± 5.4	69 ± 4.1	27.4 ± 8.95	1.33 ± 0.064	245.6 ± 29.77	177.7 ± 21.35	-48.1 ± 18.25
6.79	6.64,6.92	172	32.17 ± 6.243	-1.55 ± 6.643	89 ± 4.4	79 ± 3.9	52.4 ± 33.57	1.12 ± 0.056	225.4 ± 22.91	212.3 ± 24.22	-24.6 ± 16.93
7.05	6.92,7.20	260	40.72 ± 5.230	-2.00 ± 5.462	96 ± 4.0	79 ± 3.3	54.8 ± 12.08	1.21 ± 0.048	245.1 ± 18.47	216.2 ± 21.26	-40.6 ± 14.24
7.36	7.20,7.50	315	32.95 ± 6.035	4.71 ± 5.566	112 ± 4.4	92 ± 3.6	29.5 ± 8.45	1.23 ± 0.044	333.1 ± 26.99	270.3 ± 21.95	-52.2 ± 16.64
7.65	7.50,7.80	316	13.96 ± 6.481	4.83 ± 5.656	117 ± 4.6	94 ± 3.6	34.2 ± 7.87	1.24 ± 0.043	333.1 ± 26.72	284.9 ± 22.99	-60.9 ± 17.36
7.97	7.80,8.12	358	-8.09 ± 5.894	13.93 ± 5.494	116 ± 4.2	97 ± 3.6	36.0 ± 8.53	1.20 ± 0.043	319.0 ± 22.91	285.1 ± 21.44	-52.0 ± 16.31
8.29	8.13,8.46	297	-21.98 ± 6.689	10.47 ± 6.257	120 ± 4.8	95 ± 3.8	40.3 ± 7.16	1.27 ± 0.043	308.7 ± 25.26	286.0 ± 23.54	-68.5 ± 17.12
8.61	8.46,8.81	234	-39.43 ± 6.548	11.89 ± 6.362	103 ± 4.7	90 ± 4.0	34.2 ± 17.35	1.15 ± 0.052	240.8 ± 22.91	217.3 ± 19.42	-29.7 ± 15.33
8.97	8.81,9.17	164	-48.08 ± 6.617	8.73 ± 7.030	92 ± 4.6	84 ± 4.3	58.1 ± 44.44	1.10 ± 0.057	190.2 ± 19.84	174.6 ± 21.06	-15.9 ± 14.02
9.34	9.17,9.54	92	-50.70 ± 10.361	-13.27 ± 9.248	99 ± 6.5	88 ± 5.9	7.0 ± 29.69	1.13 ± 0.069	219.4 ± 31.76	173.8 ± 25.61	-5.7 ± 20.32
9.72	9.55,9.93	52	-45.54 ± 12.147	19.04 ± 12.550	91 ± 7.7	82 ± 7.0	-58.2 ± 50.02	1.12 ± 0.083	171.3 ± 29.94	154.8 ± 32.27	16.5 ± 23.13
10.06	9.94,10.33	31	-38.38 ± 15.128	17.89 ± 12.757	82 ± 9.1	71 ± 7.4	-19.9 ± 37.90	1.16 ± 0.103	137.6 ± 34.51	110.4 ± 26.95	11.4 ± 20.68
10.55	10.35,10.77	22	-69.20 ± 16.690	-12.42 ± 18.308	103 ± 15.3	58 ± 8.6	51.0 ± 16.87	1.77 ± 0.117	156.4 ± 38.34	126.1 ± 46.23	-71.4 ± 33.39

Table 19. Observed rotation trend for the "metal-poor" sample, using a constant-width binning scheme, with uncertainty ranges given as 1σ limits based on 1000 parametric bootstrap trials. See discussion in subsection 4.1.

π'	Bin edges	N	$\langle\mu_l\rangle$	$\langle\mu_b\rangle$	a_μ	b_μ	ϕ_{lb}	a/b	σ^2_{ll}	σ^2_{bb}	C_{lb}
mag	mag		(mas yr^{-1})	(mas yr^{-1})	(mas yr^{-1})	(mas yr^{-1})	(°)		(mas^2 yr^{-2})	(mas^2 yr^{-2})	(mas^2 yr^{-2})
-1.24	-1.29,-1.21	27	1.26 ± 0.639	0.89 ± 0.471	3.2 ± 0.38	2.4 ± 0.30	0.3 ± 24.76	1.33 ± 0.113	10.15 ± 2.602	5.78 ± 1.505	-0.02 ± 1.436
-1.16	-1.21,-1.13	25	1.72 ± 0.645	-0.86 ± 0.629	3.7 ± 0.49	2.8 ± 0.37	40.4 ± 29.02	1.32 ± 0.122	11.27 ± 2.967	10.32 ± 2.925	-2.91 ± 2.234
-1.07	-1.12,-1.04	47	-0.09 ± 0.518	0.04 ± 0.421	3.5 ± 0.33	2.8 ± 0.27	5.0 ± 27.46	1.21 ± 0.095	11.91 ± 2.429	8.13 ± 1.694	-0.33 ± 1.434
-0.99	-1.04,-0.95	33	0.94 ± 0.579	0.54 ± 0.457	3.4 ± 0.40	2.5 ± 0.30	4.9 ± 20.27	1.36 ± 0.114	11.66 ± 2.810	6.32 ± 1.580	-0.46 ± 1.491
-0.90	-0.95,-0.86	41	0.23 ± 0.432	0.01 ± 0.421	2.9 ± 0.27	2.6 ± 0.25	38.2 ± 44.80	1.10 ± 0.088	7.60 ± 1.687	7.27 ± 1.611	-0.68 ± 1.121
-0.82	-0.86,-0.78	61	-0.29 ± 0.374	0.55 ± 0.394	3.1 ± 0.25	2.8 ± 0.21	72.4 ± 59.76	1.12 ± 0.080	9.44 ± 1.364	7.82 ± 1.700	-0.57 ± 1.100
-0.73	-0.77,-0.69	79	0.50 ± 0.386	-0.08 ± 0.302	3.6 ± 0.29	2.3 ± 0.18	28.7 ± 7.29	1.57 ± 0.070	11.16 ± 1.767	7.04 ± 1.126	-3.23 ± 1.040
-0.64	-0.69,-0.60	99	0.85 ± 0.328	-0.60 ± 0.280	3.4 ± 0.24	2.6 ± 0.17	21.9 ± 10.73	1.34 ± 0.072	10.91 ± 1.608	7.22 ± 1.028	-1.77 ± 0.893
-0.56	-0.60,-0.52	124	0.40 ± 0.274	-0.34 ± 0.271	3.5 ± 0.21	2.6 ± 0.15	40.3 ± 8.66	1.38 ± 0.061	10.06 ± 1.238	9.09 ± 1.155	-2.94 ± 0.868
-0.46	-0.51,-0.43	119	0.18 ± 0.276	0.24 ± 0.281	3.2 ± 0.20	2.7 ± 0.16	51.8 ± 21.22	1.21 ± 0.069	9.30 ± 1.052	8.53 ± 1.177	-1.60 ± 0.838
-0.38	-0.42,-0.34	177	0.41 ± 0.231	-0.14 ± 0.224	3.3 ± 0.17	2.9 ± 0.14	39.6 ± 19.35	1.16 ± 0.058	9.87 ± 1.080	9.34 ± 0.976	-1.40 ± 0.724
-0.29	-0.34,-0.25	209	0.20 ± 0.219	0.10 ± 0.194	3.2 ± 0.15	2.8 ± 0.13	10.5 ± 17.86	1.15 ± 0.054	10.35 ± 1.026	7.99 ± 0.775	-0.45 ± 0.671
-0.20	-0.25,-0.16	245	0.18 ± 0.193	0.40 ± 0.200	3.3 ± 0.14	2.8 ± 0.13	57.5 ± 19.24	1.15 ± 0.052	9.94 ± 0.800	8.82 ± 0.889	-1.20 ± 0.597
-0.12	-0.16,-0.08	233	0.04 ± 0.206	0.07 ± 0.193	3.1 ± 0.12	2.9 ± 0.12	36.8 ± 30.79	1.09 ± 0.047	9.23 ± 0.859	8.79 ± 0.767	-0.74 ± 0.593
-0.03	-0.07, 0.01	246	-0.24 ± 0.196	0.24 ± 0.162	3.0 ± 0.13	2.5 ± 0.12	13.5 ± 13.20	1.17 ± 0.052	8.74 ± 0.788	6.57 ± 0.611	-0.55 ± 0.487
0.06	0.01, 0.10	250	-0.39 ± 0.187	0.23 ± 0.175	3.0 ± 0.12	2.8 ± 0.11	29.4 ± 34.34	1.07 ± 0.045	8.53 ± 0.766	7.97 ± 0.710	-0.47 ± 0.522
0.14	0.10, 0.19	227	-0.47 ± 0.184	0.13 ± 0.181	2.9 ± 0.12	2.8 ± 0.12	15.9 ± 40.24	1.03 ± 0.043	8.16 ± 0.753	7.70 ± 0.730	-0.14 ± 0.554
0.23	0.19, 0.27	191	-0.34 ± 0.202	-0.01 ± 0.208	2.9 ± 0.13	2.7 ± 0.12	37.2 ± 37.35	1.08 ± 0.049	7.91 ± 0.803	7.59 ± 0.790	-0.56 ± 0.578
0.31	0.28, 0.36	145	-0.75 ± 0.222	0.57 ± 0.215	2.6 ± 0.13	2.5 ± 0.13	15.0 ± 46.51	1.03 ± 0.051	6.63 ± 0.751	6.29 ± 0.766	-0.10 ± 0.539
0.41	0.36, 0.45	127	-0.80 ± 0.219	0.36 ± 0.183	2.4 ± 0.14	2.0 ± 0.12	-6.9 ± 16.66	1.21 ± 0.067	5.93 ± 0.736	4.07 ± 0.511	0.23 ± 0.429
0.49	0.45, 0.54	96	-0.52 ± 0.266	0.12 ± 0.250	2.7 ± 0.18	2.4 ± 0.16	39.4 ± 32.26	1.14 ± 0.070	6.61 ± 0.931	6.29 ± 0.946	-0.82 ± 0.664
0.58	0.54, 0.62	64	-0.71 ± 0.277	-0.11 ± 0.308	2.6 ± 0.20	2.1 ± 0.18	-55.7 ± 38.51	1.21 ± 0.084	5.88 ± 0.885	5.11 ± 0.974	0.98 ± 0.703
0.66	0.63, 0.71	59	-0.29 ± 0.229	0.02 ± 0.252	2.0 ± 0.17	1.6 ± 0.14	52.1 ± 27.42	1.28 ± 0.092	3.46 ± 0.563	3.08 ± 0.627	-0.76 ± 0.434
0.75	0.71, 0.80	41	-0.71 ± 0.219	0.42 ± 0.198	1.5 ± 0.15	1.2 ± 0.12	29.6 ± 27.18	1.24 ± 0.101	2.00 ± 0.446	1.61 ± 0.336	-0.33 ± 0.278
0.83	0.80, 0.88	34	-0.21 ± 0.270	0.81 ± 0.269	1.8 ± 0.20	1.3 ± 0.15	44.6 ± 23.72	1.35 ± 0.109	2.52 ± 0.618	2.50 ± 0.588	-0.73 ± 0.422
0.93	0.89, 0.97	20	-0.28 ± 0.211	-0.04 ± 0.223	1.2 ± 0.17	0.8 ± 0.11	-50.1 ± 22.51	1.55 ± 0.128	1.04 ± 0.274	0.90 ± 0.325	0.40 ± 0.226

Table 20. As Table 19 (i.e., using a constant-width binning scheme) but with photometric parallaxes and proper motions converted into distances and velocities using a reference distance of 7.76 kpc. See discussion in subsection 4.1.

d	$d_{\rm lo}, d_{\rm hi}$	N	$\langle v_l \rangle$	$\langle v_b \rangle$	a_v	b_v	ϕ_{lb}	a/b	$\sigma^2_{ll,v}$	$\sigma^2_{bb,v}$	$\sigma^2_{lb,v}$
kpc	kpc		(km s^{-1})	(km s^{-1})	(km s^{-1})	(km s^{-1})	($^\circ$)		(km^2 s^{-2})	(km^2 s^{-2})	(km^2 s^{-2})
4.38	4.28,4.44	27	26.18 ± 13.259	18.48 ± 9.761	66 ± 8.0	50 ± 6.1	0.3 ± 24.76	1.33 ± 0.113	210.6 ± 53.97	119.9 ± 31.22	-0.4 ± 29.79
4.55	4.45,4.61	25	37.02 ± 13.892	-18.63 ± 13.557	80 ± 10.5	60 ± 7.9	40.4 ± 29.02	1.32 ± 0.122	242.8 ± 63.93	222.4 ± 63.02	-62.6 ± 48.14
4.74	4.63,4.81	47	-2.12 ± 11.648	0.81 ± 9.462	78 ± 7.3	64 ± 6.2	5.0 ± 27.46	1.21 ± 0.095	267.7 ± 54.58	182.7 ± 38.07	-7.4 ± 32.23
4.92	4.82,5.01	33	22.00 ± 13.518	12.49 ± 10.669	80 ± 9.3	59 ± 7.0	4.9 ± 20.27	1.36 ± 0.114	272.2 ± 65.59	147.6 ± 36.87	-10.8 ± 34.80
5.12	5.01,5.21	41	5.54 ± 10.476	0.24 ± 10.201	69 ± 6.6	63 ± 6.2	38.2 ± 44.80	1.10 ± 0.088	184.2 ± 40.90	176.2 ± 39.07	-16.5 ± 27.18
5.33	5.22,5.42	61	-7.24 ± 9.449	14.00 ± 9.945	78 ± 6.4	70 ± 5.4	72.4 ± 59.76	1.12 ± 0.080	238.5 ± 34.46	197.7 ± 42.94	-14.4 ± 27.78
5.54	5.43,5.65	79	13.12 ± 10.139	-2.07 ± 7.943	95 ± 7.5	60 ± 4.7	28.7 ± 7.29	1.57 ± 0.070	293.4 ± 46.44	185.0 ± 29.59	-85.0 ± 27.34
5.78	5.66,5.89	99	23.30 ± 9.003	-16.40 ± 7.670	93 ± 6.7	70 ± 4.8	21.9 ± 10.73	1.34 ± 0.072	299.1 ± 44.09	198.0 ± 28.18	-48.6 ± 24.47
6.01	5.89,6.12	124	11.34 ± 7.796	-9.66 ± 7.724	101 ± 6.1	73 ± 4.4	40.3 ± 8.66	1.38 ± 0.061	286.4 ± 35.25	258.8 ± 32.89	-83.6 ± 24.70
6.27	6.13,6.38	119	5.32 ± 8.197	7.14 ± 8.335	97 ± 6.1	80 ± 4.8	51.8 ± 21.22	1.21 ± 0.069	276.3 ± 31.26	253.4 ± 34.95	-47.5 ± 24.89
6.52	6.39,6.64	177	12.80 ± 7.143	-4.18 ± 6.929	103 ± 5.2	88 ± 4.5	39.6 ± 19.35	1.16 ± 0.058	305.0 ± 33.38	288.6 ± 30.17	-43.2 ± 22.36
6.78	6.64,6.92	209	6.39 ± 7.030	3.17 ± 6.248	104 ± 5.0	90 ± 4.3	10.5 ± 17.86	1.15 ± 0.054	332.7 ± 32.98	256.8 ± 24.90	-14.5 ± 21.58
7.06	6.92,7.20	245	6.10 ± 6.475	13.25 ± 6.702	110 ± 4.8	95 ± 4.2	57.5 ± 19.24	1.15 ± 0.052	332.8 ± 26.77	295.1 ± 29.75	-40.3 ± 19.99
7.33	7.20,7.50	233	1.39 ± 7.172	2.52 ± 6.716	109 ± 4.3	100 ± 4.3	36.8 ± 30.79	1.09 ± 0.047	320.7 ± 29.85	305.5 ± 26.64	-25.8 ± 20.60
7.66	7.50,7.80	246	-8.81 ± 7.133	8.64 ± 5.885	108 ± 4.8	92 ± 4.2	13.5 ± 13.20	1.17 ± 0.052	317.4 ± 28.60	238.7 ± 22.20	-20.0 ± 17.70
7.96	7.81,8.12	250	-14.80 ± 7.073	8.66 ± 6.622	112 ± 4.6	105 ± 4.1	29.4 ± 34.34	1.07 ± 0.045	322.1 ± 28.91	300.7 ± 26.80	-17.7 ± 19.69
8.29	8.13,8.46	227	-18.26 ± 7.233	5.27 ± 7.098	112 ± 4.6	109 ± 4.5	15.9 ± 40.24	1.03 ± 0.043	320.7 ± 29.57	302.6 ± 28.67	-5.6 ± 21.77
8.63	8.46,8.81	191	-13.72 ± 8.245	-0.49 ± 8.514	118 ± 5.5	109 ± 4.9	37.2 ± 37.35	1.08 ± 0.049	323.3 ± 32.84	310.4 ± 32.32	-22.8 ± 23.63
8.96	8.81,9.17	145	-31.86 ± 9.436	24.16 ± 9.114	110 ± 5.5	106 ± 5.4	15.0 ± 46.51	1.03 ± 0.051	281.4 ± 31.91	267.2 ± 32.52	-4.1 ± 22.90
9.37	9.18,9.54	127	-35.54 ± 9.734	15.79 ± 8.147	108 ± 6.4	89 ± 5.6	-6.9 ± 16.66	1.21 ± 0.067	263.3 ± 32.68	180.7 ± 22.72	10.1 ± 19.05
9.72	9.55,9.94	96	-24.02 ± 12.238	5.51 ± 11.503	124 ± 8.3	109 ± 7.2	39.4 ± 32.26	1.14 ± 0.070	304.6 ± 42.85	289.6 ± 43.54	-37.8 ± 30.56
10.14	9.94,10.34	64	-34.30 ± 13.302	-5.27 ± 14.795	123 ± 9.6	101 ± 8.4	-55.7 ± 38.51	1.21 ± 0.084	282.7 ± 42.51	245.6 ± 46.81	47.1 ± 33.77
10.53	10.35,10.77	59	-14.67 ± 11.447	0.99 ± 12.591	101 ± 8.7	79 ± 7.2	52.1 ± 27.42	1.28 ± 0.092	173.0 ± 28.10	154.0 ± 31.33	-37.8 ± 21.68
10.97	10.78,11.21	41	-36.98 ± 11.367	21.67 ± 10.307	77 ± 8.1	62 ± 6.3	29.6 ± 27.18	1.24 ± 0.101	104.1 ± 23.19	83.6 ± 17.47	-17.1 ± 14.47
11.38	11.22,11.65	34	-11.59 ± 14.555	43.79 ± 14.508	97 ± 10.9	72 ± 8.1	44.6 ± 23.72	1.35 ± 0.109	135.9 ± 33.32	134.8 ± 31.71	-39.3 ± 22.73
11.90	11.68,12.15	20	-15.73 ± 11.877	-2.35 ± 12.595	66 ± 9.7	43 ± 6.5	-50.1 ± 22.51	1.55 ± 0.128	58.8 ± 15.48	50.8 ± 18.33	22.3 ± 12.74

Table 21. Bin statistics for the rotation curves of the "metal-rich" sample, using a constant-width binning scheme. Wedge volumes V and densities ρ assume the reference sample lies at distance 7.76 kpc. $N(\mu_l)$ and $\rho(\mu_l)$ denote the counts and number densities of objects that would pass a kinematic cut of $\mu_l < -2.0$ mas yr^{-1}. The binning scheme is the same as Table 11. The uncertainties quoted refer to 1σ ranges from 1000 parameteric bootstrap trials. See subsection 5.4.

π'	$\pi'_{\rm hi} - \pi'_{\rm lo}$	d	$d_{\rm hi} - d_{\rm lo}$	N	V	ρ	$N(\mu_l)$	$f(\mu_l)$	$\rho(\mu_l)$
mag	mag	kpc	kpc		(pc^3)	(pc^{-3})			(pc^{-3})
-0.82	0.083	5.33	0.203	26	688.1	0.038	3 ± 1.3	0.12 ± 0.050	0.004 ± 0.0019
-0.73	0.086	5.53	0.220	31	776.5	0.040	7 ± 2.2	0.23 ± 0.071	0.009 ± 0.0028
-0.65	0.085	5.75	0.227	38	876.3	0.043	3 ± 1.8	0.08 ± 0.049	0.003 ± 0.0021
-0.55	0.084	6.02	0.234	58	988.9	0.059	5 ± 2.1	0.09 ± 0.037	0.005 ± 0.0022
-0.46	0.084	6.27	0.243	63	1116.0	0.056	2 ± 2.2	0.03 ± 0.034	0.002 ± 0.0019
-0.38	0.087	6.53	0.260	133	1259.4	0.106	19 ± 3.9	0.14 ± 0.029	0.015 ± 0.0031
-0.29	0.087	6.79	0.271	172	1421.2	0.121	27 ± 4.3	0.16 ± 0.025	0.019 ± 0.0030
-0.21	0.087	7.05	0.283	260	1603.8	0.162	24 ± 4.8	0.09 ± 0.018	0.015 ± 0.0030
-0.12	0.087	7.36	0.294	315	1809.9	0.174	57 ± 6.7	0.18 ± 0.021	0.031 ± 0.0037
-0.03	0.087	7.65	0.306	316	2042.5	0.155	70 ± 7.6	0.22 ± 0.024	0.034 ± 0.0037
0.06	0.087	7.97	0.319	358	2305.0	0.155	106 ± 8.2	0.30 ± 0.023	0.046 ± 0.0036
0.14	0.087	8.29	0.332	297	2601.1	0.114	92 ± 8.0	0.31 ± 0.027	0.035 ± 0.0031
0.23	0.086	8.61	0.343	234	2935.4	0.080	81 ± 7.2	0.35 ± 0.031	0.028 ± 0.0025
0.31	0.087	8.97	0.360	164	3312.6	0.050	58 ± 6.0	0.35 ± 0.037	0.018 ± 0.0018
0.40	0.086	9.34	0.370	92	3738.2	0.025	37 ± 4.5	0.40 ± 0.049	0.010 ± 0.0012
0.49	0.084	9.72	0.378	52	4218.6	0.012	15 ± 3.3	0.29 ± 0.064	0.004 ± 0.0008
0.56	0.082	10.06	0.384	31	4760.6	0.007	8 ± 2.4	0.26 ± 0.078	0.002 ± 0.0005
0.67	0.085	10.55	0.416	22	5372.3	0.004	8 ± 2.2	0.36 ± 0.100	0.001 ± 0.0004

Table 22. As Table 21 (i.e., with a constant-width binning scheme) but for the "metal-poor" sample. See subsection 5.4.

π'	$\pi'_{\rm hi} - \pi'_{\rm lo}$	d	$d_{\rm hi} - d_{\rm lo}$	N	V	ρ	$N(\mu_l)$	$f(\mu_l)$	$\rho(\mu_l)$
mag	mag	kpc	kpc		(pc^3)	(pc^{-3})			(pc^{-3})
-1.24	0.080	4.38	0.160	27	376.0	0.072	5 ± 1.8	0.19 ± 0.068	0.013 ± 0.0049
-1.16	0.077	4.55	0.161	25	424.3	0.059	3 ± 1.7	0.12 ± 0.068	0.007 ± 0.0040
-1.07	0.085	4.74	0.185	47	478.8	0.098	12 ± 3.1	0.26 ± 0.067	0.025 ± 0.0065
-0.99	0.085	4.92	0.192	33	540.3	0.061	4 ± 2.3	0.12 ± 0.069	0.007 ± 0.0042
-0.90	0.085	5.12	0.201	41	609.8	0.067	7 ± 2.6	0.17 ± 0.064	0.011 ± 0.0043
-0.82	0.083	5.33	0.204	61	688.1	0.089	20 ± 3.5	0.33 ± 0.057	0.029 ± 0.0051
-0.73	0.086	5.54	0.219	79	776.5	0.102	21 ± 3.8	0.27 ± 0.048	0.027 ± 0.0049
-0.64	0.087	5.78	0.230	99	876.3	0.113	17 ± 3.8	0.17 ± 0.039	0.019 ± 0.0044
-0.56	0.084	6.01	0.233	124	988.9	0.125	25 ± 4.4	0.20 ± 0.035	0.025 ± 0.0044
-0.46	0.087	6.27	0.249	119	1116.0	0.107	29 ± 4.6	0.24 ± 0.039	0.026 ± 0.0041
-0.38	0.085	6.52	0.256	177	1259.4	0.141	43 ± 5.5	0.24 ± 0.031	0.034 ± 0.0044
-0.29	0.087	6.78	0.272	209	1421.2	0.147	55 ± 6.2	0.26 ± 0.030	0.039 ± 0.0044
-0.20	0.087	7.06	0.283	245	1603.8	0.153	61 ± 6.6	0.25 ± 0.027	0.038 ± 0.0041
-0.12	0.087	7.33	0.295	233	1809.9	0.129	60 ± 6.8	0.26 ± 0.029	0.033 ± 0.0037
-0.03	0.087	7.66	0.306	246	2042.5	0.120	65 ± 7.1	0.26 ± 0.029	0.032 ± 0.0035
0.06	0.086	7.96	0.317	250	2305.0	0.108	79 ± 7.3	0.32 ± 0.029	0.034 ± 0.0032
0.14	0.087	8.29	0.333	227	2601.1	0.087	73 ± 6.7	0.32 ± 0.030	0.028 ± 0.0026
0.23	0.087	8.63	0.346	191	2935.4	0.065	53 ± 6.1	0.28 ± 0.032	0.018 ± 0.0021
0.31	0.087	8.96	0.360	145	3312.6	0.044	46 ± 5.6	0.32 ± 0.039	0.014 ± 0.0017
0.41	0.084	9.37	0.362	127	3738.2	0.034	42 ± 5.3	0.33 ± 0.042	0.011 ± 0.0014
0.49	0.086	9.72	0.385	96	4218.6	0.023	25 ± 4.5	0.26 ± 0.047	0.006 ± 0.0011
0.58	0.086	10.14	0.403	64	4760.6	0.013	19 ± 3.5	0.30 ± 0.055	0.004 ± 0.0007
0.66	0.086	10.53	0.418	59	5372.3	0.011	7 ± 2.9	0.12 ± 0.049	0.001 ± 0.0005
0.75	0.085	10.97	0.433	41	6062.7	0.007	7 ± 2.4	0.17 ± 0.059	0.001 ± 0.0004
0.83	0.083	11.38	0.438	34	6841.7	0.005	3 ± 2.0	0.09 ± 0.058	0.000 ± 0.0003
0.93	0.085	11.90	0.464	20	7720.8	0.003	2 ± 0.8	0.10 ± 0.042	0.000 ± 0.0001